



ÉCOLE POLYTECHNIQUE  
FÉDÉRALE DE LAUSANNE

MASTER PROJECT CMCS  
(PROF. ALFIO QUARTERONI)  
Year 2012-2013 – Spring semester

---

# Phenomenological and physiological approaches in the study of cardiac alternans.

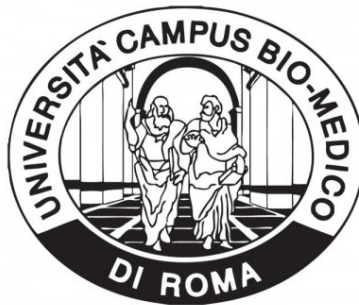
## Theoretical background, mathematical modeling and numerical simulations.

---

*Author:*  
Marie DUPRAZ

*Supervisor in EPFL:*  
Dr. Ricardo RUIZ-BAYER

*Supervisors in Università Campus  
Bio-Medico:*  
Prof. Simonetta FILIPPI  
Dr. Alessio GIZZI



June 19, 2013

## Abstract

This project presents the theoretical background in electrophysiology that is used as a basis in the development of numerical methods for the simulation of heart's electrical activity. We discuss the mathematical models currently used in cardiac electrophysiology research to simulate the propagation of an action potential wave, and then focus on the description of the ionic currents. This study allows us to anticipate the numerical model sensitivity with regard to the discretization, with the aim of recovering the physiological behaviors of the tissue (i.e. conduction velocity, electrical restitution, ...). Thereafter, we introduce the pseudo-ECG signal reconstruction method from the action potential map. This leads us to examine the approximation of such a signal using the finite element basis coming from the discretization of the monodomain equations. We discuss then a particular cardiac rhythm disorder: action potential alternans.

In a second step, we perform an extended simulation study in order to validate the previous numerical methods. We carefully check the convergence of the conduction velocity with respect to the mesh size, and we bring out the advantage of phenomenological approach in terms of electrical restitutions and computational cost. We reproduce typical rhythm disorders and show that the pseudo-ECG signal is able to detect them. Finally, we discuss the influence of anisotropy in cardiac wave propagation and alternans development, characterizing the effect of fibers direction and pacing site in the resulting spatio-temporal distribution.

# Contents

<b>1</b>	<b>Introduction</b>	<b>5</b>
<b>2</b>	<b>Mathematical models in electrophysiology</b>	<b>7</b>
2.1	Electrical activity in biological tissues . . . . .	7
2.1.1	Derivation of the diffusion problem . . . . .	7
2.1.2	Reaction-diffusion equations . . . . .	9
2.1.3	Electrical properties of the cell membrane . . . . .	10
2.1.4	Cable equation . . . . .	12
2.2	Description and properties of the cardiac action potential . . . . .	16
2.3	Cardiac tissue modeling . . . . .	17
2.3.1	Bidomain model . . . . .	20
2.3.2	Monodomain model . . . . .	21
2.3.3	Geometry of the cardiac tissue . . . . .	22
2.4	Ionic models . . . . .	24
2.4.1	Physiological models . . . . .	24
2.4.2	Phenomenological models . . . . .	27
<b>3</b>	<b>Numerical methods and discretization of the monodomain equations</b>	<b>31</b>
3.1	Finite difference approximation of the 1d and 2d cases . . . . .	31
3.1.1	Discretization for the 1d case . . . . .	31
3.1.2	Generalization to the 2d case . . . . .	32
3.2	Finite element methods for the tridimensional simulations . . . . .	34
3.2.1	Finite element discretization . . . . .	34
3.2.2	Interpolation of the ionic current . . . . .	35
3.2.3	Operator splitting . . . . .	36
3.2.4	Mass lumping . . . . .	38
<b>4</b>	<b>Pseudo-ECG</b>	<b>39</b>
4.1	Definition and derivation . . . . .	39
4.2	Approximation and computation . . . . .	41
4.2.1	Finite element approximation of $\Delta V_m(\mathbf{x}, t)$ . . . . .	41
4.2.2	Computation of the pseudo-ECG summation . . . . .	42
<b>5</b>	<b>Alternans dynamics in cardiac tissue</b>	<b>43</b>
5.1	Action potential alternans . . . . .	43
5.2	T-wave alternans . . . . .	44
<b>6</b>	<b>Numerical results</b>	<b>45</b>
6.1	Choice of the numerical scheme: ionic current integration . . . . .	45
6.1.1	Order of the splitting method . . . . .	48
6.1.2	General parameters . . . . .	49
6.2	Conduction velocity . . . . .	49
6.2.1	Relation with the mesh size . . . . .	49
6.2.2	Effect of anisotropy . . . . .	51
6.3	Restitution curves . . . . .	53
6.3.1	Electrical restitution of the RM and MM models . . . . .	53
6.3.2	Electrical restitution of the Fox model . . . . .	55
6.4	Pseudo-ECG . . . . .	55

6.4.1	Resolution of the linear system . . . . .	55
6.4.2	Results . . . . .	57
6.5	Alternans dynamics . . . . .	60
6.5.1	Fox model . . . . .	60
6.5.2	Spatial distribution in 3d tissues . . . . .	61
<b>7</b>	<b>Conclusions</b>	<b>65</b>
	<b>References</b>	<b>67</b>
	<b>Appendices</b>	<b>71</b>
<b>A</b>	<b>LifeV contributions</b>	<b>71</b>
A.1	/electrophysiology/solver . . . . .	71
A.1.1	/electrophysiology/solver/IonicModels . . . . .	71
A.2	/electrophysiology/examples . . . . .	72

# 1 Introduction

The heart's electrical activity is a key function of this organ. The electrical impulse propagation through the cells is responsible of muscle's contraction, and then of blood pumping into the whole body. Therefore a good comprehension of heart's electrical mechanisms is mandatory to model its physiological behavior. It is well known that disturbances in this electrical field could have very bad consequences on heart's functioning and lead to life treating effect. Electrophysiological models are used in order to have a better understanding of the underlying mechanisms involved in both normal and unhealthy hearts. This has been shown to bring about major improvements in the detection of heart's arrhythmias and diseases, as well as in their treatments.

In the first section, we present the theoretical background needed to provide a model of the heart's electrical activity. We deal with macroscopic behavior of general excitable media, and then we focus on the cardiac tissue specific nature. In this context, we discuss the reaction-diffusion problem for the initiation and propagation of an action potential wave, and we derive the monodomain equations from the bidomain formulation. Thereafter, at the microscopic level, we study the cellular membrane properties, and show how the action potential propagation is tightly linked to the ionic currents flowing through this membrane. We give a description of various ionic models with their underlying specific characters. The study of these theoretical aspects highlights the importance of an accurate description of physiological properties.

In the second section, we discuss the numerical methods used to discretize the monodomain diffusive equations with respect to the dimension of the simulation domain. Since 1d and 2d simulations are performed only on simple domains, an explicit finite difference discretization is adopted. However, in the 3d cases, we would prefer the finite element method. We are going to explain there two methods for the ionic current integration, with their advantages and limitations.

The third section deals with the electrocardiogram (ECG). Such signals give an interpretation of the heart's electrical activity over a period of time, as detected by electrodes placed on the body surface. This non-invasive device is widely used by medical doctors to measure and diagnose heart's disrhythmias. In the same way, it is interesting to reconstruct such signals from the transmembrane potential map: the pseudo-ECG. Thereby, we can have a characterization of the signals resulting from abnormalities in the action potential, which are related to the detection of arrhythmias or other heart's diseases. First, we present the theoretical derivation of this quantity, and then we analyze its numerical approximation. We particularly focus on the usage of the finite element basis to get the approximation of this signal.

In the fourth section, we present a specific disturbance of the cardiac rhythms: cardiac alternans. We concentrate on the alternation of the action potential duration, and we discuss the relation between this phenomenon and the electrical restitution of the underlying ionic cellular models. We present also a characterization of the alternans spatial distribution in the tissue, and finally explain how these alternans could be detected using an ECG signal.

In the final part, we characterize all the numerical results obtained and the simulations performed. First, we identify the most efficient numerical method in terms of accuracy and CPU time. Then, we look at the relation between the mesh size and the restitution of the conduction velocity. We note the necessity of fine tuning the mesh size to be able to get the correct conduction properties according to the physiological problem at hand. This issue is not easy and requires the implementation of higher order methods to increase the accuracy of the scheme. Once we have a satisfying numerical scheme and a sufficiently fine mesh, we can perform simulations in order to reproduce physiological behaviors. We start with the study of the

electrical restitution according to different ionic models using the restitution curves protocol. Afterwards, we build different pseudo-ECG signals to validate the computation of the approximation, initially in a normal rhythm case, and then during rhythm disorders. We verify that in all cases the pseudo-ECG is correctly correlated with the action potential's behavior. This results in a tool to detect disturbances of the cardiac rhythm. Lastly, we focus on the alternans dynamics. We begin with the discussion of specific ionic models developed to reproduce sustainable alternans in canine hearts. This model is useful to understand the microscopic mechanism of action potential duration alternans in a single cell and the related electrical restitution properties. However, this model is limited in the 3d case in terms of restitution accuracy and CPU consumption. A phenomenological model instead allows us to reproduce alternans in 3d tissue slabs. We look at the spatial distribution of the alternans and characterize the importance of anisotropy. In this case the patterns are related to the direction of the fibers and to the pacing site.

## 2 Mathematical models in electrophysiology

In this first section we will present the theoretical background needed to understand the electrical activity in excitable media and then we focus on the propagation of an electrical stimulus in cardiac tissue. We discuss also the specific geometry of such tissue and the influence of anisotropy.

Afterwards we analyze different ionic models that describe the electrical activity in a single cell, namely the ionic mechanisms underlying the initiation and propagation of an action potential, and we discuss the specifications of each of them.

The discussion of the mathematical model leads us to anticipate some problems related to the discretization of the model and the choice of an appropriate mesh to recover some important physiological properties.

### 2.1 Electrical activity in biological tissues

At a cellular level we describe the electrical potential as the *membrane* — or *transmembrane* — *potential*. It is defined by the difference between the intracellular and the extracellular potentials with respect to a generic reference potential. This potential is made up essentially by two contributions: electrical forces and diffusion.

The potential of an ion can be divided into two parts: the chemical potential and the electrical potential. The first one describes the uncharged part of the potential and is related to a diffusion process. The second one is the charged part and is described by the influence of electric fields [8]. We will discuss these two aspects separately.

#### 2.1.1 Derivation of the diffusion problem

We can see the diffusion process as the macroscopic result of the microscopic movement of particles. This irregular motion induces a regular movement in terms of the particles compound. The diffusion process of ions through the cellular membrane is related, in a linear approximation, to the Fick's laws [18].

The first Fick's law says that the flux  $J$  of an uncharged material — for example cell, amount of chemical, etc. — is proportional to the gradient of the concentration  $\phi$  of the material

$$J \propto -\nabla\phi \Leftrightarrow \exists D \text{ such that } J = -D\nabla\phi, \quad (2.1)$$

where  $D$  is the diffusivity coefficient. The minus sign indicates that the flux goes from high to low concentration. Using the mass conservation, if we suppose the absence of any chemical reaction, we obtain

$$0 = \frac{\partial\phi}{\partial t} + \nabla \cdot J = \frac{\partial\phi}{\partial t} - \nabla \cdot (D\nabla\phi).$$

So, we have

$$\frac{\partial\phi}{\partial t} = \nabla \cdot (D\nabla\phi)$$

and if  $D$  is constant

$$\frac{\partial\phi}{\partial t} = D\Delta\phi.$$

**Unidimensional random walk process** In the unidimensional case, the diffusion process could be described as a simple random walk process [36]. We allow the particles to move randomly on a 1d-axis. During a time step  $\Delta t$  the particle can move forward or backward by a fixed step  $\Delta x$ . Thus, after  $N\Delta t$  steps, the particle lies between  $-N\Delta x$  and  $N\Delta x$ .

To study the motion of a particle we need to describe the probability  $p(m, n)$  for a given particle to reach a point,  $m$  space steps to the right, after  $n$  time steps. We suppose that the particles goes  $a$  steps to the right and  $b$  steps to the left. So we have

$$m = a - b, \quad n = a + b.$$

The number of possible paths to reach  $x = m\Delta x$  is given by

$$N_p = \frac{n!}{a!b!} = \frac{n!}{a!(n-a)!}$$

and the number of all the paths is  $N_{tot} = \frac{1}{2^n}$ . Therefore the probability is given by

$$p(m, n) = \frac{N_p}{N_{tot}}.$$

Since

$$(x + y)^n = \sum_{m=-n}^n \frac{n!}{a!(n-a)!} x^a y^{n-a},$$

we get

$$\sum_{m=-n}^n p(m, n) = \sum_{m=-n}^n \frac{n!}{a!(n-a)!} \left(\frac{1}{2}\right)^a \left(\frac{1}{2}\right)^{n-a} = \left(\frac{1}{2} + \frac{1}{2}\right)^n = 1$$

and  $p(m, n)$  is therefore the binomial distribution whose asymptotic approximation is given by the normal distribution, i.e.

$$p(m, n) \sim \left(\frac{2}{\pi n}\right)^{\frac{1}{2}} \exp\left(-\frac{m^2}{2n}\right), \quad m \gg 1, \quad n \gg 1.$$

Set  $m\Delta x = x$ ,  $n\Delta t = t$  for some continuous variables  $x$  and  $t$ . For  $x, t$  finite, if we let  $\Delta x$  and  $\Delta t$  go to zero, the number of points along the axis becomes infinite and so

$$p(m, n) \rightarrow 0, \quad \text{as } \Delta x, \Delta t \rightarrow 0.$$

The probability of finding the particle in the interval  $(x, x + \Delta x)$  at time  $t$  is given by

$$\frac{p\left(\left(\frac{x}{\Delta x}\right), \left(\frac{t}{\Delta t}\right)\right)}{2\Delta x} \sim \left(\frac{\Delta t}{2\pi t(\Delta x)^2}\right)^{\frac{1}{2}} \exp\left(-\frac{x^2}{2t(\Delta x)^2}\right).$$

We define the *diffusion coefficient*  $D$  as

$$0 \neq D = \lim_{\Delta x, \Delta t \rightarrow 0} \frac{(\Delta x)^2}{\Delta t}. \quad (2.2)$$

It has the dimension of  $\frac{(\text{length})^2}{\text{time}}$  and represents how efficiently particles disperse from high to low concentration. Finally the distribution of the particles is given by

$$u(x, t) = \lim_{\Delta x, \Delta t \rightarrow 0} \frac{p\left(\left(\frac{x}{\Delta x}\right), \left(\frac{t}{\Delta t}\right)\right)}{2\Delta x} = \left(\frac{1}{4\pi Dt}\right)^{\frac{1}{2}} \exp\left(-\frac{x^2}{4Dt}\right). \quad (2.3)$$

### Remark 2.1

We see from equation (2.3) that the probability distribution  $p(\cdot)$  is nonlinearly related to the diffusion coefficient. So we have to be careful in the definition of this coefficient, in view of the numerical models we will develop.

The definition of the coefficient (2.2) tells us that the space discretization has to be sufficiently small according to the diffusivity to guaranty the right evaluation of the diffusion coefficient. This first consideration warns us about the importance of the mesh size in the further simulations.

For more details about the derivation of the diffusion coefficient we can refer to [36].



**Diffusion through a membrane** We use the Ohm's law to describe the diffusion process through a membrane of thickness  $L$ , which can be seen as a separation between two large reservoirs  $r_l$  and  $r_r$  of chemical species with concentrations  $c_l$  and  $c_r$ . The diffusion equation in the membrane gives

$$\frac{\partial c}{\partial t} = D \frac{\partial^2 c}{\partial x^2}$$

with the boundary conditions  $c(0, t) = c_l$  and  $c(L, t) = c_r$ . Here we need only the steady state, i.e.  $\frac{\partial c}{\partial t} = 0$ , solution, that is

$$\frac{\partial J}{\partial x} = -D \frac{\partial^2 c}{\partial x^2} = 0 \Rightarrow J = -D \frac{\partial c}{\partial x} = \text{constant}.$$

So we deduce that  $c(x) = ax + b$  for some constants  $a$  and  $b$ . Applying the boundary conditions, we get

$$c(x) = c_l + (c_r - c_l) \frac{x}{L}.$$

From Fick's law, the flux is constant and independent of  $x$ . Hence, we have

$$J = \frac{D}{L}(c_l - c_r).$$

### 2.1.2 Reaction-diffusion equations

Since the transmembrane potential is induced by the diffusion of charged ions through the cellular membrane, we can't describe it only by a simple diffusion process. The potential is also under the influence of electrical fields and active transport processes. These introduce in the previous problem a reaction term which depends on the ionic model.

We will discuss the general derivation of the reaction-diffusion equations. After that we will see how the reaction term is derived in terms of the electrical properties of the cellular membrane.

**General derivation of the reaction-diffusion equation** For an arbitrary surface  $S$  enclosing a volume  $V$  in a three dimensional space, we have the following integral conservation relation for the scalar field  $\phi$ :

$$\frac{\partial}{\partial t} \int_V \phi(\mathbf{x}, t) dV = - \int_S J \cdot dS + \int_V f(\mathbf{x}, t, \phi) dV.$$

This equation says that the rate of change of an amount of material in  $V$  is equal to the sum of rate of flow of material across  $S$  into  $V$  and the created/dissolved material. By the divergence theorem and the continuity of  $\phi(\cdot, \cdot)$ , we have

$$\int_V \left( \frac{\partial \phi}{\partial t}(\mathbf{x}, t) - \nabla \cdot J + f(\mathbf{x}, t, \phi) \right) dV = 0,$$

and that relation has to be valid for any volume  $V$ . So this implies the local form

$$\frac{\partial \phi}{\partial t}(\mathbf{x}, t) - \nabla \cdot J + f(\mathbf{x}, t, \phi) = 0. \quad (2.4)$$

Moreover this equation is valid for any kind of flux  $J$  and thus also for a classic Fick diffusion flux given by  $J = -\nabla \phi$ . For this specific flux, equation (2.4) becomes

$$\frac{\partial \phi}{\partial t} = f + \nabla \cdot (D \nabla \phi).$$

This relation can be generalized for several chemical species by the matrix formulation

$$\frac{\partial \mathbf{u}}{\partial t} = \mathbf{f} + \nabla \cdot (D \nabla \mathbf{u}),$$

where  $D$  is the matrix of diffusivities.

### 2.1.3 Electrical properties of the cell membrane

The cell membrane provides a separation between the intracellular and the extracellular spaces. It is selectively permeable depending on the ionic species and particles, going through passive transport or active processes. The active transport processes of ions is needed to regulate the intracellular ionic composition of the cell and the cellular volume. The ionic transportation of the ions generates a potential difference across the cellular membrane and thus induces an electrical field. The most important process is the diffusion related to the concentration gradient. The concentration differences are setted up and maintained by active mechanisms using energy to pump ions against their gradient concentrations. Many of these pumps are dedicated to a specific type of ion.

**Nernst potential** The Nernst equation is one of the most important relation in electrophysiology. This equation describes how the differences in ionic concentrations result in potential differences. This is related to the selective permeability of the membrane allowing the flow of specific ions to create a difference of charge across the membrane. The equilibrium is reached when the electric field exactly balances the diffusion of ions. At equilibrium the potential difference  $\phi$  across the cell membrane is given by the *Nernst potential*

$$\phi_{eq} = \phi_i - \phi_e = \frac{RT}{zF} \ln \left( \frac{[S]_e}{[S]_i} \right), \quad (2.5)$$

where the subscripts  $i$  and  $e$  refer to intracellular and extracellular spaces, respectively (see [28]). The constant  $R$  is the universal gas constant,  $T$  is the absolute temperature,  $F$  is Faraday's constant and  $z$  is the valence of the ion  $S$ . The full derivation of the Nernst equation can be found in [16].

**Electrical circuit model** As the cellular membrane separates the charges, it can be viewed as a capacitor. The capacitance of an insulator is given by the ratio of the charge  $Q$  across the capacitor to the voltage potential  $\phi$  needed to hold that charge, i.e.

$$C_m = \frac{Q}{\phi}.$$

Since the current is defined by  $\frac{dQ}{dt}$ , the current associated to the capacitor is given by

$$i_c = C_m \frac{d\phi}{dt}.$$

The part of the current due to the resistors — which are here the ion channels — is given in a linear approximation by the Ohm's laws and is defined by

$$i_r = \frac{\phi}{R_m} = I_{ion}.$$

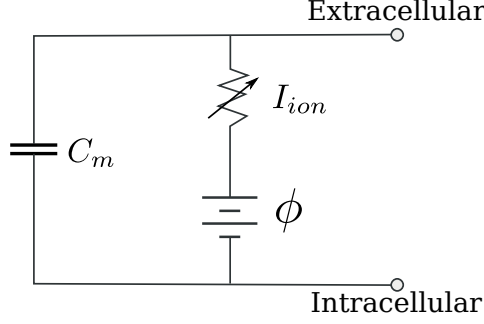


Figure 2.1: Equivalent electric circuit for the cellular membrane.

Since there can be no build up of charge on either side of the membrane, the sum of the capacitive and ionic currents must be zero, and so we get

$$i_c + i_r = C_m \frac{d\phi}{dt} - I_{ion} = 0. \quad (2.6)$$

The equivalent electric circuit is shown in Figure 2.1. For more details, see [28].

### Remark 2.2

This equation is used to model the electrical potential in a single cell. If we want to induce an action potential by applying a stimulus, the equation becomes

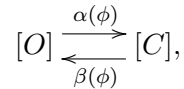
$$C_m \frac{d\phi}{dt} - I_{ion} + I_{app} = 0,$$

where  $I_{app}$  represents the applied stimulus.

The ionic current  $I_{ion} = I_{ion}(\phi)$  must be defined in generalized nonlinear terms, thanks to the generalized Ohm's law [50]. This issue is very challenging. Many ionic models have been developed based on phenomenological or physiological properties. Some of those are presented in Section 2.4.

**Gating variables** The cellular membrane separates the extracellular and the intracellular spaces. To maintain the right concentration of each kind of ions, it allows some ionic exchanges between these two spaces. The membrane encloses some channels and each of them allows the passage of some specific ions. The channels could be either a pump or an exchanger. These ionic exchanges are needed to generate and maintain a potential difference across the membrane. The channels open or close according to the ionic concentrations and the electrical fields. Their opening states are related to electric stimuli. Each channel is made of sub-units and each of them could be open or closed.

We denote by  $[O]$  (resp.  $[C]$ ) the ionic concentrations in the open (resp. closed) channels. The transition from the open state to the closed state can be summarized as a kinetic relation



where  $\alpha(\phi)$  is the probability for this channel to go from the open state to the closed state and  $\beta(\phi)$  the opposite direction. Using the law of mass action [28], we have

$$\frac{d[O]}{dt} = \alpha(\phi)[C] - \beta(\phi)[O]. \quad (2.7)$$

Setting  $g = [O]/([O] + [C])$  and dividing the equation (2.7) by the full ionic concentration  $[O] + [C]$ , we get

$$\frac{dg}{dt} = \alpha(\phi)(1 - g) - \beta(\phi)g. \quad (2.8)$$

Hence, we can understand  $g$  as the probability that the channel  $g$  is open. These variables are called *gating variables* [27]. Sometimes equation (2.8) is written as

$$\frac{dg}{dt} = \frac{g_\infty(\phi) - g}{\tau_g(\phi)},$$

where  $g_\infty(\phi) = \frac{\alpha(\phi)}{\alpha(\phi) + \beta(\phi)}$  and  $\tau_g(\phi) = \frac{1}{\alpha(\phi) + \beta(\phi)}$ . In general, these values are determined experimentally.

For a channel made of  $n$  identical sub-units, the probability  $O$  that the channel is open, is given by

$$O = g^n.$$

A channel can also be made of different sub-units which are associated with a probability  $g_i$  to be open and related to the coefficients  $\alpha_{g_i}, \beta_{g_i}$  defined by (2.8).

Given the probability  $O$ , we can define the current flowing across the cellular membrane: the current is given by the product of the maximal current and the proportion of open channels. For the maximal conductance  $G_{max}$ , i.e. when all the channels are open, the current is given by

$$I = G_{max}O(\phi - \phi_{eq}), \quad (2.9)$$

where  $\phi_{eq}$  is the Nernst equilibrium potential (2.5) associated to each ion.

#### 2.1.4 Cable equation

First we want to describe the propagation of an action potential along a single fiber. This model is useful for describing the evolution of the action potential in an axon, a muscle fiber or any other single fiber.

The cable model is based on an infinitely long fiber with constant cross section. We use the theory of electric circuit to model the propagation of the potential along the fiber [42], see Figure 2.2.

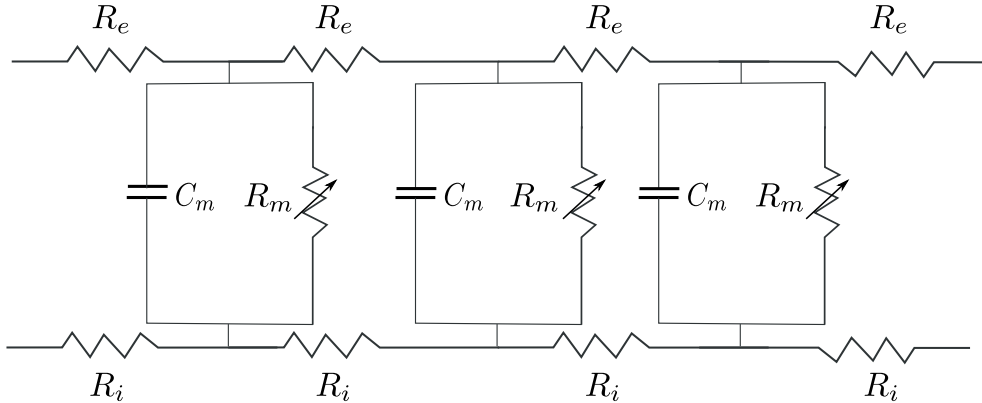


Figure 2.2: Equivalent electric circuit representation to derive the cable equation. The subscripts  $i$  refer to intracellular,  $e$  to extracellular and  $m$  to membrane.

As discussed before, each cell is represented by a capacitor  $C_m$  in parallel with a resistive component  $R_m$ . The intracellular space within the fiber is modelled using resistances  $R_i$  in series and the extracellular space surrounding the fiber is modelled using resistances  $R_e$  in series.

We consider a fiber of length  $l$  with an intracellular cross sectional area  $A_i$  and an extracellular cross sectional area  $A_e$ . So the resistivities in these spaces become

$$r_i = \frac{R_i A_i}{l}, \quad r_e = \frac{R_e A_e}{l}.$$

From Ohm's law, the change of the potential in each parts is given by

$$\frac{d\phi_i}{dx} = -I_i r_i, \quad \frac{d\phi_e}{dx} = -I_e r_e, \quad (2.10)$$

where  $I_i$  (resp.  $I_e$ ) is the current flowing in the intracellular (resp. extracellular) space along the fiber axis.

Since the intracellular and extracellular potentials are rarely equal, there is a driving force inducing a transversal current across the membrane. We denote this current by  $I_m$  and we follow the convention that it is positive if it goes from the intracellular to the extracellular space.

From the Kirchhoff's first law, we have the following expressions for the currents variation:

$$\frac{dI_i}{dx} = -I_m, \quad \frac{dI_e}{dx} = I_m.$$

Combining this with (2.10), we get

$$-I_m = \frac{dI_i}{dx} = \frac{d}{dx} \left( -\frac{1}{r_i} \frac{d\phi_i}{dx} \right) = -\frac{1}{r_i} \frac{d^2\phi_i}{dx^2}$$

and, in a similar manner,

$$\frac{d^2\phi_e}{dx^2} = -I_m r_e.$$

Since the transmembrane potential is given by  $\phi = \phi_i - \phi_e$  and using the last two relations we get

$$I_m = \frac{1}{r_i + r_e} \frac{\partial^2 \phi}{\partial x^2}. \quad (2.11)$$

This expression is equally applicable for a passive or an active description of the membrane [42]. The electrical analogue for the passive membrane is derived in (2.6), where  $I_{ion}$  is here given by  $I_{ion} = \frac{\phi}{R_m}$  with  $R_m$  the membrane resistance associated to the ionic channels. If the ratio of membrane area associated to a given volume is given by  $A_m$ , the current along the fiber per unit of volume becomes

$$I_m = A_m \left( C_m \frac{\partial \phi}{\partial t} + \frac{\phi}{R_m} \right). \quad (2.12)$$

Combining equations (2.11) and (2.12) gives the reaction-diffusion equation perscribed by the cable theory for a passive membrane

$$\frac{1}{r_i + r_e} \frac{\partial^2 \phi}{\partial x^2} = A_m \left( C_m \frac{\partial \phi}{\partial t} + \frac{\phi}{R_m} \right).$$

Often we use the conductances  $\sigma_i = \frac{1}{r_i}$  and  $\sigma_e = \frac{1}{r_e}$  instead of the resistivities. Using  $I_{ion}$  to represent the sum of the ionic currents, the final form of the active cable equation is

$$\frac{\sigma_i \sigma_e}{\sigma_i + \sigma_e} \frac{\partial^2 \phi}{\partial x^2} = A_m \left( C_m \frac{\partial \phi}{\partial t} + I_{ion}(\phi) \right). \quad (2.13)$$

**Conduction velocity** The cardiac tissues are excitable conductive media: when an action potential is generated somewhere in the tissue, it will propagate in the whole tissue. An electrical stimulation induces an action potential wave leaving from the pacing site and travelling through the tissue. The propagation is related to the electrical conductivity of the medium. Indeed, the wave front travels faster in the direction of the muscular fibers than orthogonal to these. The *conduction velocity* is the velocity of the wave front along the propagation direction and it is defined by

$$CV = \frac{\Delta x}{\Delta t},$$

where  $\Delta x$  is the distance covered by the action potential wave and  $\Delta t$  is the difference between the two corresponding activation times. The involved quantities are illustrated in Figure 2.3.

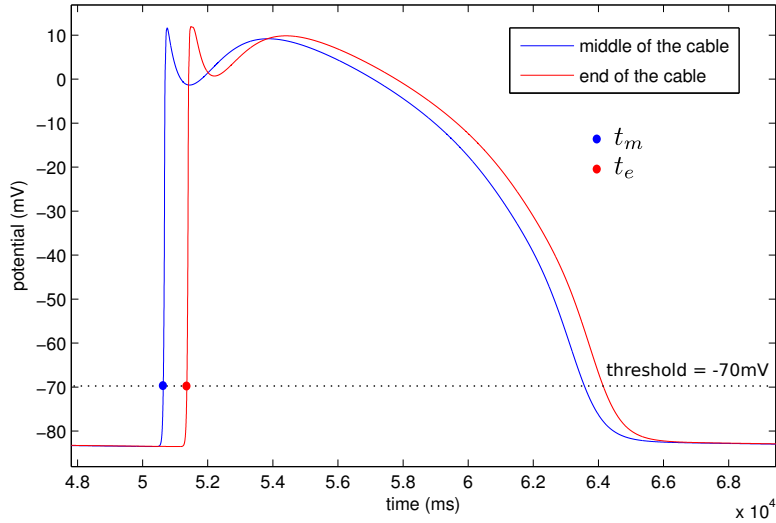


Figure 2.3: Propagation of the action potential in a cable. The conduction velocity is given by  $CV = \frac{\Delta x}{\Delta t}$ , where  $\Delta t = t_e - t_m$  and  $\Delta x = x_e - x_m$ , the coordinates of the middle and the end point of the cable.

The conduction velocity is an important property and we have to be careful that it is correctly reproduced by the numerical model we will choose. Furthermore we will see that it is related to the choice of the mesh size. Thus we must pay attention to the choice of the space discretization.

**Bistable equation** The bistable equation is a special case of the cable equation (2.13) where the ionic current  $I_{ion}(\phi)$  has a specific cubic form. For simplicity, we reduce the equation (2.13) to

$$\frac{\partial \phi}{\partial t} = D \frac{\partial^2 \phi}{\partial x^2} + I_{ion}(\phi), \quad (2.14)$$

where  $I_{ion}(\phi)$  has three zeros at 0,  $\alpha$  and 1,  $0 < \alpha < 1$ . The values  $\phi = 0$  and  $\phi = 1$  are stable steady solutions of the ordinary differential equation  $\frac{d\phi}{dt} = I_{ion}(\phi)$ , where  $\phi$  could be rescaled to satisfy this property.

Some examples of such functions and the associated analytic solution of the bistable equation are presented in [28] and [13].

We are interested in the relation between the propagation of travelling waves and the conduction velocity. Namely, we want to analyse the condition on the diffusion coefficient for a

wave going from a cell to another. As cells are discrete entities, we look at a discrete form — in space — of the simplified cable equation (2.14)

$$\frac{d\phi_n}{d\tau} = I_{ion}(\phi_n) + D(\phi_{n+1} - 2\phi_n + \phi_{n-1}), \quad (2.15)$$

where  $\tau = \frac{t}{R_m C_m} = \frac{t}{\tau_m}$  is the dimensionless time and  $D = \frac{R_m}{\mu L p (r_i + r_e)}$  is the diffusion coupling coefficient. The parameters  $\mu$ ,  $L$ ,  $p$ ,  $R_m$  are the length of the nodes, the distance between two nodes, the perimeter of the cable and the resistivity of the membrane, respectively.

If a travelling wave solution exists, it satisfies the property

$$\phi_{m+1} = \phi_m(\tau - \tau_d),$$

for some time delay  $\tau_d$ , see [28]. Furthermore, if  $\phi_m(\tau) = \phi(\tau)$ , it satisfies the differential equation

$$\frac{d\phi}{d\tau} = D(\phi(\tau + \tau_d) - 2\phi(\tau) + \phi(\tau - \tau_d)) + I_{ion}(\phi).$$

Since  $\phi$  is sufficiently smooth and  $\tau_d$  is sufficiently small, we can approximate  $\phi(\tau + \tau_d)$  by its Taylor series  $\phi(\tau + \tau_d) = \sum_{n=0}^{\infty} \frac{1}{n!} \phi^{(n)}(\tau) \tau_d^n$ . Ignoring terms of order six and higher, the differential equation is approximated by

$$D \left( \tau_d^2 \phi_{\tau\tau} + \frac{\tau_d^4}{12} \phi_{\tau\tau\tau\tau} \right) - \phi_{\tau} + I_{ion}(\phi) = 0,$$

and if  $\tau_d$  is small enough, it reduces to

$$D\tau_d^2 \phi_{\tau\tau} - \phi_{\tau} + I_{ion}(\phi) = 0. \quad (2.16)$$

Every travelling wave satisfying  $U_{\tau\tau} - cU_{\tau} + I_{ion}(U) = 0$ ,  $\phi_0(\tau) = U(c\tau)$  for  $D = \frac{1}{\tau_d^2 c^2}$  is solution of (2.16), where  $c$  is the dimensionless wave speed for the continuous equation. We saw that the conduction velocity  $CV$  is given by the internodal distance divided by the time delay. In this specific case we get

$$CV = \frac{L + \mu}{\tau_d \tau_m} = (L + \mu)c \frac{\sqrt{D}}{\tau_m}.$$

While the continuous equation allows the wave propagation for all coupling strength, the discrete system has a coupling threshold for the wave propagation [28].

### Remark 2.3

From a numerical analysis point of view, it is interesting to see that the spatial discretization has an effect on the conduction velocity. Therefore we have to pay attention to this aspect for the further numerical simulations.

In the discrete system, the propagation depends on the choice of the parameters and may fail if the coupling coefficient —related to the conduction velocity and the internodal distance — between two consecutive cells is too small. Indeed if the effective internodal resistance is large the propagation cannot go to the next node because the current from an excited node to an unexcited node is too small to achieve the threshold potential of the unexcited node.

This result is demonstrated in [28] using the maximum principle and some comparison arguments: we first look for a standing solution of the discrete bistable equation (2.15). It is known that if a set of initial data for the discrete bistable equation is ordered, then the corresponding solutions remain ordered for any time. Therefore, if the discrete bistable equation has a monotone increasing stationary front solution, there cannot be a travelling wave solution.

A standing front solution of the discrete bistable equation is a sequence  $\{\phi_n\}$  satisfying the finite difference equation

$$0 = D(\phi_{n+1} - 2\phi_n + \phi_{n-1}) + I_{ion}(\phi_n),$$

$$\forall n \in \mathbb{N} \text{ such that } \phi_n \rightarrow 1, \text{ as } n \rightarrow \infty \text{ and } \phi_n \rightarrow 0, \text{ as } n \rightarrow -\infty.$$

Since for any bistable function there is a number  $D^* > 0$ , such that  $D \leq D^*$ , the discrete bistable equation has a standing solution, that is, propagation fails [29].

We can find the calculation of such a  $D^*$  in [28] for the special case where

$$I_{ion}(\phi) = -\phi + H(\phi - \alpha), \quad 0 < \alpha < 1,$$

where  $H(\cdot)$  is the Heaviside step function [35].

## 2.2 Description and properties of the cardiac action potential

The action potential is an excitation phenomenon which occurs in excitable cells. This short-lasting event makes the membrane potential increasing very fast and then decreasing until recovering the resting potential. Action potentials are supported by special types of voltage-gated ion channels embedded in the cell's plasma membrane. This induces first a depolarization of the cellular membrane and then a progressive repolarization due to the complex mechanisms of the ion channels. After that there is an equilibrium phase that lasts longer, until the total repolarization of the cell.

The course of the action potential can be divided in five phases, reported in Figure 2.4:

- Phase 0: rapid depolarization. This first phase is almost exclusively due to a rapid influx of sodium ions in the cell which is generally induced by an external stimulus.
- Phase 1: partial repolarization. This short partial repolarization phase is induced mainly by an outward current of potassium.
- Phase 2: plateau. The existence and the duration of this phase is related to the flow of calcium ion. We have a plateau phase when the amount of charge carried by the inward calcium current equals the amount of charge carried by the outward potassium current.
- Phase 3: repolarization. This is a long period of slow repolarization, the potential decreases slowly. The current of calcium ion ceases while the outward potassium current remains and the repolarization of the cell becomes faster.
- Phase 4: resting potential. The repolarization ends and the ionic concentrations recover their resting values. Therefore the equilibrium transmembrane potential is restored.

**Specific quantities associated to an action potential** At the baseline state, the membrane potential is held at a relatively stable value, called the *resting potential*. When the voltage is brought to a more positive value, the cell reaches a depolarization phase. A large depolarization during a short period of time generates an *action potential* which is related to certain voltage-gated ion channels [5].

If we consider a threshold for the value of the potential, the *action potential duration (APD)* is defined as the amount of time during which the action potential is greater than a fixed threshold value.



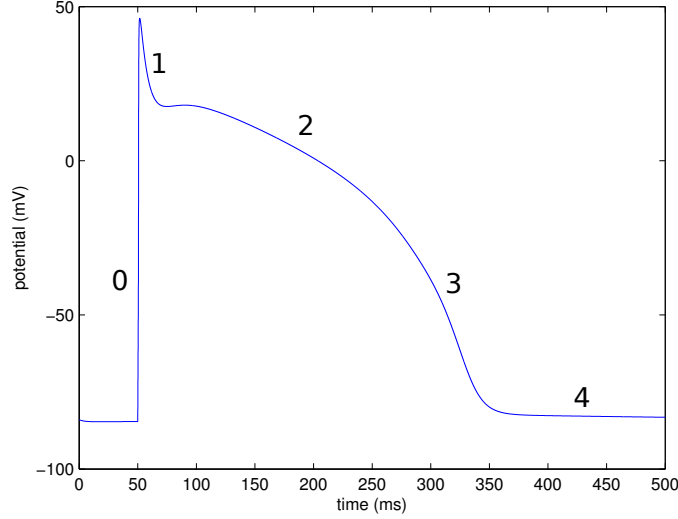


Figure 2.4: Typical shape of a cardiac action potential divided into five phases: rapid depolarization (0), partial repolarization (1), plateau (2), repolarization (3) and resting potential (4).

If several action potentials occur, the *diastolic interval* ( $DI$ ) is given by the duration of the interval between two action potentials. During this period the potential is approximately equal to its resting value.

The *cycle length* ( $CL$ ) is the period between the beginning of two action potentials and coincides with the period of stimulation. Namely, we have an iterative map law [48]

$$CL = APD + DI.$$

All these quantities are illustrated in Figure 2.5.

**Generation and propagation of an action potential** The spread and propagation of the electrical activation in the heart follow specific pathways and can be differentiated according to each different muscular entity. The shape of the action potential is specific to each of them. A schematic representation of this is shown in Figure 2.6.

### 2.3 Cardiac tissue modeling

The cardiac muscle has a very specific architecture and its conduction properties are closely related to this composition. Cardiac tissue is an anisotropic media and we will see later in details how to characterize its anisotropy.

The cardiac muscle consists of densely packed cells, the cardiac myocytes, which are more or less cylindrical. Due to membrane property and organization of the cells, the ionic currents encounter an easier path in the longitudinal than in the orthogonal direction to the main axis of the cell. So the resulting mean electrical conductivity is much higher in the direction of the fiber.

The myocytes are organized in fiber-like array and the fibers are then arranged in sheets. Therefore the fibers form discrete layers, the sheets, and, for the ventricular wall, these are radially oriented with respect to the ventricular surface. Such a complex structure induces a rotational propagation direction to the action potential.

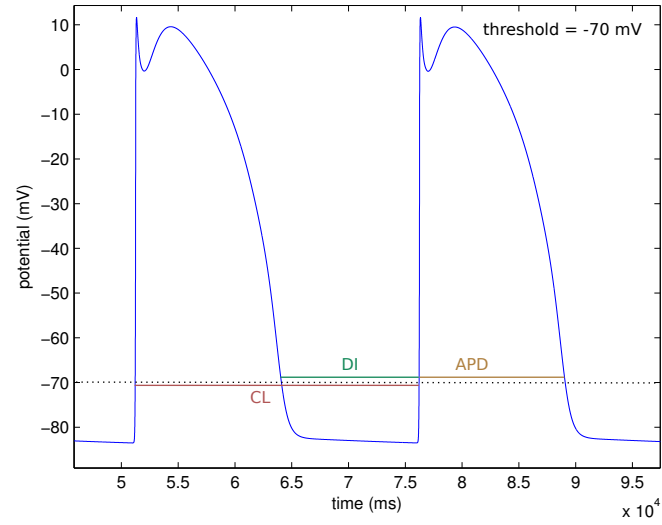


Figure 2.5: Main quantities associated to the action potential.

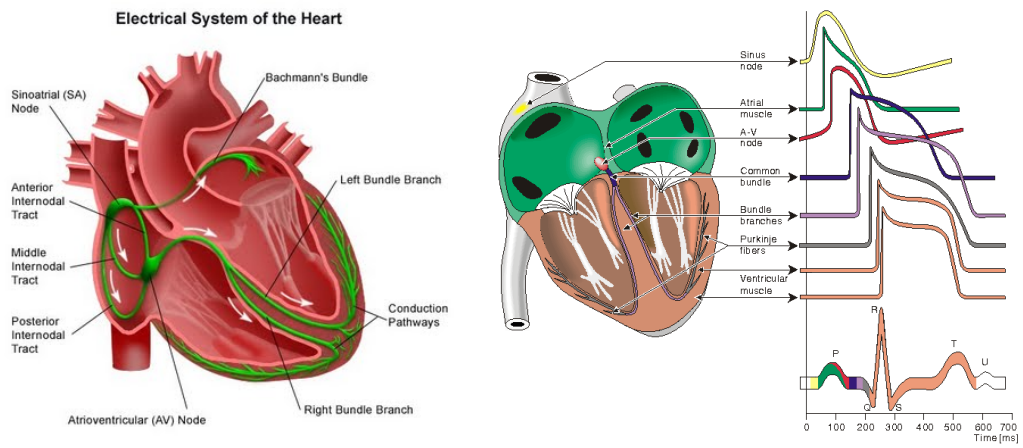


Figure 2.6: Left: Cardiac activation network, pathways from atria to ventricles. Right: Action potentials morphology at the different levels of the activation network [33].

Since the composition of the cardiac muscle has a great influence on its electrical activity, we need a good description of it to reproduce correctly its physiological behavior. The anatomical constitution of the heart has been studied extensively in [31] and this paper provides good descriptions of the organization of fibers. We see in Figure 2.7 the fibers orientation in the ventricles.

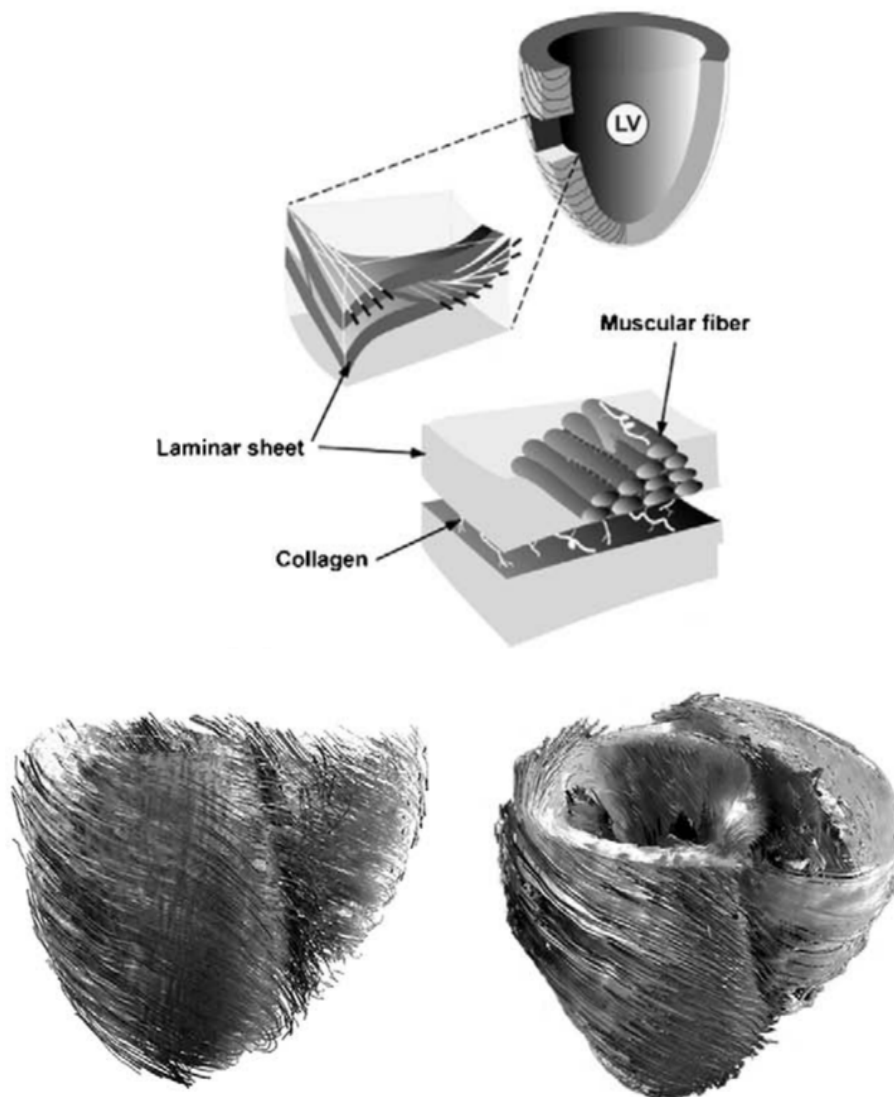


Figure 2.7: Top: Schematic of cardiac microstructure. Tissue block contains layers of tightly coupled myocytes-laminar sheets. The cardiac myocytes (fibers) are tightly coupled within the same, but sparsely coupled between the adjacent laminas. The planes of the laminas could be defined locally by the longitudinal axis of comprising myocardial fibers and by their spiral, branching transmurular direction on the ventricular mass level. Bottom: Reconstruction of the ventricular fibers. [31].

Taking into account these considerations, we want to derive a model for the evolution of the electrical potential in cardiac tissue. The further models are continuum models in the sense that they are based on average properties taken on many cells.

### 2.3.1 Bidomain model

We want to describe the transmembrane potential, i.e. the difference between the electrical potential inside and outside each cell along the membrane. We suppose that either the extracellular and the intracellular spaces are continuum media and fill the whole space. This implies the existence of gap junctions between these two spaces: the ionic channels, for more details see 2.1.3.

We denote by  $\phi_i$  and  $\phi_e$  the intracellular (resp. extracellular) potential. These quantities are determined by average on small volumes. We suppose that in each point  $x$  of the domain we have an intracellular potential  $\phi_i(x)$  and an extracellular potential  $\phi_e(x)$ . We consider the cell membrane as an electric insulator and therefore it is possible to have a difference of potential between inside and outside the cell. In addition, this allows a separation of charge across the membrane. The difference  $\phi = \phi_i(x) - \phi_e(x)$  is the *transmembrane potential*.

In the following we consider that the currents are quasi-static —satisfy the Fick's law— and hence the intracellular (resp. extracellular) currents are given by:

$$\begin{aligned} J_i &= -D_i \nabla \phi_i, \\ J_e &= -D_e \nabla \phi_e, \end{aligned}$$

where  $D_i$  and  $D_e$  are the conductivities in each parts.

We suppose that there is no source of charge but that we can have a charge accumulation in one point of the domain. Since the cell membrane is very thin, a charge accumulation on one side will create the same accumulation of charge in the other side. Finally, at each point, the charge accumulation must be zero:

$$\frac{\partial}{\partial t}(q_i + q_e) = 0,$$

where  $q_i$  and  $q_e$  are the intracellular (resp. extracellular) charges.

The current at a point of the domain is given by the sum of the rate of charge accumulation in this point and the ionic current flowing outside the domain from this point, namely:

$$-\nabla \cdot J_i = \frac{\partial q_i}{\partial t} + \chi I_{ion}, \quad (2.17)$$

$$-\nabla \cdot J_e = \frac{\partial q_e}{\partial t} - \chi I_{ion}, \quad (2.18)$$

where  $\chi$  is the surface-volume ratio and  $I_{ion}$  is the ionic current through the cell membrane. By convention, the positive way goes from inside to outside the cell.

Equations (2.17) and (2.18) confirm that the full current is conserved. Indeed, we have

$$\begin{aligned} \nabla \cdot J_i + \nabla \cdot J_e &= -\frac{\partial q_i}{\partial t} - \chi I_{ion} - \frac{\partial q_e}{\partial t} + \chi I_{ion} \\ &= -\frac{\partial}{\partial t}(q_i + q_e) = 0. \end{aligned}$$

The amount of charge that can be separated by the cell membrane is related to the electrical potential and also to the capacity  $C_m$  of the membrane. Since  $\phi = \phi_i - \phi_e$ , setting  $q = \frac{1}{2}(q_i - q_e)$ , we get

$$\phi = \frac{q}{\chi C_m}.$$

Hence, this gives

$$\begin{aligned}
C_m \chi \frac{\partial \phi}{\partial t} &= \frac{\partial q}{\partial t} = \frac{1}{2} \frac{\partial (q_i - q_e)}{\partial t} \\
\Leftrightarrow \quad \frac{\partial q_i}{\partial t} &= -\frac{\partial q_e}{\partial t} = C_m \chi \frac{\partial \phi}{\partial t} \\
\Leftrightarrow \quad -\nabla \cdot J_i &= C_m \chi \frac{\partial \phi}{\partial t} + \chi I_{ion}.
\end{aligned}$$

Finally, for  $\phi_i = \phi - \phi_e$ , we get the standard formulation of the bidomain equations [49]:

$$\begin{cases} \nabla \cdot (D_i \nabla \phi) + \nabla \cdot (D_i \nabla \phi_e) = C_m \chi \frac{\partial \phi}{\partial t} + \chi I_{ion}, \\ \nabla \cdot (D_i \nabla \phi) + \nabla \cdot ((D_i + D_e) \nabla \phi_e) = 0. \end{cases} \quad (2.19)$$

To solve the differential system (2.19), we have to define the boundary conditions associated to the variables  $\phi$  and  $\phi_e$ . For this purpose, we suppose that the heart is embedded in a non-conductive medium, i.e.,

$$n \cdot J_i = 0 \quad \text{and} \quad n \cdot J_e = 0,$$

on the boundary of the domain. Hence, for a domain  $\Omega$ , we get the following system of partial differential equations:

$$\begin{aligned}
\nabla \cdot (D_i \nabla \phi) + \nabla \cdot (D_i \nabla \phi_e) &= C_m \chi \frac{\partial \phi}{\partial t} + \chi I_{ion}, & \text{in } \Omega, \\
\nabla \cdot (D_i \nabla \phi) + \nabla \cdot ((D_i + D_e) \nabla \phi_e) &= 0, & \text{in } \Omega, \\
n \cdot (D_i \nabla \phi + D_i \nabla \phi_e) &= 0, & \text{on } \partial\Omega, \\
n \cdot (D_e \nabla \phi_e) &= 0, & \text{on } \partial\Omega.
\end{aligned} \quad (2.20)$$

**Remark 2.4** (Existence of weak solutions)

By imposing some regularity conditions on the domain and the functional spaces, it is possible to show that, under some hypothesis, the problem (2.20) has a unique weak solution. The full demonstration of this result is presented in [22].

### 2.3.2 Monodomain model

The bidomain equations can be simplified if we suppose that the intracellular and the extracellular spaces has the same kind of anisotropy, namely

$$D_e = \lambda D_i, \quad \lambda \in \mathbb{R}. \quad (2.21)$$

With this supposition, system (2.20) becomes

$$\nabla \cdot (D_i \nabla \phi_e) = -\frac{1}{1+\lambda} \nabla \cdot (D_i \nabla \phi)$$

and we need to solve only

$$\begin{aligned}
\left(\frac{\lambda}{1+\lambda}\right) \nabla \cdot (D_i \nabla \phi) &= C_m \chi \frac{\partial \phi}{\partial t} + \chi I_{ion}, & \text{in } \Omega, \\
n \cdot (D_i \nabla \phi) &= 0, & \text{on } \partial\Omega.
\end{aligned} \quad (2.22)$$

### 2.3.3 Geometry of the cardiac tissue

Cardiac tissue has very specific conduction properties. Because of its composition in sheets and fibers, it is an anisotropic medium. It is possible to characterize this anisotropy and to derive a description of the tensor of conductivities  $D$ . First, we build a system of coordinates  $\{a_l, a_t, a_n\}$  where  $a_l$  is direction along a fiber,  $a_t$  and  $a_n$  are perpendicular to the fiber with  $a_t$  in the plan of the sheet and  $a_n$  in the plane othogonal to the sheet. In this system of coordinates, the conductivity tensor becomes

$$D^\star = \begin{bmatrix} \sigma_l & 0 & 0 \\ 0 & \sigma_t & 0 \\ 0 & 0 & \sigma_n \end{bmatrix}, \quad (2.23)$$

where the  $\star$  refers to the local coordinates.

In this project, the only anisotropic domain we will consider is a parallelepipedal slab of ventricular tissue. In this case the sheets are planes — let say parallel to the  $O_{xy}$  plane — and the fibers are straight lines. The orientation of the fibers depends on the  $z$ -coordinate with a rotation angle from  $60^\circ$  on the endocardium ( $z = 1$ ) to  $-60^\circ$  on the epicardium ( $z = 0$ ) [17]. The fibers orientation associated to the domain is shown on Figure 2.8.

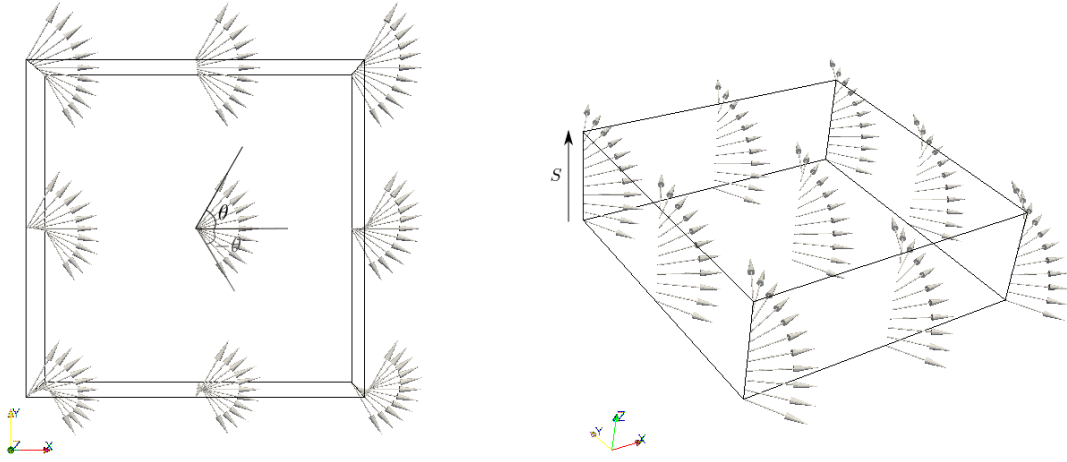


Figure 2.8: Parallelepipedal slab of ventricular tissue, with parameters  $\theta = 60^\circ$  and  $S = 1$  cm.

We need to transform (2.23) into cartesian coordinates to use it with the monodomain equation (2.22). We denote by  $\theta(z)$  the angle between the fibers and the  $y$ -axis in each plane. In this plane, the tensor (2.23) reduces to

$$D^\star = \begin{bmatrix} \sigma_l & 0 \\ 0 & \sigma_t \end{bmatrix}.$$

For a vector  $(x, y)$  in this plane, a rotation of angle  $-\theta(z)$  gives its coordinates along the fibers:

$$\begin{pmatrix} \cos \theta(z) & \sin \theta(z) \\ -\sin \theta(z) & \cos \theta(z) \end{pmatrix} \begin{pmatrix} x \\ y \end{pmatrix} = \begin{pmatrix} x \cos \theta(z) + y \sin \theta(z) \\ -x \sin \theta(z) + y \cos \theta(z) \end{pmatrix}.$$

We need to apply a rotation of angle  $\theta(z)$  to the local frame to have the corresponding components in cartesian coordinates

$$\begin{pmatrix} \cos \theta(z) & -\sin \theta(z) \\ \sin \theta(z) & \cos \theta(z) \end{pmatrix} \begin{pmatrix} a_l & 0 \\ 0 & a_t \end{pmatrix} = \begin{pmatrix} a_l \cos \theta(z) & -a_t \sin \theta(z) \\ a_l \sin \theta(z) & a_t \cos \theta(z) \end{pmatrix}$$

and we get the  $x$  and  $y$  components of the tensor in cartesian coordinates by multiplication of the two previous results

$$\begin{pmatrix} a_l \cos \theta(z) & -a_t \sin \theta(z) \\ a_l \sin \theta(z) & a_t \cos \theta(z) \end{pmatrix} \begin{pmatrix} x \cos \theta(z) + y \sin \theta(z) \\ -x \sin \theta(z) + y \cos \theta(z) \end{pmatrix} = \begin{pmatrix} (a_l \cos^2 \theta(z) + a_t \sin^2 \theta(z)) x + (a_l - a_t) \sin \theta(z) \cos \theta(z) y \\ (a_l \sin^2 \theta(z) + a_t \cos^2 \theta(z)) y + (a_l - a_t) \sin \theta(z) \cos \theta(z) x \end{pmatrix}.$$

Finally, we can write the tensor of conductivities in cartesian coordinates as

$$D = \begin{pmatrix} D_{11} & D_{12} & 0 \\ D_{21} & D_{22} & 0 \\ 0 & 0 & D_{\perp} \end{pmatrix},$$

where the components are given by

$$\begin{aligned} D_{11} &= \sigma_l \cos^2 \theta(z) + \sigma_t \sin^2 \theta(z), \\ D_{22} &= \sigma_l \sin^2 \theta(z) + \sigma_t \cos^2 \theta(z), \\ D_{12} &= D_{21} = (\sigma_l - \sigma_t) \sin \theta(z) \cos \theta(z), \\ D_{\perp} &= \sigma_n. \end{aligned}$$

There are essentially two kinds of anisotropy:

1. *axially symmetric anisotropy*: the diffusion in all directions perpendicular to the fibers is assumed to be the same, i.e.  $\sigma_t = \sigma_n$ .
2. *orthotropic anisotropy*: the diffusion is specific to each direction, in general  $\sigma_l \neq \sigma_t \neq \sigma_n$ .

For the next simulations, we assume valid the first definition of anisotropy.

**Remark 2.5** (Monodomain model for the general anisotropic case)

It is possible to get the monodomain model even if the hypothesis (2.21) is not fulfilled. We use the expression for the total current  $J_{tot} = -D_i \nabla \phi_i - D_e \nabla \phi_e$  and setting  $\phi_i = \phi + \phi_e$ , we get

$$\nabla \phi_e = -D^{-1} D_i \nabla \phi - D^{-1} J_{tot},$$

with  $D = D_i + D_e$ . Therefore, we have

$$\nabla \cdot (D_i \nabla \phi_e) = \nabla \cdot (-D_i D^{-1} D_i \nabla \phi - D_i D^{-1} J_{tot}),$$

where  $J_{tot}$  is related to  $\phi_e$  and  $\phi_i$ . Hence we want to approximate this current in terms of  $\phi$  only. We use the decomposition of the conductivity tensor in the local coordinates  $\{a_l, a_t, a_n\}$ . The key of this approximation is to neglect the projections of  $J_{tot}$  along the directions perpendiculars to the fibers. This is allowed because the current is mainly colinear to the fibers. We also use that  $\nabla \cdot J_{tot} = -I_{app}$ .

This method is explained in detail in [21, Section 2.3].

In view of this remark, we will use the monodomain equations for all simulations presented in this project.

## 2.4 Ionic models

To solve the monodomain problem (2.22) we need to specify the ionic current  $I_{ion}$ . We discuss now some of these ionic models. Those are mainly of two categories: physiologically based, which reproduce the microscopic dynamic of the cell, or phenomenologically based, which reproduce the macroscopic shape of the action potential.

### 2.4.1 Physiological models

The physiological models aim to reproduce the microscopic behavior of the cell. They are constructed using the Hodgking-Huxley formalism [27] characterizing the description of the ionic currents and ionic concentrations for cardiac cells.

**Beeler-Reuter (BR)** The model of Beeler and Reuter [10] is the first model for mammalian ventricular muscle cells and includes two inward currents and two outward currents. It was discovered that the intracellular calcium concentration changes significantly during the course of an action potential and therefore this is included in the model as an additional kinetic variable. The quantities involved in this model are summarized in Figure 2.9 (Left).

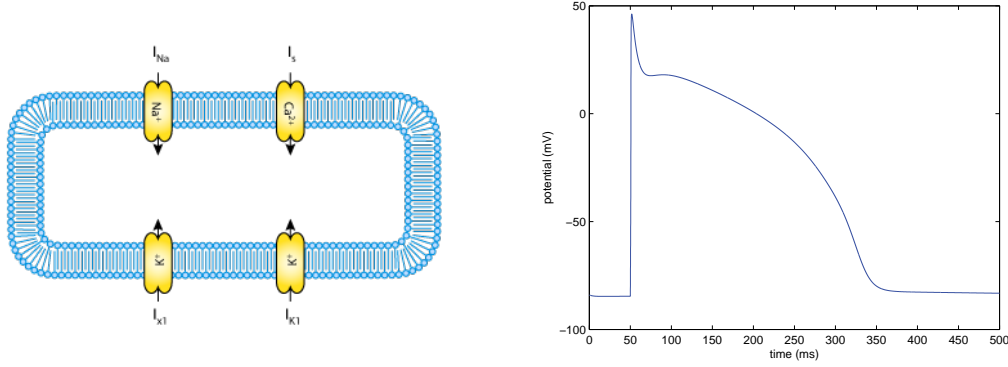


Figure 2.9: Left: A schematic diagram describing the current flows across the cell membrane that are captured in the BR model [1]. Right: Action potential for the Beeler-Reuter model.

The total ionic current flowing across the membrane is given by

$$I_{ion} = I_{Na} + I_{K1} + I_{x1} + I_s.$$

The fast inward sodium current  $I_{Na}$  is responsible for the fast upstroke of the action potential while the slow inward current  $I_s$  is responsible for the duration of the plateau phase. The time-independent outward potassium current  $I_{K1}$  and the time-dependent outward current  $I_{x1}$  are responsible for the repolarization of the cell [42]. The complete description of the model and the parameters are given in [10].

The typical shape of the action potential shown in Figure 2.9 (Right) is obtained by giving a stimulus of 80 mV during 1 ms. The integration of the cell model uses a timestep  $\Delta t = 0.02$  ms.

**Luo-Rudy (LR1)** The model proposed by Luo and Rudy [32] is a model for cardiac ventricular myocytes of guinea pigs and is based on the BR model. This model includes six ionic currents flowing through six different ionic channels. It takes also into account the evolution of the calcium concentration inside the cell. All these quantities are shown in Figure 2.10.



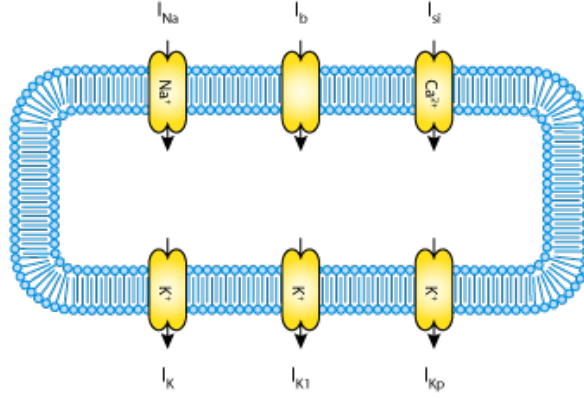


Figure 2.10: A schematic diagram describing the current flows across the cell membrane that are captured in the LR1 model [1].

The model is described by a system of nine differential equations:

$$\begin{aligned} -C_m \frac{d\phi}{dt} &= I_{ion} + I_{app}, \\ \frac{d[Ca]_i}{dt} &= -0.0001 I_{Ca} + 0.07(0.0001 - [Ca]_i), \\ \frac{dg}{dt} &= \alpha_g(1 - g) - \beta_g g, \end{aligned}$$

where  $g = m, h, j, d, f, X, X_i$  are the gating variables and

$$I_{ion} = I_{Na} + I_K + I_{K1} + I_{Kp} + I_{Ca} + I_b.$$

The parameters for this model are given in [32].

**Fox** Most of the ionic model of cardiac myocytes developed previously fails to reproduce alternans of cardiac action potential duration, while this phenomenon is a robust feature of the rapid paced canine ventricles. Alternans is a common heart rhythm disorder and will be discussed in details in Section 5. The ionic basis for alternans are determined using existing ionic computer model and used to create this new model.

The Fox model [20] is based on the LR1 model with the modification of Winslow et al. [52] which uses data for ionic currents obtained from canine ventricular myocytes. The new model uses also the alternative formulation for calcium dynamics proposed by Chudin et al. [14] in their modification of the LR1 model. Each of these previous models has limitations with respect to the study of ionic basis for electrical alternans and not reproduces sustained alternans at rapid pacing states. In this perspective, the objective of this model is to get an ionic model of cardiac ventricular myocytes that exhibits stable electrical alternans which can be used to identify the ionic currents responsible for alternans.

This model includes the formulation of 13 ionic currents and 10 gating variables. It takes also into account the calcium concentrations in the intracellular space  $[Ca^{2+}]_i$  and in the sarcoplasmic reticulum  $[Ca^{2+}]_{SR}$ . A schematic diagram of the involved ionic currents and calcium concentrations is shown in Figure 2.11.

The total ionic current is given by

$$I_{ion} = I_{Na} + I_K + I_p + I_{Ca} + I_{CaK},$$

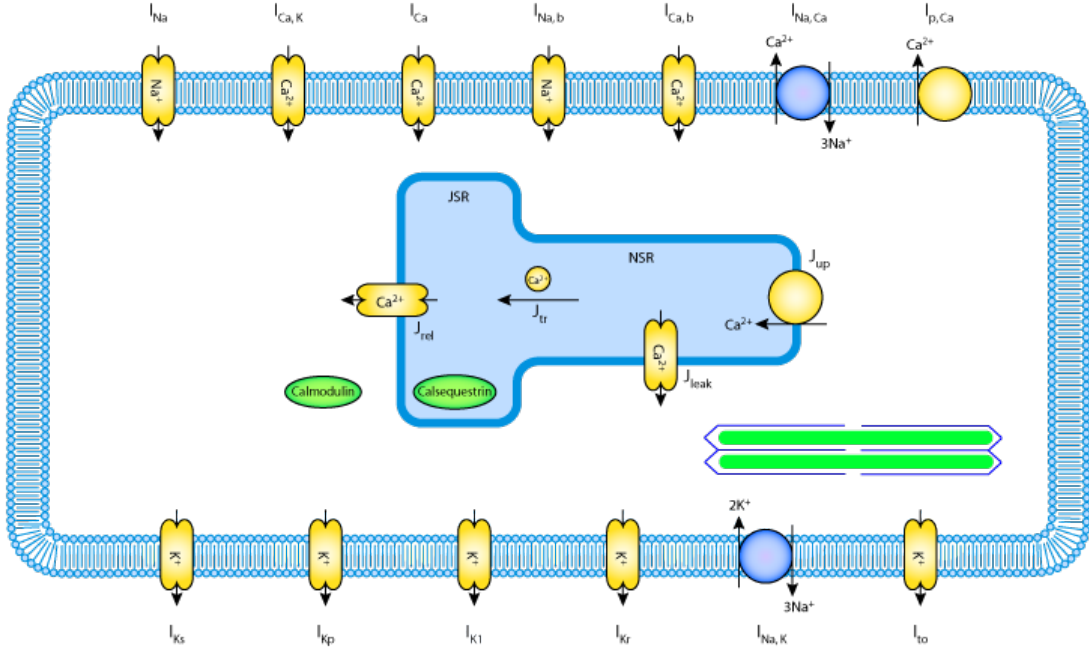


Figure 2.11: A schematic diagram describing the current flows across the cell membrane and the calcium fluxes between the cytoplasm and the sarcoplasmic reticulum that are captured in the Fox canine ventricular cell model [1].

where each current is defined in the following way:

- The rapid depolarization current  $I_{Na}$  is the current associated to the ion  $Na^+$ ;
- The current  $I_K = I_{K1} + I_{Kr} + I_{Ks} + I_{t0} + I_{Kp}$  is associated to the ion  $K^+$  and includes the following currents:
  - $I_{K1}$ , the inward rectifier  $K^+$  current, modified to get a smaller outward current at depolarization time;
  - $I_{Kr}$ , the rapid component of the delayed rectifier  $K^+$  current, altered to increase rectification, slow kinetics at depolarized potentials, and increase maximum conductance;
  - $I_{Ks}$ , the slow component of the delayed rectifier  $K^+$  current, altered to increase the magnitude of the current and shift the activation to less positive voltages;
  - $I_{t0}$ , the transient outward  $K^+$  current;
  - $I_{Kp}$ , the plateau  $K^+$  current.
- The current  $I_p = I_{NaCa} + I_{pCa} + I_{Cab} + I_{Nab}$  results from the pumps and exchangers, where:
  - $I_{NaCa}$  is the  $Na^+/Ca^{2+}$  exchange current;
  - $I_{pCa}$  is the sarcolemmal pump current;
  - $I_{Cab}$  is the  $Ca^{2+}$  background current;

- $I_{Nab}$  is the  $\text{Na}^+$  background current.
- The current  $I_{Ca}$  is the L-type  $\text{Ca}^{2+}$  channel current and is modified to get a time-dependent, enhanced  $\text{Ca}^{2+}$ -induced inactivation, as well as a decrease in the current magnitude. These changes give a smaller more rapidly inactivating  $\text{Ca}^{2+}$  current.
- The current  $I_{CaK}$  is the  $\text{K}^+$  current through the L-type  $\text{Ca}^{2+}$  channel.

These currents are associated to the gating variables according to Table 2.1.

Current	$I_{Na}$	$I_{t0}$	$I_{Kr}$	$I_{Ks}$	$I_{Ca}$
Gating variable	$m, h, j$	$X_{t0}, Y_{t0}$	$X_{Kr}$	$X_{Ks}$	$d, f, f_{Ca}$

Table 2.1: Ionic currents and associated gating variables.

The typical shape of the action potential shown in Figure 2.12 is obtained by giving a stimulus of 80 mV during 1 ms. The integration of the cell model uses a timestep  $\Delta t = 0.0025$  ms.

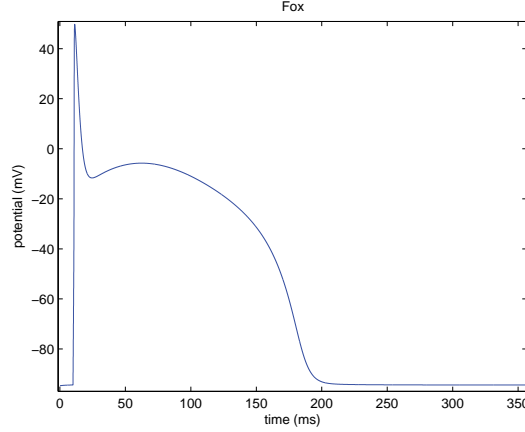


Figure 2.12: Action potential given by the Fox model.

### 2.4.2 Phenomenological models

We will now discuss two phenomenological models. These are based on the following description of the ionic current:

$$I_{ion} = f(v) = A^2(v - v_r)(v - v_t)(v - v_p), \quad (2.24)$$

where  $v_r$  is the resting potential,  $v_t$  the threshold potential and  $v_p$  the maximal potential. This model can reproduce only the very general shape of the action potential, but it fails in the description of the repolarization phase of the cells.

The great advantage of phenomenological models is the small number of variables. Some of these models reproduce very well the actual shape of the action with a very limited number of variables and parameters. This is very useful to reduce the computational cost.

**FitzHugh-Nagumo** In order to get a qualitatively correct description of the repolarization phase, we add to the simple model (2.24) a repolarization variable  $w$ . The FitzHugh-Nagumo's

model [19] [37] is given by the nondimensional differential system

$$\begin{aligned}\frac{dv}{dt} &= c_1 v(v - a)(1 - v) - c_2 w + I_{app}, \\ \frac{dw}{dt} &= b(v - c_3 w),\end{aligned}\tag{2.25}$$

where  $a, b, c_1, c_2, c_3$  are given parameters, see Table 2.2. The stimulus  $I_{app}$  is applied between  $t = 50$  and  $t = 60$  ms and its amplitude is 0.05. The shape of the transmembrane potential  $v$  and the gating variable  $w$  is shown in Figure 2.13. This model gives a simplification of the Hodgkin-Huxley model of spike generation in squid giant axons [27]. The biggest advantage of

$a$	$b$	$c_1$	$c_2$	$c_3$
0.13	0.013	0.26	0.1	1.0

Table 2.2: Parameters for the FitzHugh-Nagumo and Rogers-McCulloch models.

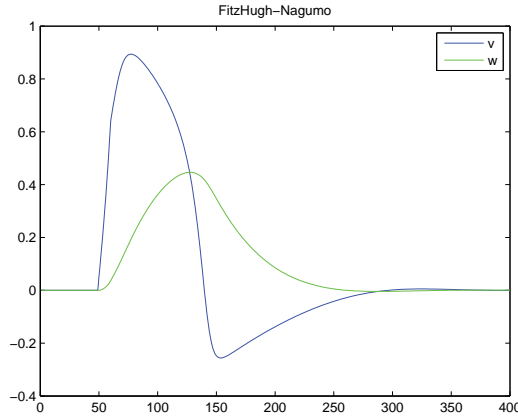


Figure 2.13: Action potential for the FitzHugh-Nagumo model (2.25).

such a model is its simplicity. However this model can't reproduce very well the physiological behavior of the cardiac cell. This model leads to an hyperpolarization during the repolarization phase which is physically unrealistic. The next model will correct this point.

**Rogers-McCulloch** The modification of Rogers and McCulloch [45] takes place only in the last term of the first equation of the system (2.25) and can avoid the hyperpolarization mentioned before.

$$\begin{aligned}\frac{dv}{dt} &= c_1 v(v - a)(1 - v) - c_2 vw + i_{app}, \\ \frac{dw}{dt} &= b(v - c_3 w),\end{aligned}\tag{2.26}$$

where  $a, b, c_1, c_2, c_3$  are given parameters, see Table 2.2. The potential is now qualitatively correct from a physiological point of view but the values are in a wrong scale. To get the coherent values, we have to rescale the variables  $v$  and  $w$  according to the following rescaling:

$$\begin{aligned}V &= v_{amp}v + v_r, \\ W &= v_{amp}w, \\ I_{app} &= v_{amp}i_{app}, \\ v_t &= v_r + av_{amp},\end{aligned}$$

where  $v_{amp} = v_p - v_r$ . The values of  $v_r$ ,  $v_t$  et  $v_p$  are reported in Table 2.3. The action potential resulting from this model is shown in Figure 2.14. We have to be careful that the gating variable is still adimensional.

$v_r$	$v_t$	$v_p$
-85	-68.75	40

Table 2.3: Parameters for the Rogers-McCulloch model.

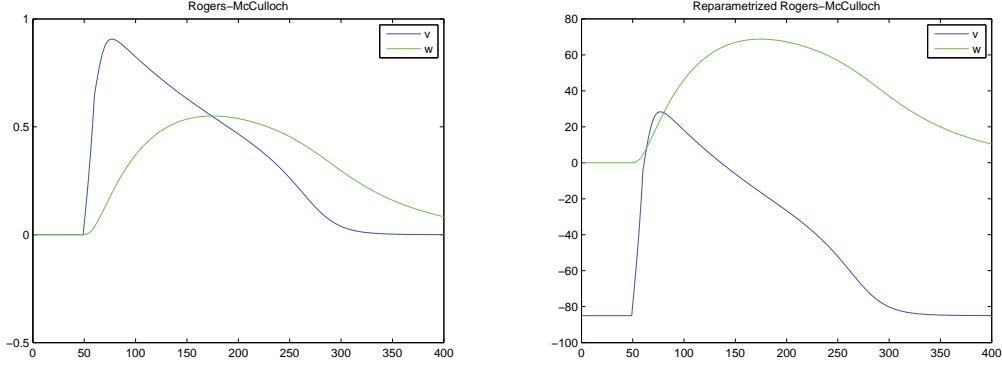


Figure 2.14: Action potential for the Rogers-McCulloch model before (left) and after (right) rescaling.

**Minimal model** The purpose of this model is to describe in the best possible way the electrophysiological properties of the human ventricle action potential with the two following constraints: first, the model has to reproduce the experimental data and secondly, we want that the model is computationally efficient.

The minimal model can reproduce the resting potential, the excitation threshold, the shape and the duration of the action potential. It was built by fitting a generic model on experimental data. In this way, we get the following four variables model:

$$\begin{aligned}
\frac{\partial u}{\partial t} &= \nabla \cdot (M \nabla u) - (I_{fi} + I_{so} + I_{si}), \\
\frac{\partial v}{\partial t} &= (1 - H(u - \theta_v))(v_\infty - v)/\tau_v^- - H(u - \theta_v)v/\tau_v^+, \\
\frac{\partial w}{\partial t} &= (1 - H(u - \theta_w))(w_\infty - w)/\tau_w^- - H(u - \theta_w)w/\tau_w^+, \\
\frac{\partial s}{\partial t} &= ((1 + \tanh(\kappa_s(u - u_s)))/2 - s)/\tau_s,
\end{aligned}$$

where  $u$  is the transmembrane potential and  $v, w, s$  are the gating variables. The function  $H(x)$  is the Heaviside function. The different ionic currents, the time-independent functions and the parameters are given in [12]. We depict the action potential in Figure 2.15.

### Remark 2.6

Since the previous models are species specific, they will give different results in terms of restitution of the physiological properties (electrical restitution, conduction velocity, ...).

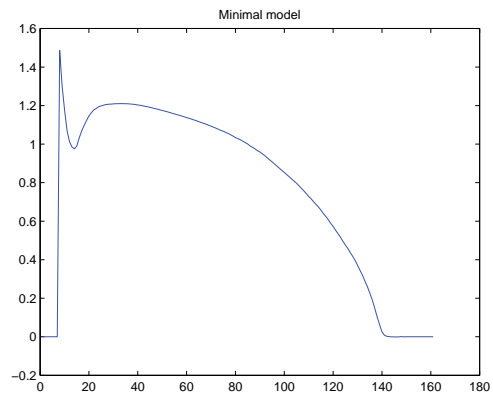


Figure 2.15: Action potential reproduced by the minimal model for the endocardium.

### 3 Numerical methods and discretization of the monodomain equations

In this section we will present the different numerical schemes used to solve the monodomain equations. We remind that the monodomain model is given by

$$\chi \left( C_m \frac{\partial \phi}{\partial t} + I_{ion}(\mathbf{u}, \phi) \right) - \nabla \cdot (D \nabla \phi) = I_{stim}, \quad (3.1)$$

$$\frac{\partial \mathbf{u}}{\partial t} = f(\mathbf{u}, \phi), \quad (3.2)$$

where  $\mathbf{u}$  is a set of cell-level gating and concentration variables and system (3.2) stands for the updating of those quantities.

#### 3.1 Finite difference approximation of the 1d and 2d cases

First we derive the finite difference approximation of the monodomain equations for the 1d case. We want to solve the system (3.1)-(3.2) in the cable  $\Omega = [x_0, x_F]$  for  $t \in [t_0, t_F]$ . In this specific case, the system reduces to

$$\begin{aligned} \chi \left( C_m \frac{\partial \phi}{\partial t} + I_{ion}(\mathbf{u}, \phi) \right) - \sigma \frac{\partial^2 \phi}{\partial x^2} &= I_{stim}, & \text{in } [x_0, x_F] \times [t_0, t_F] \\ \frac{\partial \mathbf{u}}{\partial t} &= f(\mathbf{u}, \phi), & \text{in } [x_0, x_F] \times [t_0, t_F], \end{aligned}$$

with the initial boundary conditions  $\phi(x, t_0) = \phi_0$ ,  $\mathbf{u}(x, t_0) = \mathbf{u}_0$  and the boundary conditions

$$\frac{\partial \phi}{\partial t}(x_0, t) = \frac{\partial \phi}{\partial t}(x_F, t) = 0, \quad \forall t \in [t_0, t_F].$$

The vector  $\mathbf{u}$  includes all the gating and concentration variables and the function  $f$  represents the evolution of these variables. We notice that in this case the conductivity tensor  $D$  reduces to the scalar  $\sigma$ .

##### 3.1.1 Discretization for the 1d case

The discretization of this system takes place in two times: first the time discretization and then the space discretization.

**Semi discretization in time** We consider a time interval  $T = [t_0, t_F]$  and we divide this interval into  $N_t$  subintervals of length  $\Delta t = \frac{t_F - t_0}{N_t}$ . The  $n$ -th timestep is given by  $t^n = n\Delta t$ , where  $\Delta t = t^{n+1} - t^n$ . We use a forward Euler scheme which gives us a first order approximation of the time derivatives:

$$\frac{\partial \phi}{\partial t} \sim \frac{\phi^{n+1} - \phi^n}{\Delta t}, \quad \frac{\partial \mathbf{u}}{\partial t} \sim \frac{\mathbf{u}^{n+1} - \mathbf{u}^n}{\Delta t},$$

where  $\phi^n = \phi(t^n)$  and  $\mathbf{u}^n = \mathbf{u}(t^n)$ . Since we solve first the cell model,

$$\frac{\mathbf{u}^{n+1} - \mathbf{u}^n}{\Delta t} = f(\mathbf{u}^n, \phi^n),$$

we get  $\mathbf{u}^{n+1}$  and then we obtain an explicit formulation of the time discretization of (3.1):

$$\chi \left( C_m \frac{\phi^{n+1} - \phi^n}{\Delta t} + I_{ion}(\mathbf{u}^{n+1}, \phi^n) \right) - \sigma \frac{\partial^2 \phi^n}{\partial x^2} = I_{stim}. \quad (3.3)$$

**Semi discretization in space** We divide the domain  $\Omega = [x_0, x_F]$  into  $N_h$  small intervals of equal length  $\Delta x = \frac{x_F - x_0}{N_h}$ . The  $i$ -th point of the cable is given by  $x_i = i\Delta x$ . We use a second order approximation of the space derivative:

$$\frac{\partial^2 \phi}{\partial x^2} \sim \frac{\phi_{i+1} - 2\phi_i + \phi_{i-1}}{\Delta x^2}, \quad (3.4)$$

where  $\phi_i = \phi(x_i)$ .

**Full discretization** Combining the discretizations (3.3) and (3.4), we get the full discretization of the monodomain problem. To solve numerically this problem we proceed through the following steps:

1. We start from the initial values of the transmembrane potential, the gating variables and the concentrations.
2. We iterate the following steps until we reach the final time  $t_F$ :
  - (a) Knowing the value of the transmembrane potential and the other variables at the previous time step, we solve the cell model:

$$\mathbf{u}_i^{n+1} = \mathbf{u}_i^n + \Delta t f(\mathbf{u}_i^n, \phi_i^n), \quad \forall 1 \leq i \leq N_h.$$

- (b) Knowing  $\mathbf{u}_i^{n+1}$ , we get the transmembrane potential in the internal nodes:

$$\phi_i^{n+1} = \frac{\Delta t}{\chi C_m} \left( I_{stim} + \sigma \frac{\phi_{i+1}^n - 2\phi_i^n + \phi_{i-1}^n}{\Delta x^2} \right) - \frac{\Delta t}{C_m} I_{ion}(\mathbf{u}_i^{n+1}, \phi_i^n), \quad \forall 2 \leq i \leq N_h - 2.$$

On the boundaries we have:

$$\begin{aligned} \phi_1^{n+1} &= \frac{\Delta t}{\chi C_m} \left( I_{stim} + \sigma \frac{2\phi_2^n - 2\phi_1^n}{\Delta x^2} \right) - \frac{\Delta t}{C_m} I_{ion}(\mathbf{u}_1^{n+1}, \phi_1^n), \\ \phi_{N_h}^{n+1} &= \frac{\Delta t}{\chi C_m} \left( I_{stim} + \sigma \frac{2\phi_{N_h-1}^n - 2\phi_{N_h}^n}{\Delta x^2} \right) - \frac{\Delta t}{C_m} I_{ion}(\mathbf{u}_{N_h}^{n+1}, \phi_{N_h}^n). \end{aligned}$$

### 3.1.2 Generalization to the 2d case

We can generalize the method previously described to the approximation of the monodomain equations on a square domain  $\Omega = [x_0, x_F]^2$ . The time discretization is exactly the same as the one for the 1d case 3.1.1. In this case the conductivity coefficient is no more a scalar, but a tensor, and we denote it by  $D = \begin{pmatrix} D_{11} & D_{12} \\ D_{12} & D_{22} \end{pmatrix}$ . We consider only homogeneous media. So the conductivity is independent of the position and the diffusive part of (3.1) becomes

$$\begin{aligned} \nabla \cdot (D \nabla \phi) &= \begin{pmatrix} \partial/\partial x \\ \partial/\partial y \end{pmatrix} \cdot \left( \begin{pmatrix} D_{11} & D_{12} \\ D_{12} & D_{22} \end{pmatrix} \begin{pmatrix} \partial\phi/\partial x \\ \partial\phi/\partial y \end{pmatrix} \right) \\ &= \begin{pmatrix} \partial/\partial x \\ \partial/\partial y \end{pmatrix} \cdot \begin{pmatrix} D_{11}\partial\phi/\partial x + D_{12}\partial\phi/\partial y \\ D_{12}\partial\phi/\partial x + D_{22}\partial\phi/\partial y \end{pmatrix} \\ &= D_{11} \frac{\partial^2 \phi}{\partial x^2} + 2D_{12} \frac{\partial^2 \phi}{\partial x \partial y} + D_{22} \frac{\partial^2 \phi}{\partial y^2}. \end{aligned}$$



**Isotropic case** In the isotropic case, the conductivity tensor has the diagonal form

$$D = \begin{pmatrix} \sigma & 0 \\ 0 & \sigma \end{pmatrix}$$

and therefore

$$\nabla \cdot (D \nabla \phi) = \sigma \Delta \phi. \quad (3.5)$$

Hence we approximate the Laplacian using the following discretization:

$$\Delta \phi(x_i, x_j) \sim \frac{\phi_{i-1,j} + \phi_{i+1,j} + \phi_{i,j-1} + \phi_{i,j+1} - 4\phi_{i,j}}{\Delta x^2}, \quad 2 \leq i \leq N_h - 1, 2 \leq j \leq N_h - 1$$

with the following values on the boundaries:

$$\begin{aligned} \Delta \phi(x_1, x_j) &\sim \frac{-4\phi_{1,j} - 2\phi_{2,j} - \phi_{1,j-1} - \phi_{1,j+1}}{\Delta x^2} \\ \Delta \phi(x_{N_h}, x_j) &\sim \frac{-4\phi_{N_h,j} - 2\phi_{N_h-1,j} - \phi_{N_h,j-1} - \phi_{N_h,j+1}}{\Delta x^2} \\ \Delta \phi(x_i, x_1) &\sim \frac{-4\phi_{i,1} - 2\phi_{i,2} - \phi_{i-1,1} - \phi_{i+1,1}}{\Delta x^2} \\ \Delta \phi(x_i, x_{N_h}) &\sim \frac{-4\phi_{i,N_h} - 2\phi_{i,N_h-1} - \phi_{i-1,N_h} - \phi_{i+1,N_h}}{\Delta x^2} \end{aligned}$$

and in the corners:

$$\begin{aligned} \Delta \phi(x_1, x_1) &\sim \frac{-4\phi_{1,1} - 2\phi_{2,1} - 2\phi_{1,2}}{\Delta x^2} \\ \Delta \phi(x_1, x_{N_h}) &\sim \frac{-4\phi_{1,N_h} - 2\phi_{2,N_h} - 2\phi_{1,N_h-1}}{\Delta x^2} \\ \Delta \phi(x_{N_h}, x_1) &\sim \frac{-4\phi_{N_h,1} - 2\phi_{N_h-1,1} - 2\phi_{N_h,2}}{\Delta x^2} \\ \Delta \phi(x_{N_h}, x_{N_h}) &\sim \frac{-4\phi_{N_h,N_h} - 2\phi_{N_h-1,N_h} - 2\phi_{N_h,N_h-1}}{\Delta x^2}. \end{aligned}$$

**Anisotropic case** In the anisotropic case, the relation (3.5) is not valid and hence we can't use the previous the discretization. We derive the finite difference approximation of the diffusive part of (3.1) following the method of [47]. We define the coefficients

$$\begin{aligned} A_{1,3} &= \frac{D_{11}}{\Delta x^2} & A_{2,4} &= \frac{D_{22}}{\Delta x^2} \\ A_{5,7} &= \frac{D_{12}}{2\Delta x^2} & A_{6,8} &= \frac{-D_{12}}{2\Delta x^2} \end{aligned} \quad (3.6)$$

associated to the finite difference grid presented in Figure 3.1. The discrete approximation of the Laplacian at  $\mathbf{x}_0$  is given by

$$\Delta \phi(\mathbf{x}_0) \sim \sum_{i=1}^8 A_i \phi(\mathbf{x}_i) - \left( \sum_{i=1}^8 A_i \right) \phi(\mathbf{x}_0).$$

We follow the same steps of resolution as in 3.1.1 to get the approximation of the monodomain equation in the 2d case.

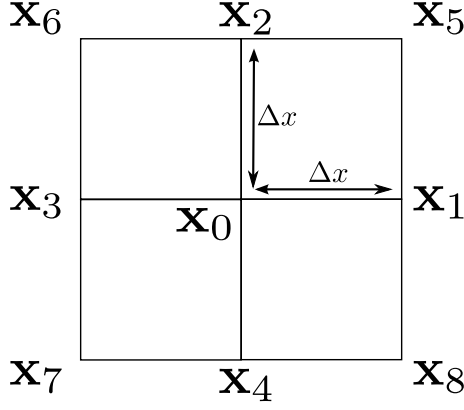


Figure 3.1: Finite difference grid used to derive the discretization of the diffusive term of (3.1) in the anisotropic case.

### 3.2 Finite element methods for the tridimensional simulations

For the tridimensional simulations, the numerical approximation of the solution is carried out using the finite element method. We use this method instead of the finite difference method because it is well suited to handle derivative boundary conditions and irregular geometries, such as the heart, in a systematic and straightforward manner. For all the simulations presented in this project, we use a tetrahedral decomposition of the domain and the solution is given by a linear polynomial approximation of the solution on each element of the domain. We have seen that the cell model leads to the resolution of a system of ordinary differential equations. This system is solved using a standard solver such as forward Euler.

First we derive the finite element discretization of the monodomain equations and then we present three different ways to couple back the solution of the cell model to the solution of the full problem.

#### 3.2.1 Finite element discretization

The discretization can be divided into two parts: first the time discretization and then the space discretization. For clarity, in this section we set the external stimulus  $I_{stim}$  to zero. As before we denote by  $\phi^n$  the value of the transmembrane potential at time  $t^n$ . We use a semi-implicit discretization in time, in which the conduction term is treated implicitly and the nonlinear reaction term is treated explicitly. For the equation (3.1) this may be written as

$$\chi \left( C_m \frac{\phi^{n+1} - \phi^n}{\Delta t} + I_{ion}(\mathbf{u}^{n+1}, \phi^n) \right) - \nabla \cdot (\sigma \nabla \phi^{n+1}) = 0.$$

The time step  $\Delta t$  has to be small enough to not affect the precision of the approximation, constrained by a CFL condition associated to the semi-implicit scheme [43].

Then we derive the weak formulation of semi-discrete form of the equation (3.1). It is given by: find  $\phi^{n+1} \in H^1(\Omega)$ , such that

$$\int_{\Omega} \chi \left( C_m \frac{\phi^{n+1} - \phi^n}{\Delta t} + I_{ion}(\mathbf{u}^{n+1}, \phi^n) \right) \psi d\Omega + \int_{\Omega} \sigma \nabla \phi^{n+1} \cdot \nabla \psi d\Omega = 0, \quad \forall \psi \in H^1(\Omega). \quad (3.7)$$

It is possible to show existence and uniqueness of weak solutions to (3.7). Some other results about the regularity of these solutions can be found in [22].

We use a conform tetrahedral decomposition  $\mathcal{T}_h$  of the domain  $\Omega$  such that  $\Omega = \cup_{j=1}^N K_j$ , with  $K_j \in \mathcal{T}_h$  for  $1 \leq j \leq N$ . We follow here the Galerkin finite element method [43] to get the space discretization of the variational problem (3.7) and we use the finite element space  $X_h$  of degree one — $\mathbb{P}_1$ — of finite dimension  $N_h$ . The basis of this space is denoted by  $\{\psi_i\}_{i=1}^{N_h}$ . We build the mass matrix  $M = (m_{kl})$  and the stiffness matrix  $A = (a_{kl})$  whose elements are given by

$$m_{kl} = \sum_{j=1}^N \int_{K_j} \psi_k \psi_l d\Omega,$$

$$a_{kl} = \sum_{j=1}^N \int_{K_j} \sigma \nabla \psi_k \cdot \nabla \psi_l d\Omega$$

and we define  $\mathbf{b}^{n+1} = (b_1^{n+1}, \dots, b_{N_h}^{n+1})$  by

$$b_j^{n+1} = \int_{\Omega} \chi \left( \frac{C_m}{\Delta t} \phi^n - I_{ion}(\mathbf{u}^{n+1}, \phi^n) \right) \psi_j d\Omega.$$

Letting  $\Phi^{n+1} = (\phi_1^{n+1}, \dots, \phi_{N_h}^{n+1})$  be a vector of the nodal values of the transmembrane potential, we can write the matrix form of (3.7):

$$\left( \frac{\chi C_m}{\Delta t} M + A \right) \Phi^{n+1} = \mathbf{b}^{n+1}. \quad (3.8)$$

The ionic current  $I_{ion}$  is computed at each node using the chosen cell model. Since we know the value of the potential at each time step, it is possible to update the cell model at the beginning of each time step.

### 3.2.2 Interpolation of the ionic current

Each time step requires the integration of the cell model, we discuss now two ways of doing this. First, we suppose that we already know the value of the state variables and the value of the transmembrane potential at each node, that is  $\mathbf{u}_j$  and  $\phi_j$  for  $j = 1, \dots, N_h$ . Using these values we can compute the value of the ionic current at each node

$$I_j = I_{ion}(\mathbf{u}_j, \phi_j).$$

Now we want to use this value to build an approximation  $I(\mathbf{x})$  of the ionic current at each point of the domain,  $\mathbf{x} \in \Omega$ . There are mainly two ways for doing this [40]:

#### 1. Ionic current interpolation (ICI)

This method gives an interpolation of the ionic current using the finite element basis  $\{\psi_i\}_{i=1}^{N_h}$ . So, in this case,  $I(\mathbf{x})$  is given by

$$I_{ICI}(\mathbf{x}) = \sum_{j=1}^{N_h} I_j \psi_j(\mathbf{x}).$$

#### 2. State variables interpolation (SVI)

This approximation uses the interpolated values of the state variables and the transmembrane potential into the interior of the elements to compute the ionic current:

$$I_{SVI}(\mathbf{x}) = I_{ion} \left( \sum_{j=1}^{N_h} \mathbf{u}_j \psi_j(\mathbf{x}), \sum_{j=1}^{N_h} \phi_j \psi_j(\mathbf{x}) \right).$$

Since cell models are in general highly nonlinear these two methods give different approximations of the ionic current. If SVI gives certainly a more accurate approximation of the ionic current, there are several advantages to use the ICI approach in terms of computational efficiency. The most important one deals with the construction of the vector  $\mathbf{b}^{n+1}$ . In general it has to be computed by looping over all the elements, computing the integral for each of them and then assigning the value to the right components of the vector. When we solve the monodomain problem there are three tasks to be done at each time step: solving the ODE cell model, assembling the vector  $\mathbf{b}^{n+1}$  and solving the linear system (3.8). The assembly of the vector  $\mathbf{b}^{n+1}$  can dominate the computational burden. However, with the ICI method, this step can be done very cheaply. Indeed, since  $\phi^n = \sum_{j=1}^{N_h} \phi_j^n \psi_j$ , we obtain, using implicit summation convention, that

$$\begin{aligned} b_j^{n+1} &= \int_{\Omega} \chi \left( \frac{C_m}{\Delta t} \phi_k^n \psi_k - I_k^n \psi_k \right) d\Omega \\ &= \left( \chi \int_{\Omega} \psi_j \psi_k d\Omega \right) \left( \frac{C_m}{\Delta t} \phi_k^n - I_k^n \right) \\ &= \chi M \left( \frac{C_m}{\Delta t} \Phi^n - \mathbf{I}^n \right), \end{aligned} \quad (3.9)$$

where  $M$  is the mass matrix and can be computed once for all at the beginning of the algorithm. Here,  $\mathbf{I}^n$  is the vector of the nodal values of the ionic currents. Finally the construction of the vector  $\mathbf{b}^{n+1}$  reduces to a matrix-vector multiplication. This kind of construction is not possible when the SVI method is used. Another advantage of using the ICI method is related to parallelization. Indeed we have some tools to efficiently parallelize this kind of elementary operations. All these considerations are explained in more details in [40].

The formulation (3.9) leads to the resolution of the following linear systems:

$$\left( \frac{\chi C_m}{\Delta t} M + A \right) \Phi^{n+1} = \chi M \left( \frac{C_m}{\Delta t} \Phi^n - \mathbf{I}^n \right), \quad \text{for ICI} \quad (3.10)$$

$$\left( \frac{\chi C_m}{\Delta t} M + A \right) \Phi^{n+1} = \chi M \left( \frac{C_m}{\Delta t} \Phi^n - \mathbf{I}^n \right) + \mathbf{c}^n, \quad \text{for SVI}, \quad (3.11)$$

where the vector  $\mathbf{c}^n$  is defined by

$$c_j^n = \chi \int_{\mathcal{T}} (I_{ICI} - I_{SVI}) \psi_j d\mathcal{T}.$$

This vector is a correction term. Due to computational efficiency this correction is done only on a selection of elements  $\mathcal{T}$  on which the ionic current is not small for instance, on the wavefront, see [39].

### 3.2.3 Operator splitting

There is an alternative approach that is widely used to solve the monodomain equations which is the reaction-diffusion operator splitting. In this method, the partial differential equation (3.1) is broken down into two parts :

- The system of nodal ordinary differential equations associated to the cell model:

$$\begin{aligned} C_m \frac{d\phi}{dt} &= -I_{ion}(\mathbf{u}, \phi), \\ \frac{\partial \mathbf{u}}{\partial t} &= f(\mathbf{u}, \phi). \end{aligned} \quad (3.12)$$

- The partial differential equation related to the diffusive part:

$$\chi C_m \frac{\partial \phi}{\partial t} = \nabla \cdot (\sigma \nabla \phi). \quad (3.13)$$

These two equations are solved sequentially. Assuming that  $\phi^n$  and  $\mathbf{u}^n$  are known, one time step of the splitting method consists of the following three operations [49]:

1. Solve the ODE system:

$$\begin{aligned} C_m \frac{d\phi}{dt} &= -I_{ion}(\mathbf{u}, \phi), \\ \frac{\partial \mathbf{u}}{\partial t} &= f(\mathbf{u}, \phi), \end{aligned}$$

for  $t^n < t \leq t^n + \theta \Delta t$ , with initial conditions  $\phi(t^n) = \phi^n$  and  $\mathbf{u}(t^n) = \mathbf{u}^n$ . The resulting solutions  $\phi(t^n + \theta \Delta t)$  and  $\mathbf{u}(t^n + \theta \Delta t)$  are denoted by  $\phi_\theta^n$  and  $\mathbf{u}_\theta^n$ .

2. Solve the diffusive PDE:

$$\chi C_m \frac{\partial \phi}{\partial t} = \nabla \cdot (\sigma \nabla \phi),$$

for  $t^n < t \leq t^n + \Delta t$  with initial condition  $\phi(t^n) = \phi_\theta^n$ . The resulting solution  $\phi(t^n + \Delta t)$  is denoted by  $\phi_\theta^{n+1}$ .

3. Solve the ODE system:

$$\begin{aligned} C_m \frac{d\phi}{dt} &= -I_{ion}(\mathbf{u}, \phi), \\ \frac{\partial \mathbf{u}}{\partial t} &= f(\mathbf{u}, \phi), \end{aligned}$$

for  $t^n + \theta \Delta t < t \leq t^n + \Delta t$ , with initial conditions  $\phi(t^n + \theta \Delta t) = \phi_\theta^{n+1}$  and  $\mathbf{u}(t^n + \theta \Delta t) = \mathbf{u}_\theta^{n+1}$ . The resulting solutions  $\phi(t^n + \Delta t)$  and  $\mathbf{u}(t^n + \Delta t)$  are denoted by  $\phi^{n+1}$  and  $\mathbf{u}^{n+1}$ .

**First-order splitting** A first-order splitting correspond to a choice of  $\theta = 1$  and is typically associated with first-order time discretization methods. The simplest way to solve this problem is to use a forward Euler scheme for the resolution of the ODE system and a backward Euler scheme for the time discretization of the PDE.

### Remark 3.1

In this specific case, the operator splitting method is identical to the ICI. Indeed, for an intermediate variable  $\Phi^{n+\star}$ , we get the following linear system associated to the equations (3.12)-(3.13):

$$C_m \Phi^{n+\star} = C_m \Phi^n - \Delta t \mathbf{I}^n, \quad (3.14)$$

$$\left( \chi \frac{C_m}{\Delta t} M + A \right) \Phi^{n+1} = M \left( \chi \frac{C_m}{\Delta t} \Phi^{n+\star} \right) \quad (3.15)$$

and substituting (3.14) into (3.15)

$$\begin{aligned} \left( \chi \frac{C_m}{\Delta t} M + A \right) \Phi^{n+1} &= M \left( \chi \frac{C_m}{\Delta t} \left( \Phi^n - \frac{\Delta t}{C_m} \mathbf{I}^n \right) \right) \\ &= \chi M \left( \frac{C_m}{\Delta t} \Phi^n - \mathbf{I}^n \right), \end{aligned}$$

which is exactly the ICI formulation (3.10).

If a different splitting scheme is used the method will not be identical to ICI anymore, but the differences will be only in the time discretization part of the scheme.

**Second-order splitting** To improve the accuracy of the scheme it is possible to use a second order splitting method. This corresponds to the choice  $\theta = 1/2$  in the splitting method. In general we use in this case a higher-order accuracy scheme to solve the systems (3.12) and (3.13). Here we still use a forward Euler scheme for the time discretization of the ODE system but we use a second-order backward differentiation formula (BDF2) for the diffusion part, that is:

$$\chi C_m \frac{3\phi^{m+1} - 4\phi^m + \phi^{m-1}}{2\Delta t} = \nabla \cdot (\sigma \nabla \phi^{m+1}),$$

where  $\phi^{m-1} = \phi^n$ ,  $\phi^m = \phi_{1/2}^n$  and  $\phi^{m+1} = \phi^{n+1}$ . Hence, for some intermediate variables  $\Phi^{n+\star}$  and  $\Phi^{n+\star\star}$ , we get the following linear system associated to the equations (3.12)-(3.13):

$$\begin{cases} C_m \Phi^{n+\star} = C_m \Phi^n - \Delta t \mathbf{I}^n, \\ \left( \chi \frac{C_m}{\Delta t} 3M + 2A \right) \Phi^{n+\star\star} = \chi \frac{C_m}{\Delta t} M (4\Phi^{n+\star} - \Phi^n), \\ C_m \Phi^{n+1} = C_m \Phi^{n+\star\star} - \Delta t \mathbf{I}^{n+\star\star}. \end{cases} \quad (3.16)$$

In the further simulations the first-order and the second-order splitting methods are used depending on the complexity of the cell model chosen.

### 3.2.4 Mass lumping

The mass lumping technique involves replacing the mass matrix  $M$  by a diagonal matrix  $M_L$  defined by

$$(M_L)_{ij} = \begin{cases} \sum_k M_{ik} & \text{if } i = j, \\ 0 & \text{otherwise.} \end{cases}$$

This method is related with the usage of the trapezoidal rule for the computation of the integrals, for more detailed explanations see [43]. The choice of using the lumped mass matrix instead of the classical mass matrix is justified by the reduction of the computational cost.

## 4 Pseudo-ECG

The electrocardiogram (ECG) is the oldest and the most important tool to record and analyze the electrical activity of the heart. The first recording was done in 1877 and the ECG is still widely used by cardiologist. On this line, it is useful to construct the ECG signals related to the mathematical models we developed to reproduce the electrical activity of the heart.

An action potential of the heart generates an electrical field which can be measured on the body surface thus resulting in the ECG. Since the body is a volumetric conductor, when there is any current source somewhere in the body, currents spread throughout the body [28]. Even for a small voltage potential, the potential differences can be recorded between any two points of the body. The typical shape of an ECG signal is shown in Figure 4.1.

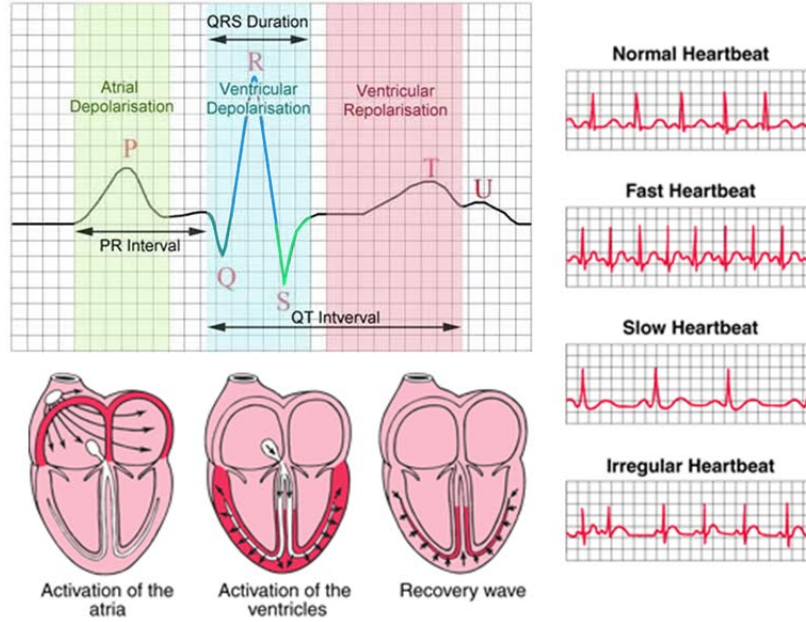


Figure 4.1: ECG trace with its associated vocabulary [4]. Each part of the ECG is related to a specific step of the action potential propagation.

Here we discuss a way to derive such a quantity from the transmembrane potential in the myocardium. We follow the approach of [41] and [15]. Then we explain how to get it numerically.

### 4.1 Definition and derivation

The ECG is a measure of change in the electric potential on the body surface and is the result of the current flowing inside the torso and the myocardium generated by an action potential. The Ohm's law gives that the current flow in the torso is given by:

$$\mathbf{J} = \mathbf{J}^s + \sigma \mathbf{E}, \quad (4.1)$$

where  $\sigma \mathbf{E}$  is the current generated by the source current and  $\mathbf{J}^s$  is an impressed density current, which is zero everywhere excepted in the myocardium. Since the membrane current is negligible and the electric field  $\mathbf{E}$  is quasi-static, i.e.  $\mathbf{E} = -\nabla \phi$ , the equation (4.1) becomes:

$$\mathbf{J} = \mathbf{J}^s - \sigma \nabla \Phi, \quad (4.2)$$

where  $\Phi$  is the electric potential. Taking the divergence of (4.2), we get

$$\nabla \cdot \mathbf{J} = \nabla \cdot \mathbf{J}^s - \nabla \cdot (\sigma \nabla \Phi). \quad (4.3)$$

Since the charge is conserved and there is no source nor sink of current over the entire torso, we have

$$\int_S \mathbf{J} \cdot \mathbf{n} dS = 0,$$

for any surface  $S$  embedded in the torso, with  $\mathbf{n}$  the unit outward normal vector to the surface. By the divergence theorem, this is equivalent to

$$\int_V \nabla \cdot \mathbf{J} dV = 0,$$

for any volume  $V$  embedded in the torso. Since this property is valid for any little volume of the body, we deduce that

$$0 = \nabla \cdot \mathbf{J} = \nabla \cdot \mathbf{J}^s - \nabla \cdot (\sigma \nabla \Phi)$$

and if the torso is considered as an isotropic medium with conductivity  $\sigma$ , we get  $\sigma \nabla^2 \Phi = \nabla \cdot \mathbf{J}^s$ .

Now we want to define the potential  $\Phi$  as a function of the position  $\mathbf{r}$  where the potential is recorded. First, we remind the Green's theorem

$$\int_V (A \nabla^2 B - B \nabla^2 A) dV = \int_S (A \nabla B - B \nabla A) \cdot \mathbf{n} dS. \quad (4.4)$$

Setting  $A$  to  $\Phi$  and  $B$  to  $\frac{1}{r}$  for  $r = \|\mathbf{r}\|$  in (4.4), we obtain

$$\int_V \left( \Phi \nabla^2 \left( \frac{1}{r} \right) - \frac{1}{r} \nabla^2 \Phi \right) dV = \int_S \left( \Phi \nabla \left( \frac{1}{r} \right) - \frac{1}{r} \nabla \Phi \right) \cdot \mathbf{n} dS. \quad (4.5)$$

For a point source, currents and potential are uniform in all directions, the extracellular potential is given by [41]:

$$\Phi_e = \frac{1}{4\pi\sigma_e} \cdot \frac{I_0}{r},$$

where  $I_0$  is the source amplitude. Using this result and choosing a right surface  $S$ , we get that  $\nabla^2 \left( \frac{1}{r} \right) = -4\pi$  at  $r = 0$  and 0 elsewhere [41]. Since  $\nabla \left( \frac{1}{r} \right) = \frac{\mathbf{r}}{r^3}$ , and  $\nabla^2 \Phi = \frac{1}{\sigma} \nabla \cdot \mathbf{J}^s$ , the equation (4.5) becomes

$$-4\pi\Phi - \int_V \frac{1}{r\sigma} \nabla \cdot \mathbf{J}^s dV = \int_S \Phi \frac{\mathbf{r}}{r^3} \cdot \mathbf{n} dS - \int_S \frac{1}{r} \nabla \Phi \cdot \mathbf{n} dS,$$

where  $\nabla \Phi \cdot \mathbf{n}$  is zero if we consider the torso as a homogeneous volume conductor [15]. Hence we get

$$\Phi(\mathbf{x}) = \frac{1}{4\pi\sigma} \int_V \frac{1}{r} \nabla \cdot \mathbf{J}^s dV + \frac{1}{4\pi} \int_S \Phi \frac{\mathbf{r}}{r^3} \cdot \mathbf{n} dS, \quad (4.6)$$

where  $\mathbf{x}$  is the observation point and  $\mathbf{r}$  becomes the vector between each elementary elements and  $\mathbf{x}$ . Here we assume the bounding surface is too far away to have any effect on the result and so we neglect the last term of (4.6). Thus we obtain

$$\Phi(\mathbf{x}) = \frac{1}{4\pi\sigma} \int_V \frac{1}{r} \nabla \cdot \mathbf{J}^s dV. \quad (4.7)$$

As previously mentioned, we suppose that the torso has an isotropic conductivity  $\sigma_h$  and we approximate the impressed density current by  $\mathbf{J}^s = \sigma_h \cdot \nabla V_m$ , where  $V_m$  is the transmembrane potential related to a chosen cell model. Finally, since we are only interested in the shape of the function (4.7), we use the following formulation: for a transmembrane potential  $V_m(\mathbf{x}, t)$ ,  $\mathbf{x} \in \Omega$ , the *pseudo-ECG* associated to an electrode  $e$  is given by

$$ECG(\mathbf{x}_e) = \int_{\Omega} \Delta V_m(\mathbf{x}, t) \cdot \frac{1}{r_e} d\Omega, \quad (4.8)$$

where  $r_e = \|\mathbf{x} - \mathbf{x}_e\|$  and  $\mathbf{x}_e$  is the position of the electrode  $e$  [7].



## 4.2 Approximation and computation

For the 1d and the 2d cases the approximation of  $\Delta V_m(\mathbf{x}, t)$  is computed using the discrete form of the Laplacian. This discretization is the same as that used for the finite difference approximation of the monodomain equation 3.1.1. It can be computed directly at each time step of the algorithm.

In the 3d case the computation of the pseudo-ECG is not so straightforward. We need to split the computation of the pseudo-ECG,  $ECG(\mathbf{x}_e)$  into two steps. First we find the finite element approximation of  $\Delta V_m(\mathbf{x}, t)$  and after that we can compute the integral.

### 4.2.1 Finite element approximation of $\Delta V_m(\mathbf{x}, t)$

In our case we deal with the finite element approximation of the transmembrane potential  $V_m(\mathbf{x}, t)$  and we denote it by  $V_{m_h}$ . If  $\Omega = \text{int}(\cup_{K \in \mathcal{T}_h} K)$  where  $\mathcal{T}_h$  is an admissible decomposition in tetrahedral elements of the domain  $\Omega$ , the solution is a member of the finite element space

$$V_h = \left\{ v_h \in C^0(\bar{\Omega}) : v_h|_K \in \mathbb{P}_n, \forall K \in \mathcal{T}_h \right\}, \quad n \in \mathbb{N}.$$

This space is finite dimensional and its Lagrangian basis is given by  $\{\varphi_i\}_{i=1}^{N_h}$ , where  $N_h$  is the dimension of  $V_h$ .

Now our problem is to compute the quantity  $\Delta V_{m_h}$  in the finite element space  $V_h$ . This is equivalent to looking for  $f \in V_h$  such that

$$\Delta V_{m_h} = f.$$

Given a test function  $v \in V_h$ , we are looking for  $f \in V_h$  such that

$$\int_{\Omega} \Delta V_{m_h} v d\Omega = \int_{\Omega} f v d\Omega, \quad \forall v \in V_h.$$

By the Green's theorem, we have

$$\int_{\Omega} \Delta V_{m_h} v d\Omega = \int_{\partial\Omega} v \left( \frac{\partial V_{m_h}}{\partial \mathbf{n}} \right) d\Gamma - \int_{\Omega} \nabla V_m(\mathbf{x}, t) \cdot \nabla v d\Omega$$

and, as we have a zero-flux condition on the boundary of the domain, the problem reduces to: find  $f \in V_h$  such that

$$- \int_{\Omega} \nabla V_{m_h} \cdot \nabla v d\Omega = \int_{\Omega} f v d\Omega, \quad \forall v \in V_h. \quad (4.9)$$

As the functions  $V_{m_h}$  and  $f$  are members of the finite element space  $V_h$ , we can decompose them in the basis  $\{\varphi_i\}_{i=1}^{N_h}$  as

$$V_{m_h} = \sum_{i=1}^{N_h} v_i \varphi_i \quad \text{and} \quad f = \sum_{i=1}^{N_h} f_i \varphi_i.$$

As the equation (4.9) is valid for all  $v \in V_h$ , we choose  $v = \varphi_k$ ,  $1 \leq k \leq N_h$  and the problem becomes: find  $f_1, \dots, f_{N_h}$  such that

$$- \sum_{i=1}^{N_h} \int_{\Omega} \nabla \varphi_i \cdot \nabla \varphi_k d\Omega = \sum_{i=1}^{N_h} f_i \int_{\Omega} \varphi_i \varphi_k d\Omega.$$

We build the stiffness and mass matrices  $A$  and  $M$  defined by

$$(A)_{ik} = \int_{\Omega} \nabla \varphi_i \cdot \nabla \varphi_k d\Omega \quad \text{and} \quad (M)_{ik} = \int_{\Omega} \varphi_i \varphi_k d\Omega.$$

Finally the solution of the problem (4.9) is given under its matrix form by: find  $\mathbf{f} = (f_1, \dots, f_{N_h})$  such that

$$A\mathbf{v} = M\mathbf{f}, \quad (4.10)$$

where  $\mathbf{v} = (v_1, \dots, v_{N_h})$ .

#### 4.2.2 Computation of the pseudo-ECG summation

As we work on a meshed domain  $\Omega$ , we can approximate the integral in (4.8) by the sum of the quantities evaluated at the nodes, i.e.,

$$ECG_h(e) = \sum_{i=1}^{N_h} \Delta V_m(N_i, t) \cdot \frac{1}{r_i},$$

where  $r_i = \|N_i - \mathbf{x}_e\|$  and  $N_i$  denotes the  $i$ -th node of the mesh. Using (4.10) this becomes

$$ECG_h(e) = \sum_{i=1}^{N_h} f_i \cdot \frac{1}{r_i}.$$

The whole algorithm is given by Algorithm 1.

---

#### Algorithm 1 Pseudo-ECG

---

```

Initialize  $ECG = 0$ ;
Compute the stiffness and the mass matrices  $A$  and  $M$  associated to the finite element space;
for time = 0 to  $T_{max}$  do
  Compute the finite element approximation of the transmembrane potential  $V_m$ ;
  Compute the approximation of the Laplacian of the solution by solving the linear system
   $\mathbf{f} = M^{-1}AV_m$ ;
  for  $i = 1$  to  $N_h$  do
    Compute  $r_i = \|N_i - \mathbf{x}_e\|$ ;
    Sum:  $ECG = ECG + f_i \cdot \frac{1}{r_i}$ ;
  end for
end for

```

---

## 5 Alternans dynamics in cardiac tissue

Cardiac repolarization alternans is a rhythm disturbance of the heart, which leads to beat-to-beat alternation in the duration of the action potential. This phenomenon has been identified as a potential precursor of more dangerous heart diseases, also related to sudden cardiac death. In this perspective, it will be very useful to have a better understanding of the underlying mechanism of this phenomenon.

### 5.1 Action potential alternans

The duration of the cardiac action potential is determined in large part by the preceding diastolic interval and inversely affects the next diastolic interval. The relationship between the diastolic interval and the action potential duration is known as the action potential restitution relation. This electrical restitution is an important determinant in cardiac dynamics.

The duration of each cardiac action potential is an important determinant of electrical stability in the heart. Under normal conditions, as the stimulation frequency is increased—and the diastolic interval is therefore decreased—the resulting action potentials shorten [9]. During fast pacing protocols, the relative duration of systole and diastole are adjusted to ensure an efficient pumping activity. If a second action potential is initiated soon after the first, not all ionic processes have fully recovered their rest state, and therefore the duration of the second action potential is shorter than the first because the transmembrane potential is reduced. This confirms that the action potential duration is a function of both the previous action potential and the diastolic interval [24].

**Electrical restitution** This relation can be studied graphically by plotting the action potential duration against the preceding diastolic interval [38] recorded at a specific location in the tissue. This graph is named *APD restitution curve*. Usually the action potential duration decreases monotonically with decreasing the diastolic interval [23]. The restitution curves associated with the ionic models we study in this project are discussed later in Section 6.

We will see that building such restitution curves leads to many insights into the theory of complex cardiac dynamics and arrhythmias. Especially the slope of this curve may be an important determinant of the stability of the transmembrane potential dynamics. In particular, if the slope of the restitution relation is greater than one, an alternation of the action potential duration—electrical alternans—commonly develops during high frequency pacing.

**Alternans distribution** We are now interested in the distribution of the alternans patterns in the domain. To determine the temporal distribution of action potential alternans across the tissue, we follow the approach of [25]. The amplitude of alternans is defined by the difference between two consecutive action potential durations

$$\Delta APD_n(\mathbf{x}) = APD_{n+1}(\mathbf{x}) - APD_n(\mathbf{x}), \quad (5.1)$$

where  $n$  denotes the beat number and  $APD_n(\mathbf{x})$  is the action potential duration associated to the  $n$ -th beat at location  $\mathbf{x}$ . This quantity (5.1) is used to define the type of alternans associated to each node in the following way:

$$\begin{cases} |\Delta APD_n(\mathbf{x})| \leq 2 \text{ ms} & \text{no alternans or nodal line,} \\ \Delta APD_n(\mathbf{x}) < -2 \text{ ms} & \text{out-of-phase alternans,} \\ \Delta APD_n(\mathbf{x}) > 2 \text{ ms} & \text{in-phase alternans.} \end{cases} \quad (5.2)$$

The phase of alternans is negative for short-long sequences and positive for long-short sequences. When all the tissue present is alternating positively or negatively, we talk about *concordant alternans*. If a point of the tissue has in-phase alternans, and, at the same time, another has out-of-phase alternans, we talk about *discordant alternans*, see Figure 5.1. Nodal lines are defined as areas in which the amplitude is below a fixed threshold —here of 4 ms— that separates out-of-phase regions of discordant alternans. These quantities are illustrated in Figure 5.1. Three-dimensional alternans maps are constructed to explore the spatial distribution of the amplitude and phase of the alternans.

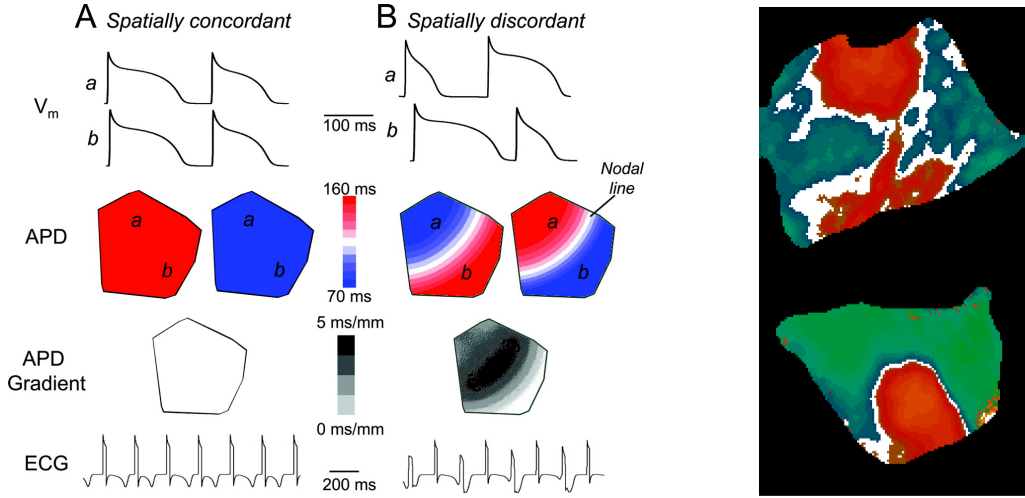


Figure 5.1: Left: spatially concordant (A) and discordant (B) APD alternans in simulated 2D cardiac tissue. Second panel shows that the spatial APD distribution is either long (blue) or short (red for each beat). Third panel shows that the APD dispersion (gray scale) for either long or short beats is minimal. Bottom panel shows simulated electrocardiogram (ECG), with T wave alternans [51]. Right: experimental spatial APD alternans patterns for right canine ventricle [25].

## 5.2 T-wave alternans

T-wave alternans is a periodic beat-to-beat variation in the amplitude or shape of the T-wave (see Figure 4.1) in an electrocardiogram. This variation is a consequence of the alternation in the action potential duration. This relation is shown on Figure 5.2.



Figure 5.2: Left: schematic ECG signal with T-wave alternans and corresponding action potentials [6]. Right: real ECG signal with T-wave alternans [30].

## 6 Numerical results

In this section we discuss all the results related to the numerical simulations. The purpose is to illustrate the theoretical aspects presented in the previous sections. We focus on the three following ionic models: Rogers-McCulloch (RM), Minimal model (MM) and Fox. The simple RM model is used to test and choose the integration method, as the others allow us to reproduce more accurately some physiological phenomena.

We use finite differences to get the approximation of the 1d and 2d models, and the finite element method for the 3d case.

Several programs or languages are used to perform the numerical simulations:

- MATLAB [34]: 0d, 1d and 2d simulations excepted for the Fox model;
- C++: 0d, 1d and 2d simulations for the Fox model;
- the Finite Element Library LifeV [3]: 3d simulations.

Since the 3d simulations could be very long and require high computational performances, we use the Bellatrix cluster in EPFL, whose specifications are given in [2], to perform them.

### 6.1 Choice of the numerical scheme: ionic current integration

We focus on three possible numerical schemes (see Sections 3.2.2 and 3.2.3) to approximate the monodomain equations. These are related to the integration of the ionic current. We want to select the best method with respect to the accuracy of the approximation and to the associated computational cost. We investigate this for the simple RM model and we suppose that similar conclusions are valid for the other ionic models. In this part we always use a parallelepipedal slab of tissue, of dimensions  $1 \times 1 \times 0.0625$  cm.

First we remark that the different approximations can perform quite differently on coarse meshes. Since a first order splitting is used, the approximations obtained with ICI and splitting method are almost identical (see Remark 3.1), but the SVI approximation differs from the previous ones. As predicted in Section 3.2.2, the shape of the action potential is better captured by the SVI method even for coarse meshes, see Figure 6.1. When the mesh is refined, the differences in the shape of the action potential are no longer that evident, see Figure 6.2.

The main difference between the approximations obtained by these three methods is their related conduction velocities. This topic has been discussed extensively in [40] and [39]. We see that the conduction velocity can be very different with respect to the numerical scheme on a coarse mesh, but it converges through the same value when the mesh is refined, see Figures 6.1 and 6.2.

Since we know that on fine meshes these three methods give the same approximation, we can choose a suitable method in terms of computational cost. To this end we record CPU times required for each method. We use the following specifications:

- cellular model: RM;
- domain: parallelepipedal slab of  $1 \times 1 \times 0.0625$  cm;
- number of elements in the mesh:  $16 \times 16 \times 1$ ,  $32 \times 32 \times 2$  and  $64 \times 64 \times 4$ ;
- mass matrix: lumped;
- duration of simulation: 500 ms.

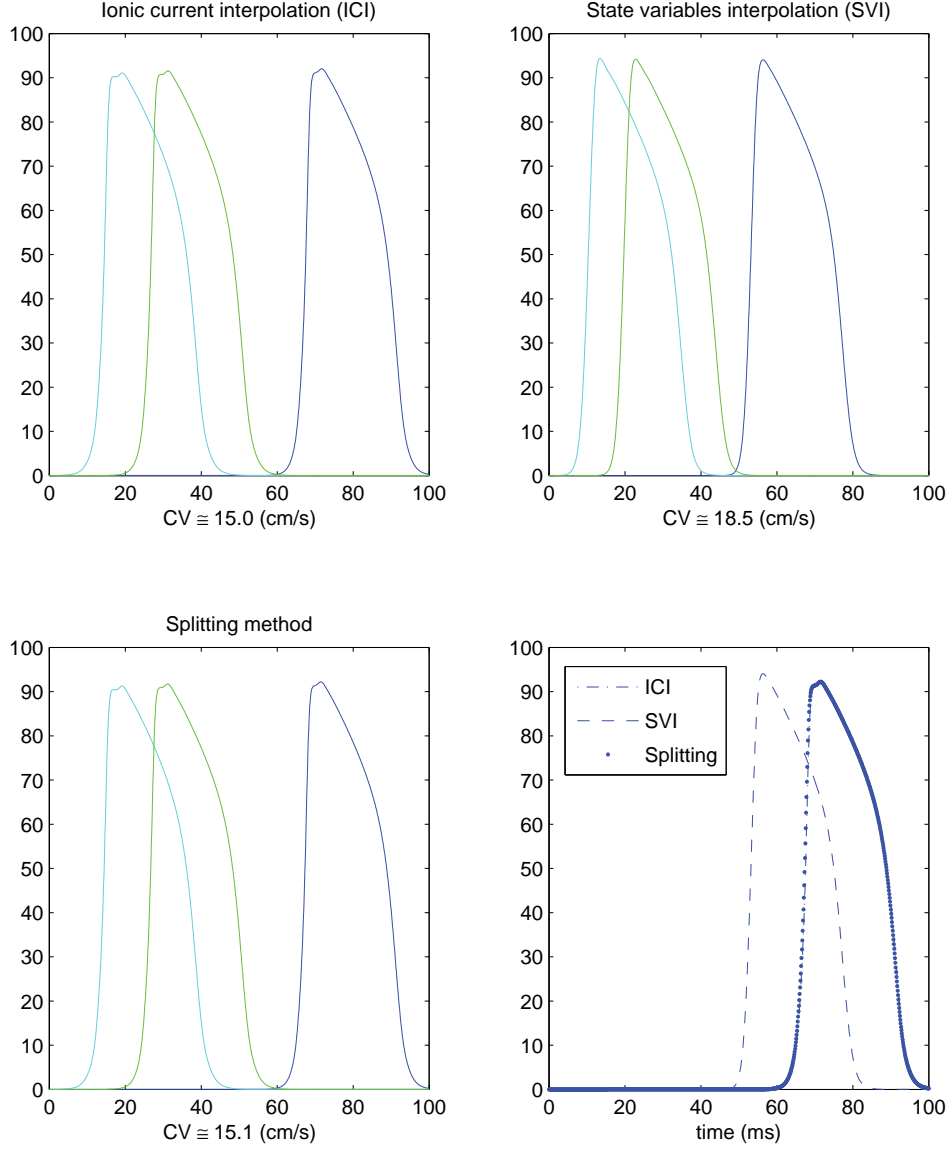


Figure 6.1: Solutions of the monodomain equations using the RM model for the three possible numerical schemes at three different locations along the axis of the wave propagation at distance 1.06 cm, 0.44 cm and 0.27 cm from the pacing site. The last panel shows the resulting action potential for the point farthest from the stimulus location. We use a mesh of  $16 \times 16 \times 1$  elements.

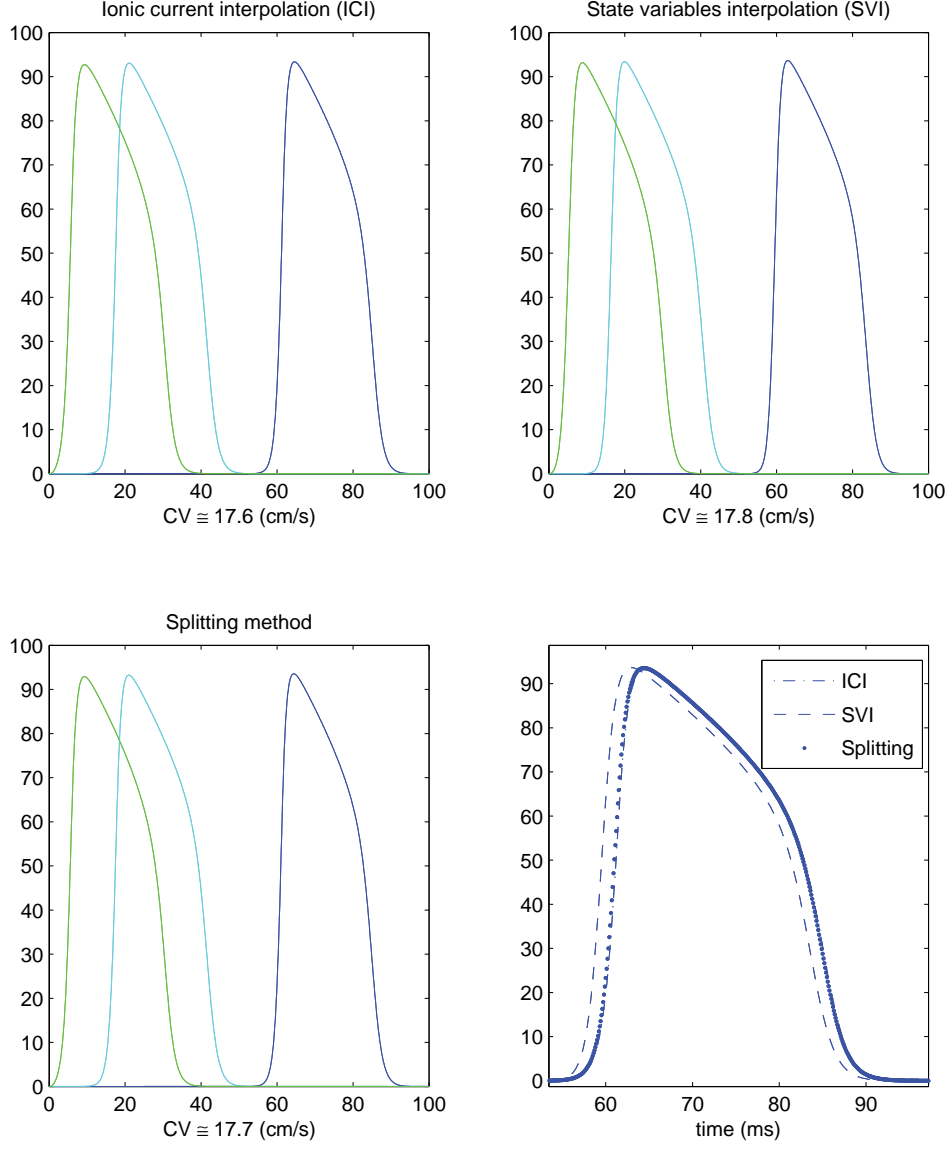


Figure 6.2: Solutions of the monodomain equations using the RM model for the three possible numerical schemes at three different locations along the axis of the wave propagation at distance 1.06 cm, 0.44 cm and 0.27 cm from the pacing site. The last panel shows the resulting action potential for the point farthest from the stimulus location. We use a mesh of  $32 \times 32 \times 2$  elements.

Using one node of the Bellatrix cluster we get the computational times reported in Figure 6.3. We see that the execution time is approximately 1.5 higher for the SVI method than for the other ones. The splitting method is the fastest one. So we choose to use the splitting method for all the next simulations.

Number of elements	Splitting	ICI	SVI
1 536	10.06 s	10.86 s	14.59 s
12 288	20.98 s	17.91 s	33.91 s
98 304	1376.57 s	1653.44 s	2195.96 s

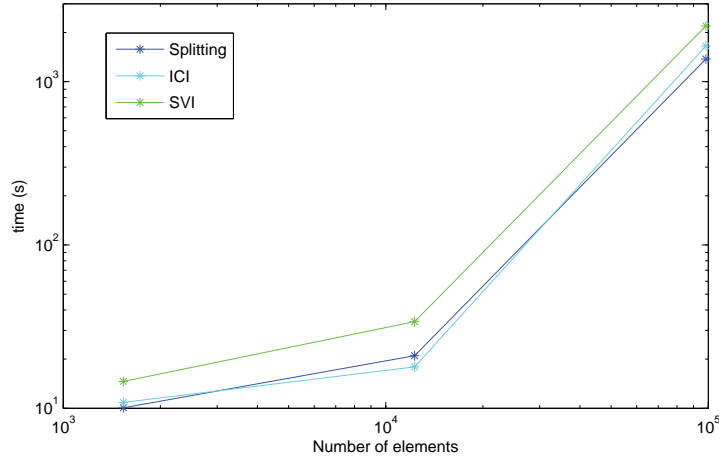


Figure 6.3: Computational times with respect to the numerical scheme and the number of elements of the mesh for a simulation of 500 ms with the RM model.

Furthermore we use here the lumped mass matrix, which induces a further reduction in CPU time. Indeed the computational time is approximately 1.2 times higher with the classical form of the mass matrix. The relative error between these two approximations is reported in Figure 6.4. We see that for a fine mesh —when the convergence for the conduction velocity is reached— the relative error has a mild growth, but it's bounded by 10%. Hence we can use this form of the mass matrix.

Finally, regarding all the previous considerations, we opt to use the splitting method with the lumped mass matrix for all our simulations.

### 6.1.1 Order of the splitting method

As we have seen in Section 3.2.3, it is possible to use different orders of splitting methods. Of course we aim to use the smallest order that provides good accuracy. For the RM model a first order splitting method is enough. Indeed, we see in Figure 6.6 that the conduction velocity converges to the desired value.

For the MM, the first order splitting doesn't give satisfactory results. In fact we don't reach the convergence for the conduction velocity and furthermore this value is too high. To gain in accuracy and solve this issue, we implement the numerical scheme given by (3.16), namely:

- a second order splitting method;
- a second-order backward differentiation formula (BDF2) for the diffusion part.



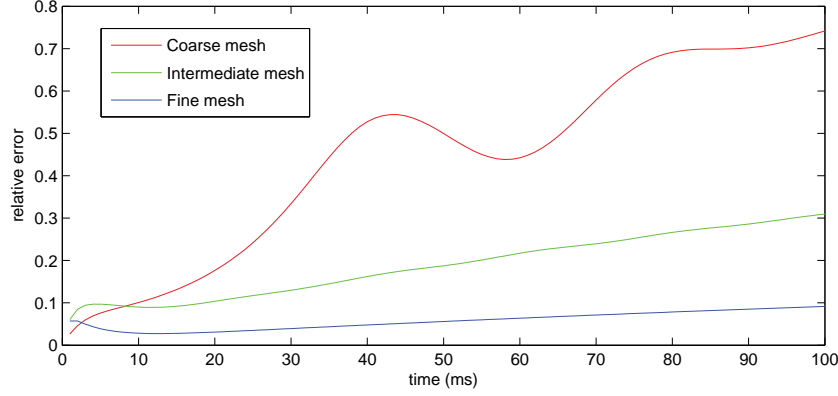


Figure 6.4: Relative error between the approximations given by the splitting method using or not the lumped mass matrix for the meshes mentioned previously.

With these modifications, the conduction velocity we get is correct (with respect to the physiological value) and the convergence is reached.

These findings suggest that a second order method is required to efficiently solve the monodomain equations when the shape of the action potential has a stiff upstroke. We use this strategy for the MM and the Fox model.

### 6.1.2 General parameters

For all the simulations we use piecewise linear finite elements  $\mathbb{P}_1$  for the scalar fields and a GMRES solver with the following parameters:

- tolerance:  $10^{-10}$ ;
- maximum number of iterations: 200;
- dimension of the Krylov spaces: 100.

This solver is presented in detail in [44]. All linear solvers used in LifeV are provided by the library Trilinos [26].

## 6.2 Conduction velocity

The conduction velocity is an important property of the cardiac tissue and has to be reproduced correctly by the model. We'll see that it is not a simple problem, and it is related to the mesh size and the accuracy of the numerical scheme.

The diffusion coefficient is obtained from experimental data and, using the formalism of Section 2.3, we have in this case:

- $\sigma_l = \sigma_t = \sigma_n = 0.001 \text{ cm}^2/\text{ms}$  in the isotropic case;
- $\sigma_l = 0.001 \text{ cm}^2/\text{ms}$  and  $\sigma_t = \sigma_n = \frac{\sigma_l}{5} = 0.0002 \text{ cm}^2/\text{ms}$  in the anisotropic case.

### 6.2.1 Relation with the mesh size

As we have seen before, we have to pay attention to the choice of the mesh size. As mentioned in Remarks 2.1 and 2.3, the mesh size is closely related to the conduction velocity and has to be small enough to reproduce it correctly according to the diffusion coefficient. Otherwise we

may solve a different diffusion problem and the results won't be correct from the physiological point of view.

We'll see that the conduction velocity becomes stable with the decrease of the mesh size. So we choose the biggest mesh size giving the convergence and the right conduction velocity according to the physiological value. We first investigate the 1d case for the two phenomenological models and then we go to the 3d cases.

**1d case** We present here the convergence of the conduction velocity with respect to the mesh size for the RM and the MM in the 1d case. We use a cable of length  $L = 2$  cm and we solve the cable equation for a mesh size  $dx \in [0.001, 0.1]$ . A wave is generated by a stimulus at one end and propagates along the cable. For each value of  $dx$  we compute the corresponding conduction velocity. The values are reported in Figure 6.5.

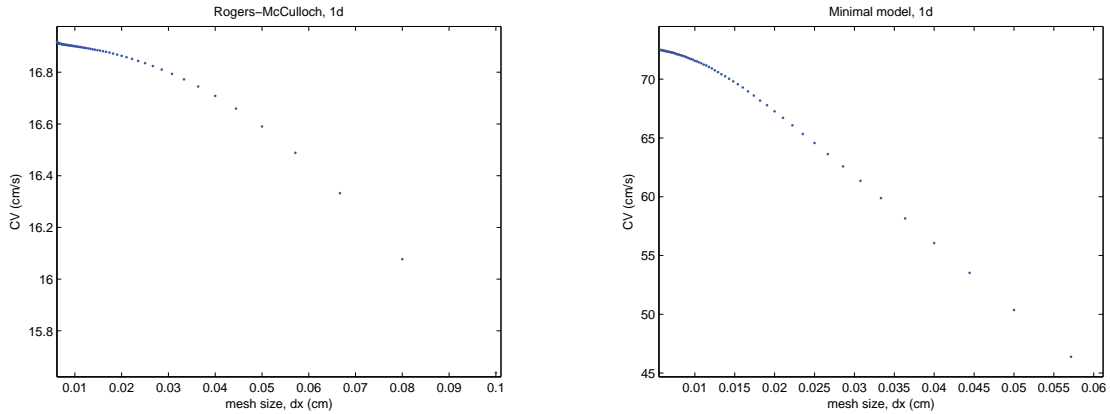


Figure 6.5: Evolution of the conduction velocity according to the mesh size for the Rogers-McCulloch (left) and the Minimal (right) models in the 1d case.

We note that for both models the speed stabilizes when the mesh size is small enough and we get the correct values according to [12]. It is also interesting to notice that the speed of convergence is related with the complexity of the cell model. We suggest that may be due to the shape of the induced action potential. Since a smaller mesh size is required to reproduced the very stiff upstroke arising in the MM.

Therefore we have to select the right mesh size for each cell model. In these cases, if  $dx = 0.025$  cm is sufficiently small for the RM model, the corresponding  $dx$  for the MM model is less than 0.01 cm.

### Remark 6.1

We note that it is necessary to use very fine meshes to correctly reproduce the physiological properties of cardiac tissue. This will imply a high computational cost, especially in the 3d case.

**3d case** We investigate now the behavior of the RM and MM models on a 3d case. We use an isotropic parallelepipedal slab domain of  $1 \times 1 \times 0.0625$  cm. We use a tetrahedral structured mesh and  $dx$  refers to the length of the smallest edge of each element. We generate a plane wave by stimulating one side of the domain and let it propagate.

As reported in Figure 6.6 (left), similar results as in the 1d case are obtained in the 3d case for the RM model. The conduction velocity stabilizes for a  $dx$  around 0.025 cm.

The case of the MM model is more complicated. Indeed we saw in Section 6.1.1 that the first order splitting doesn't give good results. With this method the resulting conduction velocity is too high with respect to the physiological value and the convergence is not reached. To improve this we adopt the second order splitting method getting similar values as in the 1d case. The results are reported in Figure 6.6 (right).

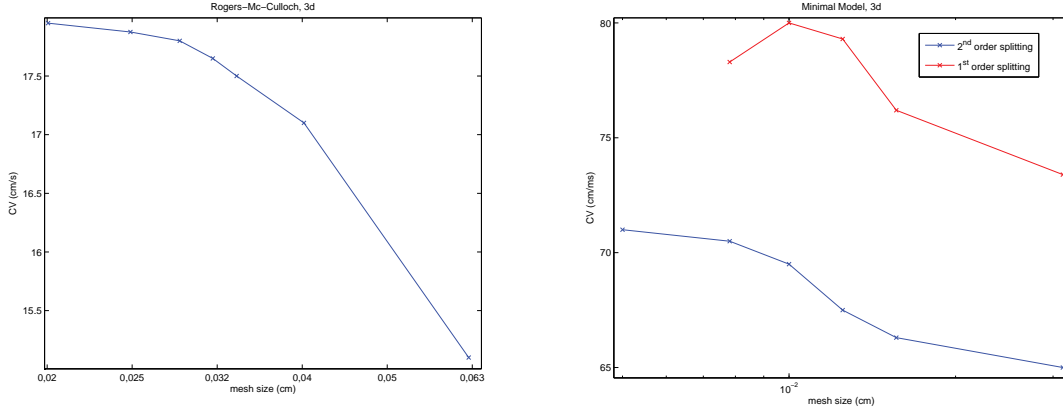


Figure 6.6: Evolution of the conduction velocity according to the mesh size for the RM and the MM models in the 3d case.

For the Fox model, even with the finest mesh previously used, we don't reach convergence. The conduction velocity still increases linearly and we don't get the physiological value. This could be related with the stiffness of the currents involved in the model. However, further investigations are needed in this direction. For instance, a higher order splitting method or time discretization could improve the accuracy of the conduction velocity approximation.

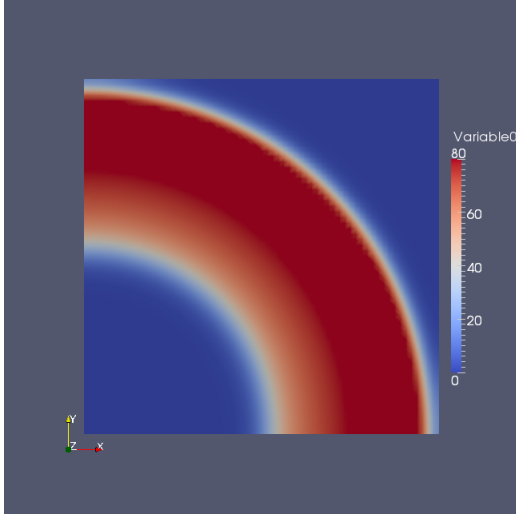
This issue could also be related to the approximation of the reaction term. Indeed the splitting method is based on the ICI method and, since  $\mathbb{P}1$  elements are used, a linear interpolation of the reaction term is performed. However, in general, the reaction term is highly non linear and can be very stiff. Hence a linear interpolation could produce large approximation error increasing with the number of variables of the model. This could be also an explanation of the convergence lacking of the conduction velocity with the Fox model.

### 6.2.2 Effect of anisotropy

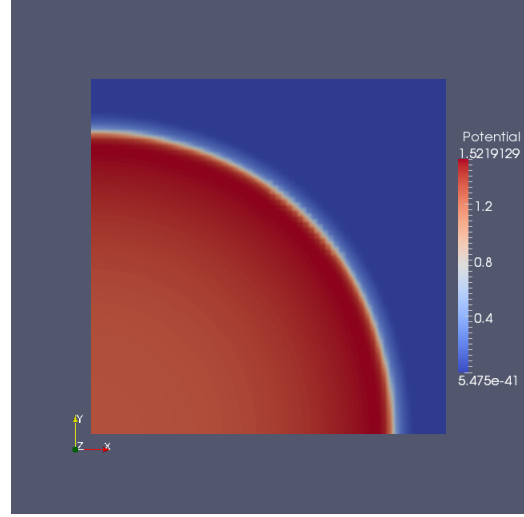
We include now the effect of anisotropy in the model and perform some testing simulations. We use here the same domain as before where fibers are straight lines crossing the  $x$ -axis with an angle of  $60^\circ$ , corresponding to the endocardial layer. We put a stimulus at one corner of the domain and let it propagate.

We see that the location of the pacing site has an influence on the shape and the speed of propagation wave in the anisotropic case. In the isotropic case the action potential wave is always spherical, but in the anisotropic case it becomes ellipsoidal or almost planar depending on the pacing site, see Figure 6.7. Furthermore, the wave propagates faster when the stimulus is applied along the fibers direction.

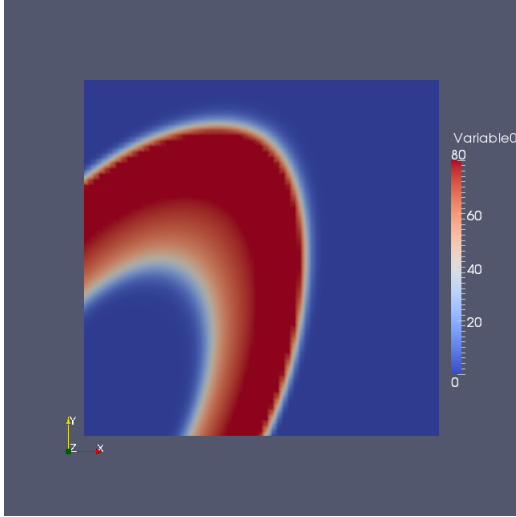
Anisotropy induces an effect on the conduction velocity too, but in this case we are only able to compute a local conduction velocity. Taking into account the direction of propagation of the wave, we determine the conduction velocity along the fibers ( $CV_{//}$ ) and orthogonal to the fibers ( $CV_{\perp}$ ). We obtain the values reported in Table 6.1 for the RM and MM models, respectively, adopting sufficiently fine mesh according to the previous considerations (see 6.2.1).



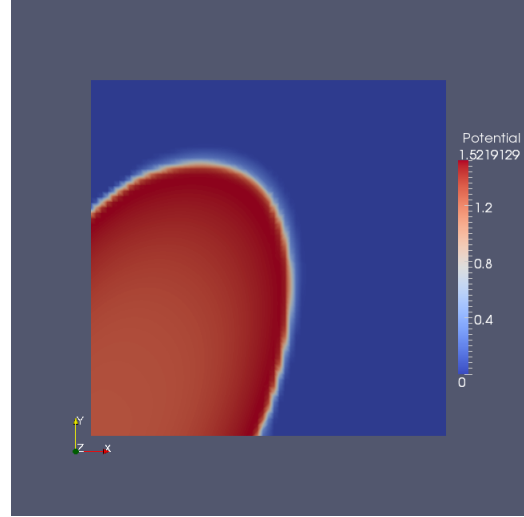
(a)  $t = 50$  ms, pacing site  $(0,0,0)$  (isotropic)



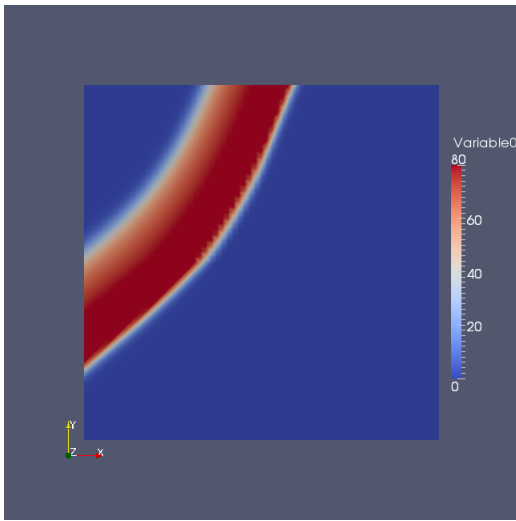
(b)  $t = 12$  ms, pacing site  $(0,0,0)$  (isotropic)



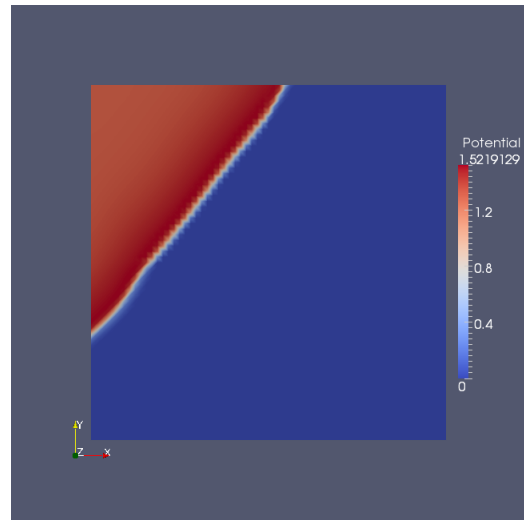
(c)  $t = 50$  ms, pacing site  $(0,0,0)$  (anisotropic)



(d)  $t = 12$  ms, pacing site  $(0,0,0)$  (anisotropic)



(e)  $t = 50$  ms, pacing site  $(0,1,0)$  (anisotropic)



(f)  $t = 12$  ms, pacing site  $(0,1,0)$  (anisotropic)

Figure 6.7: Effect of anisotropy and pacing site on a action potential wave propagation for RM (left) and MM (right).

Rogers-McCulloch	Minimal model
$CV_{//} = 18.5 \text{ cm/s}$	$CV_{\perp} = 8.8 \text{ cm/s}$
$CV_{//} = 66.3 \text{ cm/s}$	$CV_{\perp} = 31.4 \text{ cm/s}$

Table 6.1: Local conduction velocities for RM and MM in the anisotropic case.

We see in Table 6.1 that the orthogonal conduction velocity is scaled down by a factor around 0.47 from the velocity along the fibers. Such a result is predictable with respect to the value of the conductivity tensor. Indeed, in theory, we have the relation [17]:

$$CV_{\perp} = \left( \frac{\sigma_t}{\sigma_l} \right)^{\frac{1}{2}} CV_{//}.$$

Finally the two models correctly reproduce the restitution relations of the conduction velocity.

### 6.3 Restitution curves

In this part we build and study the restitution curves associated to our models. First we focus on the two simpler phenomenological models and then we address the Fox model. We remind that these graphs are obtained by plotting the action potential duration (APD) versus the duration of the previous diastolic interval (DI). These data are related to the specific pacing protocol explained hereunder.

**Pacing protocol** To build the restitution curves we use the following pacing protocol, named *pacing down* protocol: given a first cycle length (CL) and a reduction factor  $\delta t$ , for a number of stimulations  $n$ , we

- pace every CL ms,
- reduce the pacing interval of  $\delta t$  ms.

This is done until a fixed minimal cycle length is reached, or capture is lost.

#### Remark 6.2

The number of stimulations  $n$  given at each fixed CL has to be chosen in regard to the complexity of the ionic model. In general, the more complex the model the more stimulations are needed. It is possible to use an adaptive  $\delta t$  and decrease this value when the associated CL becomes smaller.

For each pacing frequency, the last two APDs and DIs are recorded (if there are no alternans, only the last ones are needed). These values are computed at a fixed point of the domain, far enough from the location of the stimulus.

#### 6.3.1 Electrical restitution of the RM and MM models

The restitution curves are built using the previous pacing protocol with  $\delta t = 5 \text{ ms}$  and  $n = 5$ . In any case the mesh size has to be small enough to reproduce the correct conduction velocity, see Section 6.2.1.

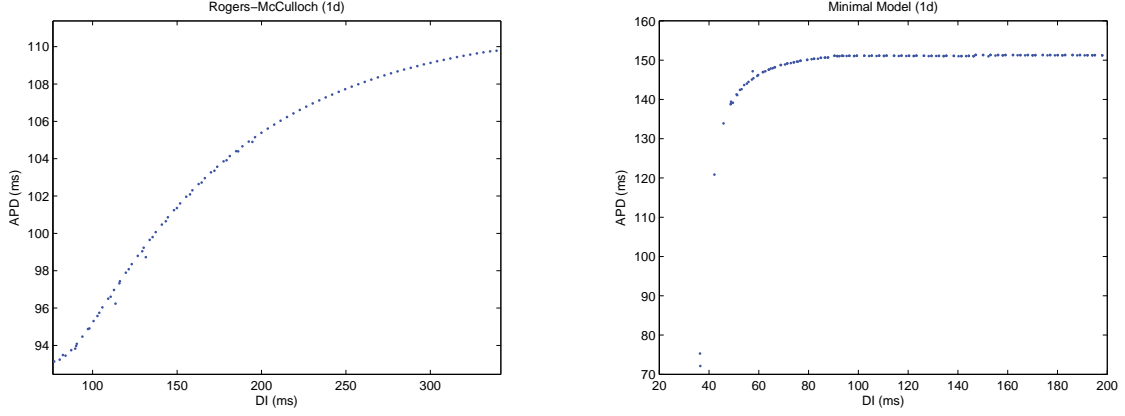


Figure 6.8: Restitution curves for the RM and MM models for the 1d case.

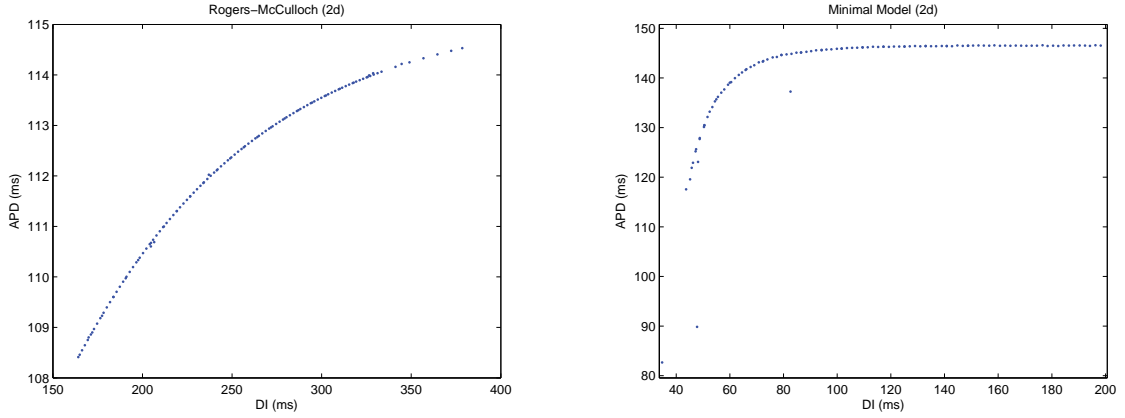


Figure 6.9: Restitution curves for the RM and MM models in a 2d case.

**1d case** The domain is a cable of length  $L = 2$  cm. The stimuli are applied to one end of the cable and the data are recorded at a fixed point far from the location of the stimulus. The restitution curves associated to these two models are shown in Figure 6.8.

The two models have different restitution curves. The curve associated to the RM model is smoother and decreases more progressively. The MM has a stable APD with respect to the associated DI until this value goes under a critical threshold, around 80 ms in this case. Then the APD decreases rapidly and hence the slope of the curve becomes higher.

**2d case** The domain is a square of  $1 \times 1$  cm. The stimuli are applied to one corner of the domain generating spherical waves that propagate across the domain. The data are recorded at a fixed point far from the stimulus location and in the direction of the propagating wave —along the diagonal of the square through the stimulus location. The restitution curves associated to these two models are shown in Figure 6.9.

The results are similar to those obtained for the 1d case.

In the anisotropic case, we see that the restitution properties depend on the recording location. The shape of the curve is conserved, but the stable APD varies through the domain. This is more visible with the MM, see Figure 6.10.

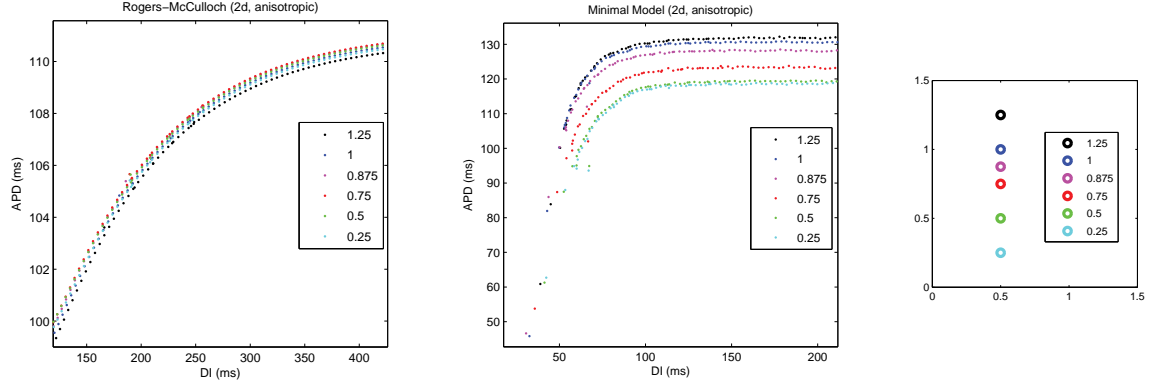


Figure 6.10: Left: restitution curves for the RM and MM models in an anisotropic 2d case with respect to the recording locations. Right: recording locations.

### 6.3.2 Electrical restitution of the Fox model

Since an important topic of this project is the study of alternans dynamics in canine heart tissues, we discuss in details the results associated to the Fox model. Indeed this model has been developed to reproduce complex behaviors and dysrhythmias in canine hearts. We analyze here the results associated to the cellular model.

The systematic study of this model allows us to validate our implementation of the cellular model and his integration in the LifeV architecture.

**Cellular model** Figure 6.11 illustrates the action potentials generated by the Fox model at different pacing cycle lengths. The action potential is characterized by the familiar spike-and-dome morphology associated with canine myocardial cells and its duration decreases with acceleration of the pacing.

The restitution curves give some information about the critical cycle length for the alternans onset. Figure 6.12 shows the relationship between action potential duration and the pacing cycle length over the range of cycle length that produced alternans —400 – 90 ms. We see that the slope of the curve, greater than one, in the left panel (APD versus DI) of Figure 6.12 is an indicator about the presence of alternans [38]. The right panel of the same Figure shows that the curve (APD versus CL) splits for the CL leading to alternans. These CLs correspond to the ones associated with a slope greater than one in the left panel.

## 6.4 Pseudo-ECG

The electrocardiogram is the most used device to record and analyze the electrical activity in the heart. This tool is used to record the external potential at the body surface. So it is a non invasive device and it is widely used to detect arrhythmias. We have presented in Section 4 a method to reproduce the external potential at a fixed location away from the myocardium and now we test this method on the different simulations.

### 6.4.1 Resolution of the linear system

The computation of the pseudo-ECG is quite different in the 1d or 2d cases than in the 3d case. Indeed in the first case, since finite differences are used, we get the Laplacian of the transmembrane potential computing directly its discrete form. As discussed in Section 4.2, the

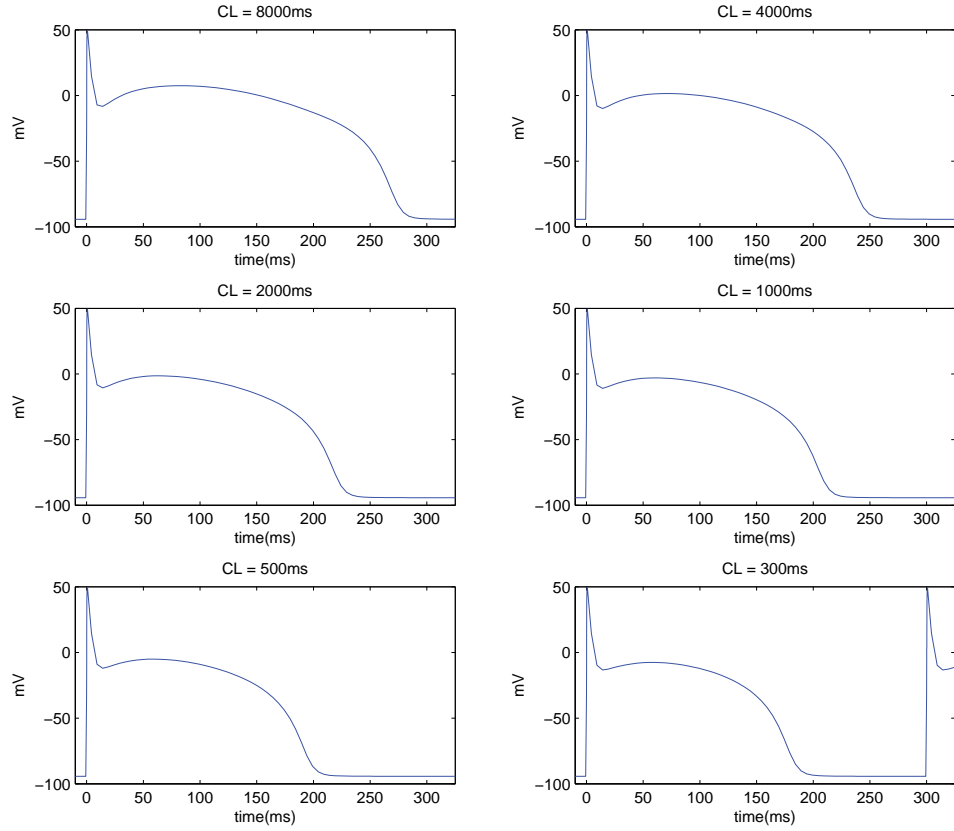


Figure 6.11: Examples of action potentials at different pacing cycle length according to the Fox model.

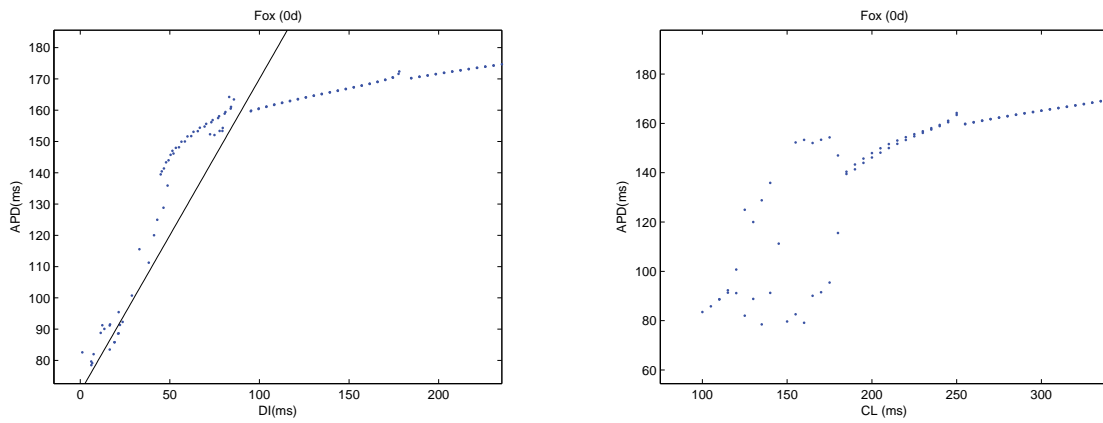


Figure 6.12: Restitution curves for the 0d Fox's model: APD versus DI (left) and APD versus CL (right).



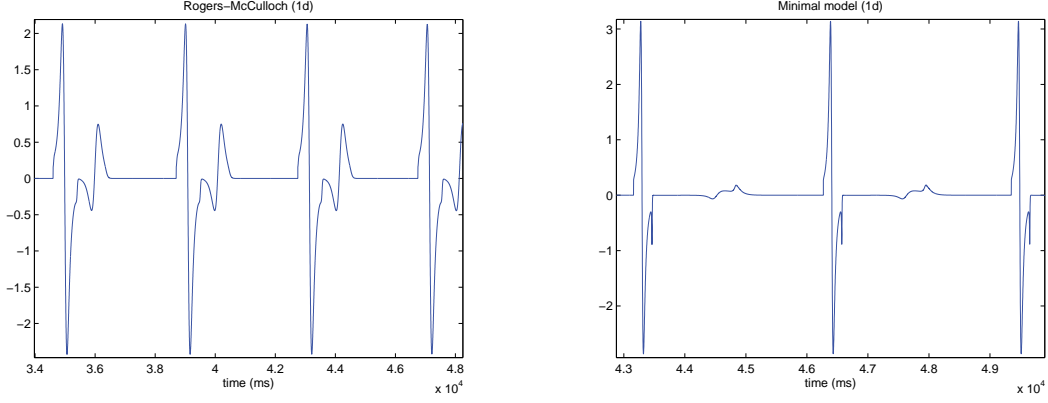


Figure 6.13: ECG profiles for the RM and MM 1d models.

3d case is not so straightforward and requires the resolution of the system (4.10). We perform this using the solver block-GMRES with the following parameters:

- preconditioner: ML;
- preconditioner side: right;
- tolerance:  $10^{-10}$ ;
- maximum number of iterations: 200.

A multigrid (ML) preconditioner is used because it is very efficient for the Laplacian problem [46]. Since the resulting matrix is symmetric, we can use the following parameters:

- smoothing: pre (at the begining of the resolution algorithm);
- smoother: symmetric Gauss-Seidel;
- solver on the coarse mesh: Amesos-KLU;
- aggregation threshold: 0.01.

This method can save around 10% of computation time compared to the standard method using the preconditioner Ifpack. We notice also that less memory is used in that way.

## 6.4.2 Results

We present here the resulting signals obtained from several simulations. The three models are used in both isotropic and anisotropic cases. We reproduce also signals associated to cardiac rythm disorders, like spirals. ECG signal related to cardiac alternans are discussed in the next Section 6.5.2.

**Normal rythm** Figures 6.13–6.15 show the pseudo-ECG signals associated with the RM and the MM model in the 1d, 2d and 3d cases. These records come from simulations with a fixed pacing cycle length and no alternans. We see that in all cases the shape of the signal is correct with respect to Figure 4.1. The QRS complex and the T-wave are reproduced correctly.

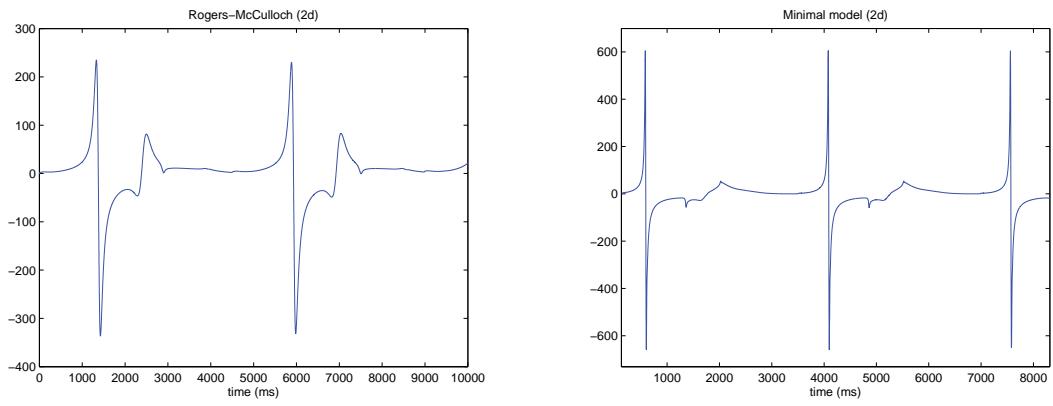


Figure 6.14: ECG profiles for the RM and MM 2d models.

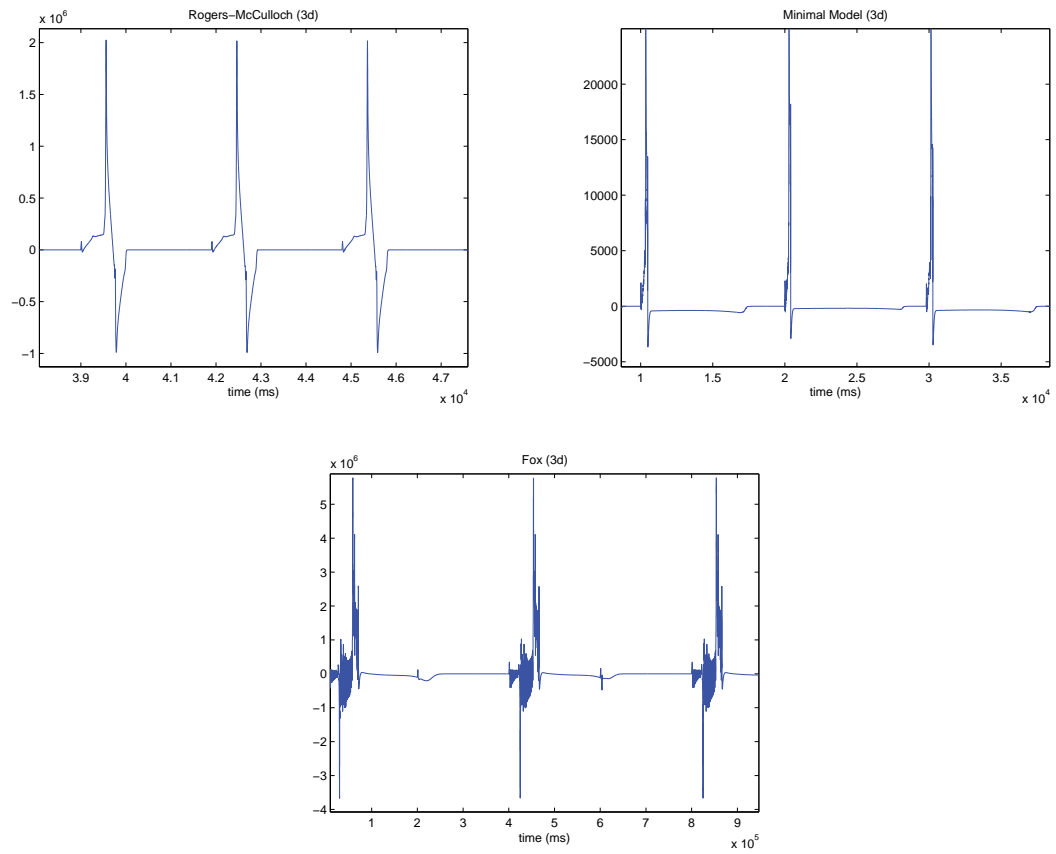


Figure 6.15: ECG profiles for the 3d models.

**Rythm disorder** Since the pseudo-ECG reproduces correctly the signal in the case of normal cardiac rythm, we want to see if it is also the case when arrythmias are present. First we use the RM model in both isotropic and anisotropic cases and we generate a spiral wave. Spiral waves are associated with tachycardia and fibrillation [11].

We use the parallelepipedal slab domain with  $32 \times 32 \times 2$  elements. The spiral is generated by:

1. inducing a plane wave by activating the part of the tissue corresponding to  $x < 0.1$  cm;
2. resetting artificially the potential to its rest value after a fixed time  $T$  in the region of the tissue corresponding to  $y < 0.1$  cm.

In the isotropic case the spiral disappears after 420 ms but in the anisotropic case the spiral stabilizes into the domain —continuous relation. Figures 6.16 and 6.17 show the spatial map of the action potential and the related ECG signals. As expected, both cases present perturbed ECG signals. In the isotropic case, since the spiral wave can't stabilize, the initial form of the signal can be recognized but the QRS complex shows obvious abnormalities, see Figure 6.16.

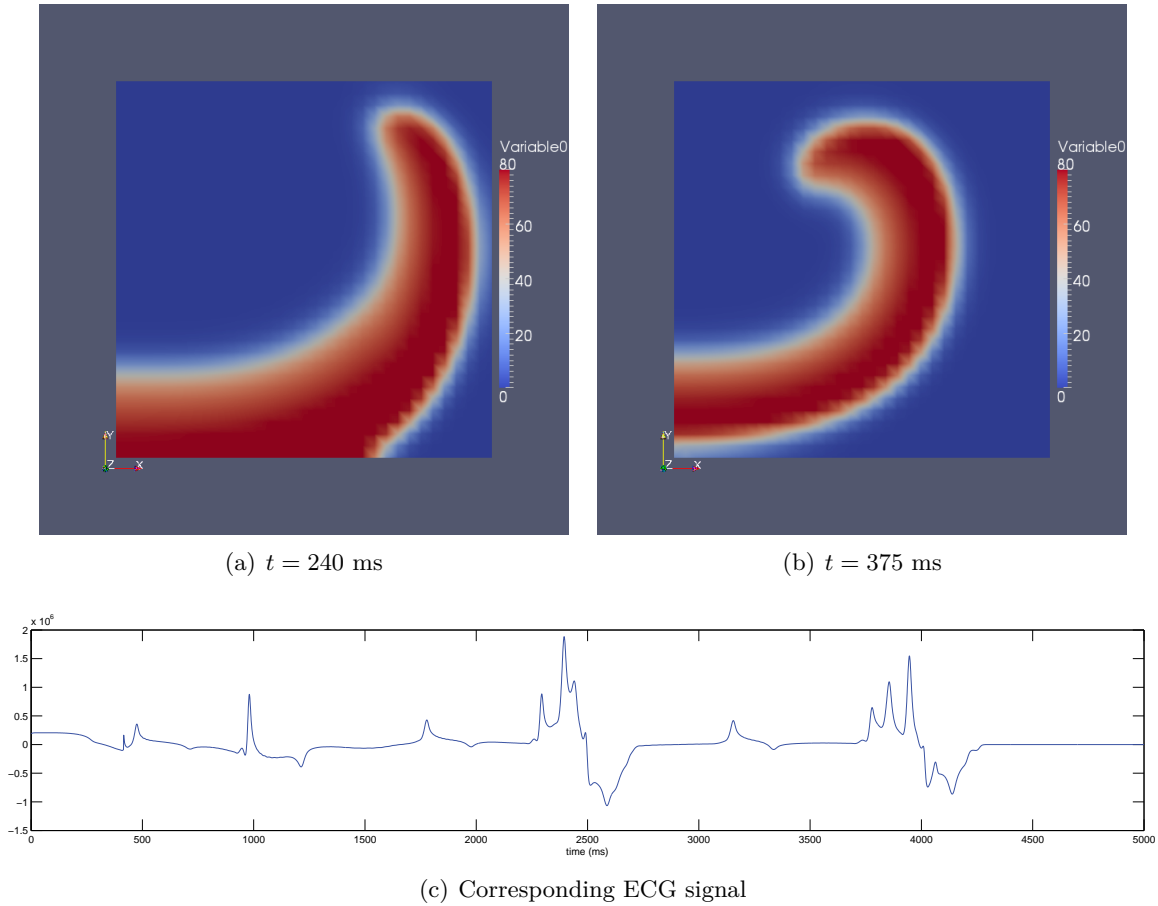


Figure 6.16: Top: spiral wave generated by the RM model in an isotropic domain. Bottom: corresponding ECG signal.

For the anisotropic case we consider a thin slice of the myocardium ventricular domain presented in Figure 2.8 corresponding to the endocardial layer. The fibers are straight lines in the  $Oxy$  plane and have an angle of  $60^\circ$  with the  $x$ -axis. In this case we see that the spiral wave

reaches a periodic state and, after stabilization around  $t = 4.5$  s, the general form of the signal is completely destroyed, see Figure 6.17.

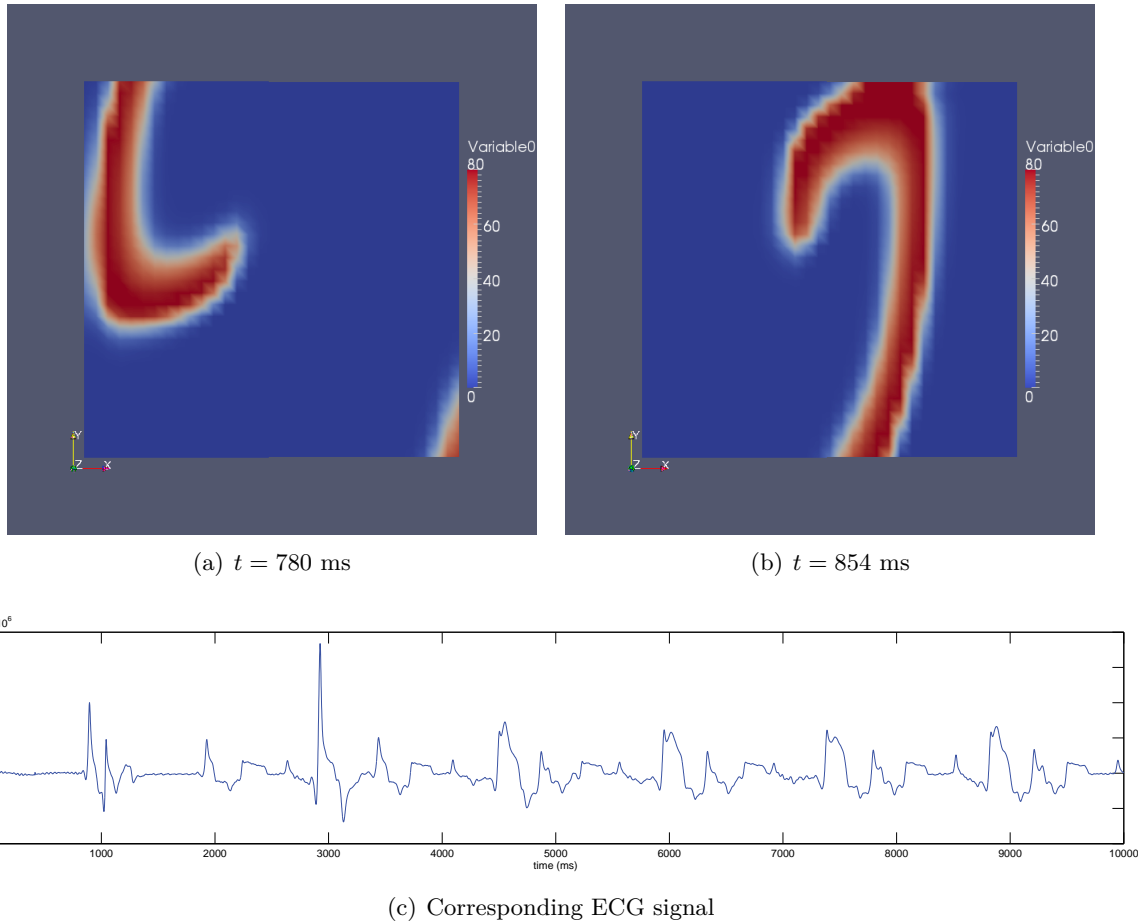


Figure 6.17: Top: Spiral wave generated by the RM model in an anisotropic domain. Bottom: corresponding ECG signal.

## 6.5 Alternans dynamics

We will see that the aim of the Fox model is to provide a physiological model reproducing stable electrical alternans. We discuss the properties of this cellular model and then we study the presence of alternans in 3d tissues.

### 6.5.1 Fox model

This section is related with the Fox model. We investigate the presence of alternans in a single cell and the relation with calcium dynamics.

**Cellular model** The Fox model generates electrical alternans over a wide range of pacing cycle lengths, in association with a region of the restitution relation having a slope close to one, see Figure 6.12. At cycle lengths smaller than 130 ms no alternans is generated, APD-CL rejoining. We notice that initially the magnitude of alternans increases as the pacing cycle is shortened, and then decrease until there is alternans anymore. Using the graphs of Figure 6.12, we know which cycle length will induced alternans, that is for  $\sim 130 < CL < 180$  ms.

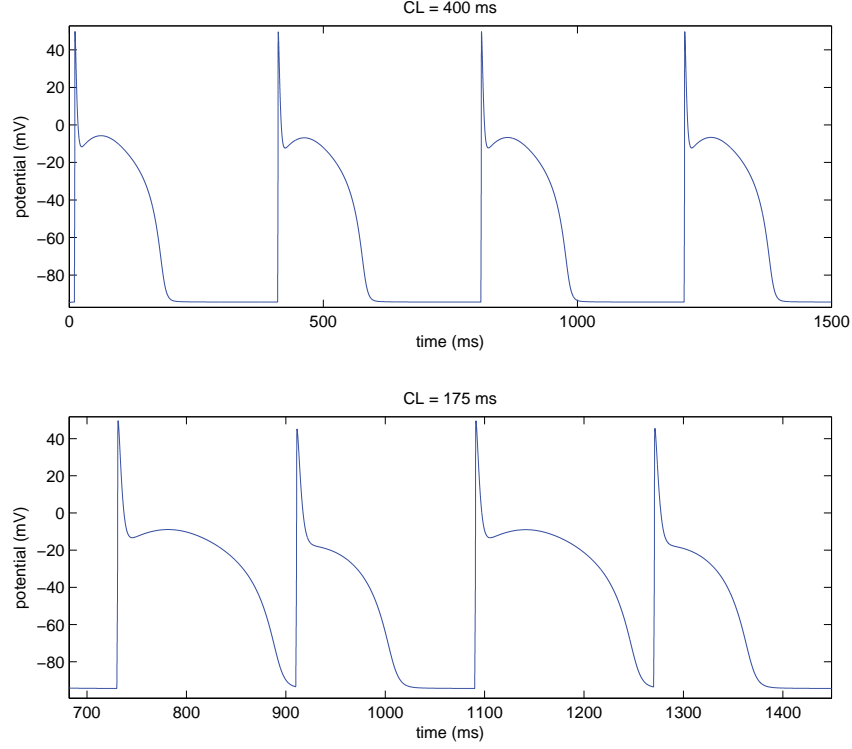


Figure 6.18: Action potential generated by the Fox model during normal rythm and alternans.

Figure 6.18 shows the typical shape of the action potential during normal rythm and large magnitude alternans.

**Calcium dynamics** The study of the evolution of the different quantities involved in the Fox model shows that alternans are closely related with calcium dynamics. Figure 6.19 illustrates that when alternation occurs in the transmembrane potential also alternation of the  $f_{Ca}$  gating variable arises, the intracellular calcium concentration and the L-type  $Ca^{2+}$  channel current. The magnitude of alternans is significant for all of these variables.

The large difference in  $I_{Ca}$  between the long and short action potential shown in Figure 6.19 suggests that  $I_{Ca}$  contributes significantly to the development of alternans. The evolution of this current is closely related to the time-dependent behavior of the calcium-induced inactivation gate  $f_{Ca}$ . It could be shown that the reduction of the  $I_{Ca}$  current could reduce the magnitude of alternans or eliminate them [20]. The intracellular calcium concentration  $[Ca]_i$  is immediately affected by the alternation of the calcium current as well. This has also strong relations with drugs' effects.

### 6.5.2 Spatial distribution in 3d tissues

We discuss here the presence of alternans in cardiac tissues. We see that both MM and Fox models are able to reproduce transient alternans patterns. Since we are able to recover the desired conduction velocity of the MM model and it requires less CPU time, we use this to illustrate some typical patterns.

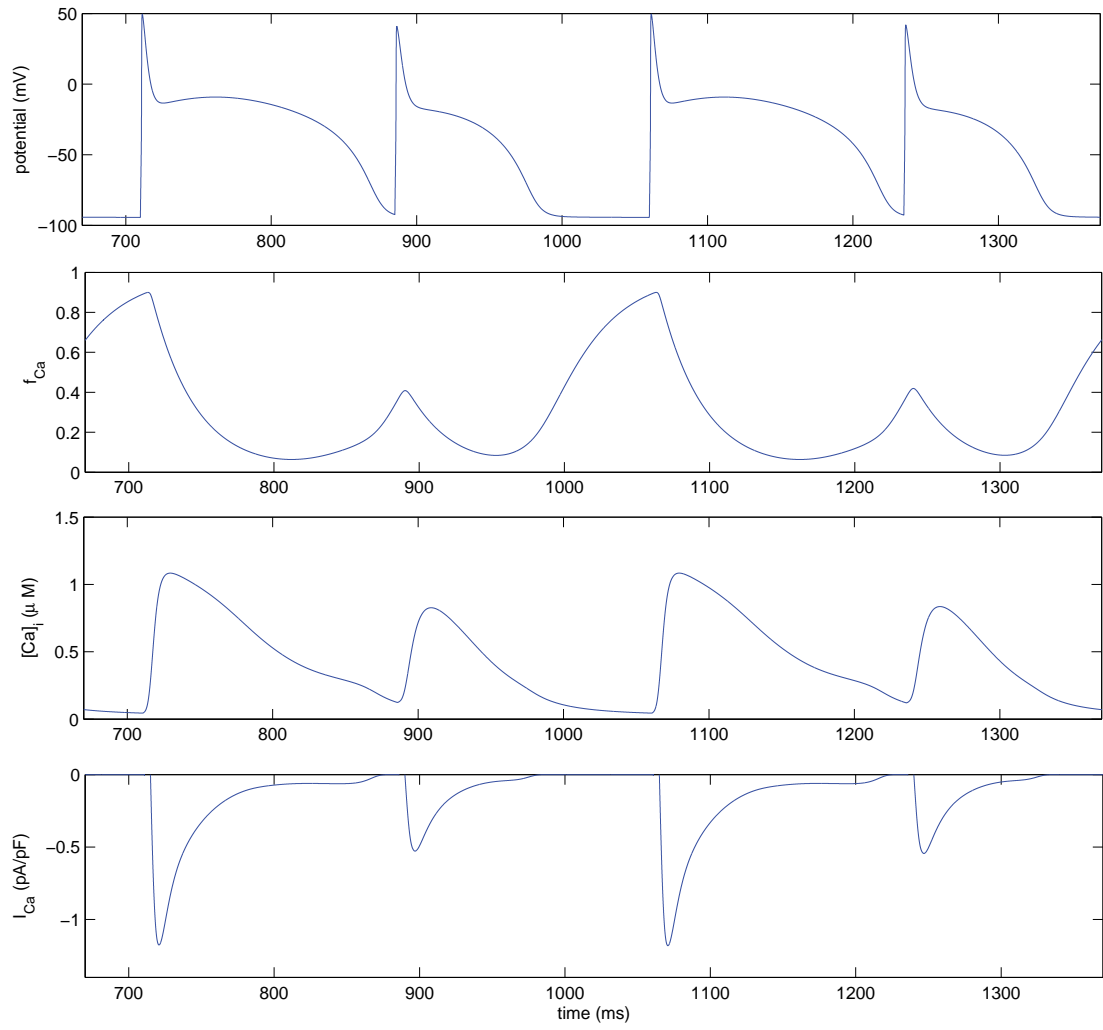


Figure 6.19: From top to bottom: action potential,  $f_{Ca}$  gating variable, intracellular calcium concentration, and L-type  $Ca^{2+}$  channel current generated by the Fox model at pacing cycle length of 175 ms.

Furthermore, we'll see that the geometry of the tissues has an influence on the spatial distribution of APD alternans.

**Isotropic case** We know that fast pacing rates can generate APD alternans. Here we use a different pacing protocol (quiescent protocol): we start from resting initial condition and directly pace at the desired frequency. We see that a pacing period of 210 ms induces alternation of the action potential duration with the MM model. In fact, only one over two action potentials is kept and so, the effective cycle is 420 ms. In the isotropic case the spatial distribution of alternans is homogeneous and we get only spatially concordant alternans.

We notice that the presence of alternans is confirmed by the splitting of the restitution curve. The local restitution curve related to this specific cycle length is presented in Figure 6.20 (right).

We also see that, as predicted, there is a correlation between the presence of APD alternans and T-wave alternans, see Figure 6.20 (left). If the alternation in the action potential duration induces T-wave alternans, we notice that the alternation in the amplitude induces alternation of the QRS complex amplitude in the pseudo-ECG signal.

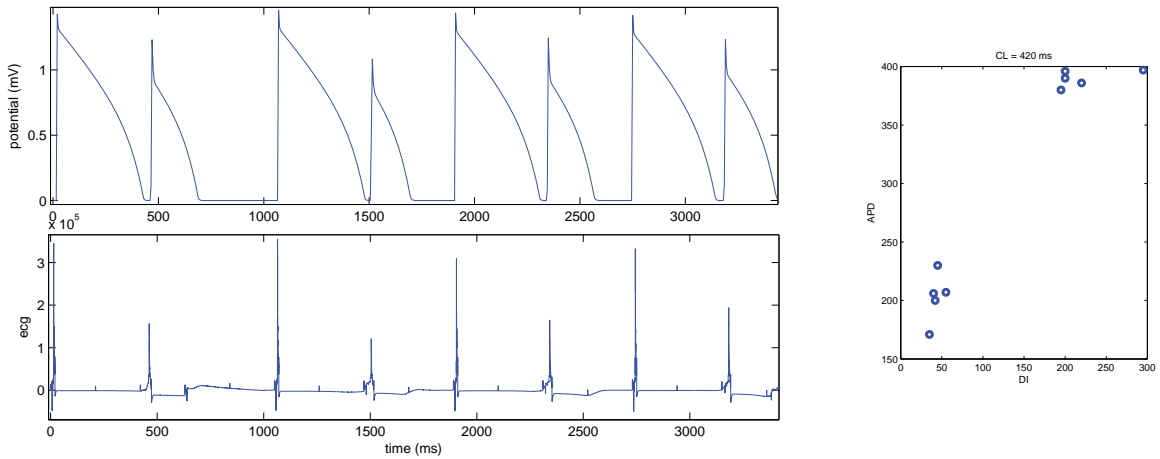


Figure 6.20: Left: action potential and related ECG signal produced by the MM. Right: local restitution curve.

**Anisotropic case** We use the same pacing rate and we put the stimulus in two different pacing sites, namely in  $(0, 0, 0)$  and  $(0, 1, 0)$ . In this case too, only one over two action potentials is kept. The resulting spatial distribution of the transient alternans is no longer homogeneous and we get spatially discordant alternans.

The direction of the fibers plays an important role in the spatial distribution of the alternans. Hence we get different patterns according to the pacing site, see Figures 6.21 and 6.22. We see that the underlying shape is related to the shape of the action potential wave according to each pacing site.

Each pattern is confirmed by the evolution of the transmembrane potential in the mentioned location: in-phase alternans in A, out-of-phase alternans in B and nodal line in C (see right pannels of Figures 6.21 and 6.22).

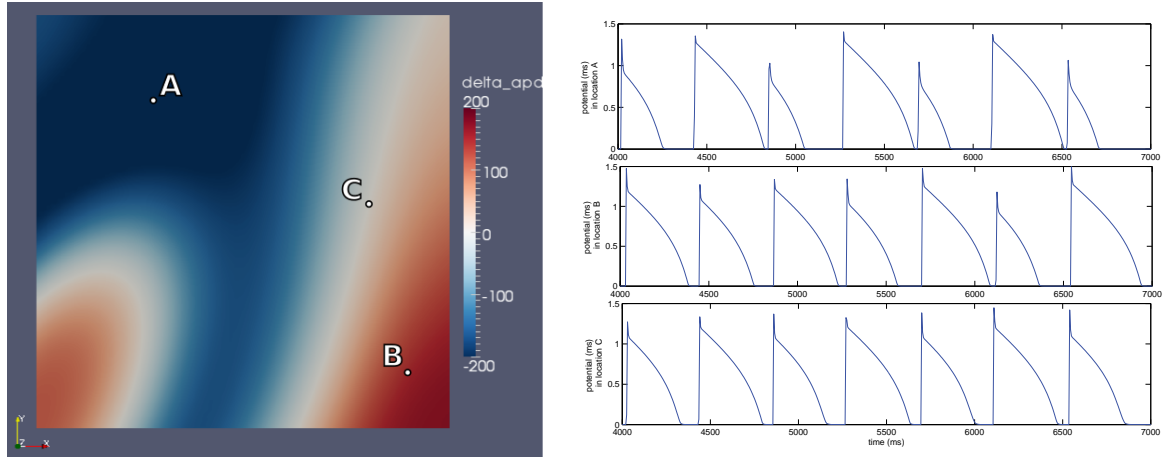


Figure 6.21: Left: spatial distribution of  $\Delta APD$  showing discordant alternans related to the pacing site  $(0,0,0)$ . Right: action potential at locations A, B and C.

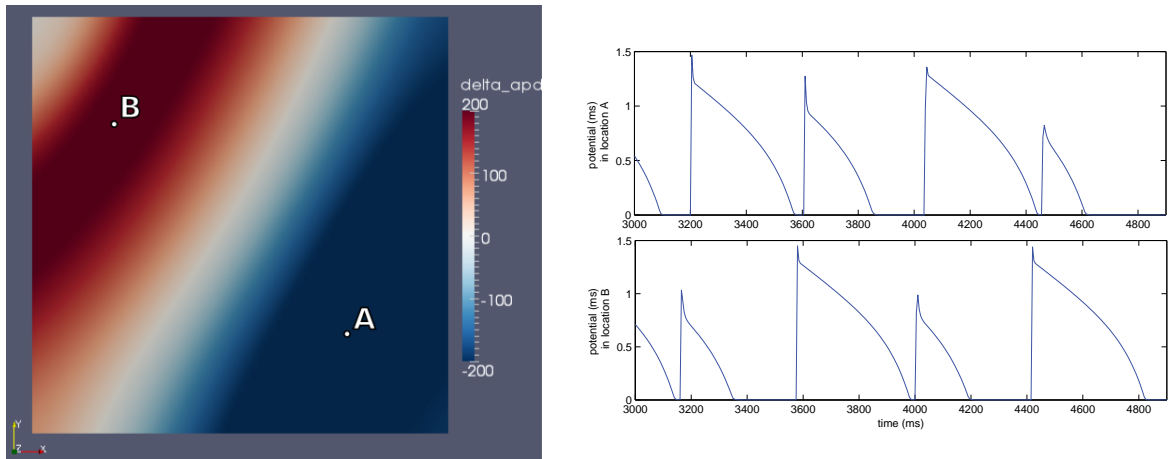


Figure 6.22: Left: spatial distribution of  $\Delta APD$  showing discordant alternans related to the pacing site  $(0,1,0)$ . Right: action potential at locations A and B.



## 7 Conclusions

This work addresses the theoretical background required to develop mathematical models of the heart's electrical activity. The numerical methods are discussed according to their accuracy and computational cost. Some improvements of the initial numerical scheme are needed to recover the desired properties. Then, we can validate the implementation of the methods related to phenomenological ionic models regarding the restitution of the conduction velocity in both isotropic and anisotropic cases. The numerical results confirm the advantage of a phenomenological approach in terms of restitution properties and computational cost. We are able to reproduce action potential duration alternans and spiral waves. In each case the pseudo-ECG signal is correlated with the physical pattern and allows the detection of the related rhythm disorder. In anisotropic cases, we get some interesting spatial distribution of cardiac alternans highlighting the relation with the fibers direction and pacing site.

Even if this essay provides a good basis for the study of heart's electrical activity, it can be enhanced in many directions. From a physiological point of view, it could be interesting to investigate the electro-mechanical coupling of the heart. Here we don't take into account tissue deformations due to muscle's contraction. However, this is a consequence of the electrical impulses propagation and has a major role in the complete behavior of the organ.

Furthermore, cardiac cell contraction is related to intracellular calcium dynamics via the excitation-contraction coupling, and we have shown that these dynamics are relevant during cardiac alternans. Consistently, we could investigate the role of excitation-contraction coupling in the development of cardiac alternans.

Moreover, we know that several external factors could have an influence on the action potentials propagation, like temperature or drugs. It would be of clinical interest to integrate in next studies these kinds of data into the models testing their consequences on electrical restitution as well as on other physiological properties. Since they can modify the ionic currents, and as a consequence the resulting action potential, they have an influence on the development of arrhythmias. The understanding of such mechanisms can help in models validation.

We notice also that each part of the heart —sino-atrial node, ventricles, atria, ...— has its own characters. Most of the models are built to reproduce the electrical activity of a specific region of the heart. In order to get a model of the whole heart's electrical activity, we need to think about the coupling between those specific models.

In this line, we want to use a realistic cardiac anatomy. We have shown the importance of the tissue structure and fibers direction in the action potentials propagation and rhythm disorder. Hence, we need a very fine description of the heterogeneity and anisotropy of the domain. If medical imaging could provide such a description, we have to discretize this information to be able to get a fine mesh and a corresponding description of the associated fibers. Since many diseases are closely related to the remodeling of the tissue, we can think about patient-specific studies.

Another direction to investigate deeper on, is the improvement of the numerical methods. We have shown that there are several limitations coming from the accuracy of the numerical scheme and the computational cost. The difficulties in recovering the physiological conduction velocity increase with the complexity of the underlying ionic model. In fact, even if the reaction terms are highly non-linear, we used a linear approximation and this could lead to error propagation, thus increasing with the number of variables. Therefore, we could gain in accuracy with a higher order method, which would allow us to use more complex ionic models with more efficiency.

In general the use of these numerical methods induces high computational costs. However, the challenge here is the optimization of those methods, without compromising the accuracy of

the model. Indeed, by reducing method's order, we have to guarantee the model fidelity and its ability to recover the physiological properties. Such an improvement could allow us to perform more complex simulations on realistic geometries.

## References

- [1] *The CellML project*. <http://www.cellml.org/>.
- [2] *High performance computing - Bellatrix*. <http://hpc.epfl.ch/bellatrix/>.
- [3] *LifeV Project*. <http://www.lifev.org>.
- [4] *A quick guide to ECG*. <http://www.ivline.info/2010/05/quick-guide-to-ecg.html>.
- [5] B. ALBERTS, *Essential cell biology: an introduction to the molecular biology of the cell*, vol. 1, Garland Pub, 1998.
- [6] A. A. ARMOUNDAS, S. H. HOHNLOSER, T. IKEDA, AND R. J. COHEN, *Can microvolt t-wave alternans testing reduce unnecessary defibrillator implantation?*, *Nature Clinical Practice Cardiovascular Medicine*, 2 (2005), pp. 522–528.
- [7] O. ASLANIDI, R. CLAYTON, J. LAMBERT, AND A. HOLDEN, *Dynamical and cellular electrophysiological mechanisms of ecg changes during ischaemia*, *Journal of Theoretical Biology*, 237 (2005), pp. 369–381.
- [8] A. J. BARD AND L. R. FAULKNER, *Electrochemical methods: fundamentals and applications*, vol. 2, Wiley New York, 1980.
- [9] B. G. BASS, *Restitution of the action potential in cat papillary muscle*, *American Journal of Physiology–Legacy Content*, 228 (1975), pp. 1717–1724.
- [10] G. W. BEELER AND H. REUTER, *Reconstruction of the action potential of ventricular myocardial fibres*, *The Journal of Physiology*, 268 (1977), pp. 177–210.
- [11] D. BINI, C. CHERUBINI, S. FILIPPI, A. GIZZI, AND P. RICCI, *On spiral waves arising in natural systems*, *Communications in Computational Physics*, 8 (2010), p. 610.
- [12] A. BUENO-OROVIO, E. M. CHERRY, AND F. H. FENTON, *Minimal model for human ventricular action potentials in tissue*, *Journal of Theoretical Biology*, 253 (2008), pp. 544–560.
- [13] C. CHERUBINI, A. GIZZI, M. BERTOLASO, V. TAMBONE, AND S. FILIPPI, *A bistable field model of cancer dynamics.*, *Communications in Computational Physics*, 11 (2012), p. 1.
- [14] E. CHUDIN, J. GOLDHABER, A. GARFINKEL, J. WEISS, AND B. KOGAN, *Intracellular  $Ca^{2+}$  dynamics and the stability of ventricular tachycardia*, *Biophysical Journal*, 77 (1999), pp. 2930–2941.
- [15] R. H. CLAYTON AND A. V. HOLDEN, *Computational framework for simulating the mechanisms and ecg of re-entrant ventricular fibrillation*, *Physiological Measurement*, 23 (2002), p. 707.
- [16] K. G. DENBIGH, *The principles of chemical equilibrium: with applications in chemistry and chemical engineering*, Cambridge University Press, 1981.
- [17] F. FENTON AND A. KARMA, *Vortex dynamics in three-dimensional continuous myocardium with fiber rotation: filament instability and fibrillation*, *Chaos: An Interdisciplinary Journal of Nonlinear Science*, 8 (1998), pp. 20–47.
- [18] A. FICK, *Ueber diffusion*, *Annalen der Physik*, 170 (1855), pp. 59–86.

- [19] R. FITZHUGH, *Impulses and physiological states in theoretical models of nerve membrane*, Biophysical journal, 1 (1961), pp. 445–466.
- [20] J. J. FOX, J. L. MCHARG, AND R. F. GILMOUR, *Ionic mechanism of electrical alternans*, American Journal of Physiology-Heart and Circulatory Physiology, 282 (2002), pp. H516–H530.
- [21] P. C. FRANZONE, P. DEUFLHARD, B. ERDMANN, J. LANG, AND L. F. PAVARINO, *Adaptivity in space and time for reaction-diffusion systems in electrocardiology*, SIAM Journal on Scientific Computing, 28 (2006), pp. 942–962.
- [22] P. C. FRANZONE AND G. SAVARÉ, *Degenerate evolution systems modeling the cardiac electric field at micro-and macroscopic level*, in Evolution equations, semigroups and functional analysis, Springer, 2002, pp. 49–78.
- [23] S. A. GAETA AND D. J. CHRISTINI, *Non-linear dynamics of cardiac alternans: subcellular to tissue-level mechanisms of arrhythmia*, Frontiers in Physiology, 3 (2012).
- [24] A. GIZZI, *Spatio-Temporal Dynamics of Cardiac Physiopathology. Experiments, Theory and Simulations*, PhD thesis, Università Campus Bio-Medico di Roma, March 2012.
- [25] A. GIZZI, E. M. CHERRY, R. F. GILMOUR JR, S. LUTHER, S. FILIPPI, AND F. H. FENTON, *Effects of pacing site and stimulation history on alternans dynamics and the development of complex spatiotemporal patterns in cardiac tissue*, Frontiers in Physiology, 4 (2013).
- [26] M. A. HEROUX, R. A. BARTLETT, V. E. HOWLE, R. J. HOEKSTRA, J. J. HU, T. G. KOLDA, R. B. LEHOUCQ, K. R. LONG, R. P. PAWLOWSKI, E. T. PHIPPS, ET AL., *An overview of the trilevos project*, ACM Transactions on Mathematical Software (TOMS), 31 (2005), pp. 397–423.
- [27] A. L. HODGKIN AND A. F. HUXLEY, *A quantitative description of membrane current and its application to conduction and excitation in nerve*, The Journal of physiology, 117 (1952), p. 500.
- [28] J. KEENER AND J. SNEYD, *Mathematical Physiology*, Springer, 1998.
- [29] J. P. KEENER, *Propagation and its failure in coupled systems of discrete excitable cells*, SIAM Journal on Applied Mathematics, 47 (1987), pp. 556–572.
- [30] M. D. KITTLESON AND R. D. KIENLE, *Small animal cardiovascular medicine*, Mosby St. Louis, 1998.
- [31] M. J. KOCICA, A. F. CORNO, F. CARRERAS-COSTA, M. BALLESTER-RODES, M. C. MOGHBEL, C. N. CUEVA, V. LACKOVIC, V. I. KANJUH, AND F. TORRENT-GUASP, *The helical ventricular myocardial band: global, three-dimensional, functional architecture of the ventricular myocardium*, European Journal of Cardio-Thoracic Surgery, 29 (2006), pp. S21–S40.
- [32] C. LUO AND Y. RUDY, *A model of the ventricular cardiac action potential: Depolarisation, repolarisation and their interaction*, Circulation Research, (1991), pp. 1501–1526.
- [33] J. MALMIVUO AND R. PLONSEY, *Bioelectromagnetism: principles and applications of bioelectric and biomagnetic fields*, Oxford University Press, USA, 1995.

- [34] MATLAB, *version 7.10.0 (R2010a)*, The MathWorks Inc., Natick, Massachusetts, 2010.
- [35] H. P. MCKEAN, *Nagumo's equation*, Advances in Mathematics, 4 (1970), pp. 209–223.
- [36] J. D. MURRAY, *Mathematical biology*, vol. 1, Springer, 2002.
- [37] J. NAGUMO, S. ARIMOTO, AND S. YOSHIZAWA, *An active pulse transmission line simulating nerve axon*, Proceedings of the IRE, 50 (1962), pp. 2061–2070.
- [38] J. NOLASCO AND R. W. DAHLEN, *A graphic method for the study of alternation in cardiac action potentials.*, Journal of Applied Physiology, 25 (1968), pp. 191–196.
- [39] P. PATHMANATHAN, M. BERNABEU, S. NIEDERER, D. GAVAGHAN, AND D. KAY, *Computational modelling of cardiac electrophysiology: explanation of the variability of results from different numerical solvers*, International Journal for Numerical Methods in Biomedical Engineering, 28 (2012), pp. 890–903.
- [40] P. PATHMANATHAN, G. R. MIRAMS, J. SOUTHERN, AND J. P. WHITELEY, *The significant effect of the choice of ionic current integration method in cardiac electro-physiological simulations*, International Journal for Numerical Methods in Biomedical Engineering, 27 (2011), pp. 1751–1770.
- [41] R. PLONSEY AND R. C. BARR, *Bioelectricity: a quantitative approach*, Springer, 2007.
- [42] A. J. PULLAN, L. K. CHENG, AND M. L. BUIST, *Mathematically Modeling the Electrical Activity of the Heart: From Cell to Body Surface and Back*, World Scientific Publishing Company, 2005.
- [43] A. QUARTERONI, *Numerical Models for Differential Problems*, Springer, 2009.
- [44] A. QUARTERONI, R. SACCO, AND F. SALERI, *Méthodes numériques: algorithmes, analyse et applications*, Springer, 2007.
- [45] J. M. ROGERS AND A. D. MCCULLOCH, *A collocation-galerkin finite element model of cardiac action potential propagation*, Biomedical Engineering, IEEE Transactions on, 41 (1994), pp. 743–757.
- [46] Y. SAAD, *Iterative methods for sparse linear systems*, Society for Industrial and Applied Mathematics, 2003.
- [47] H. I. SALEHEEN AND K. T. NG, *New finite difference formulations for general inhomogeneous anisotropic bioelectric problems*, Biomedical Engineering, IEEE Transactions on, 44 (1997), pp. 800–809.
- [48] S. STROGATZ, *Nonlinear dynamics and chaos: with applications to physics, biology, chemistry and engineering*, (2001).
- [49] J. SUNDNES, G. T. LINES, X. CAI, B. F. NIELSEN, K.-A. MARDAL, AND A. TVEITO, *Computing the Electrical Activity in the Heart*, Springer, 2006.
- [50] G. W. SUTTON AND A. SHERMAN, *Engineering magnetohydrodynamics*, (1965).
- [51] J. N. WEISS, A. KARMA, Y. SHIFERAW, P.-S. CHEN, A. GARFINKEL, AND Z. QU, *From pulsus to pulseless the saga of cardiac alternans*, Circulation Research, 98 (2006), pp. 1244–1253.

- [52] R. L. WINSLOW, J. RICE, S. JAFRI, E. MARBAN, AND B. O'ROURKE, *Mechanisms of altered excitation-contraction coupling in canine tachycardia-induced heart failure, II: Model studies*, Circulation Research, 84 (1999), pp. 571–586.

# Appendices

## A LifeV contributions

We present here the different contributions to the LifeV project. All the contributions concern the electrophysiological part related to the folder `lifev/electrophysiology/`, excepted one class in `lifev/core/function`. This one is used to calculate the euclidian distance between a fixed point—in general outside the domain—and any point in the domain. The corresponding files are : `Norm.hpp`, `Norm.cpp`.

We follow the LifeV architecture to present the different additions.

### A.1 /electrophysiology/solver

Three methods are added to the `ElectroETAMonodomainSolver.hpp`:

- Solve the monodomain equations using the ICI method and export the data every  $dt$  ms:  
`void solveICI(exporter_Type& exporter, Real dt);`
- Solve the monodomain equations using the SVI method and export the data every  $dt$  ms:  
`void solveSVI(exporter_Type& exporter, Real dt);`
- Solve the one diffusion step in splitting method using the BDF2 method:  
`void solveOneDiffusionStepBDF2(vectorPtr_Type previousPotentialPtr);`

This method has to be used in the time-loop in the following way:

```
for (Real t = initialTime; t < endTime;){
    t += timeStep;
    if (nbTimeStep==1) {
        splitting->solveOneReactionStepFE();
        (*(splitting->rhsPtrUnique())) *= 0;
        splitting->updateRhs();
        splitting->solveOneDiffusionStepBE();
        splitting->exportSolution(exporterSplitting, t);
    }else{
        splitting->solveOneReactionStepFE(2);
        *(previousPotentialPtr) = *(splitting->globalSolution().at(0));
        (*(splitting->rhsPtrUnique())) *= 0;
        splitting->updateRhs();
        splitting->solveOneDiffusionStepBDF2(previousPotential0Ptr);
        splitting->solveOneReactionStepFE(2);
    }
    nbTimeStep++;
}
```

A modification is applied to the method

```
void solveOneReactionStepFE(int subiterations = 1);
```

to allow the usage of a given number of subiterations during the reaction step.

#### A.1.1 /electrophysiology/solver/IonicModels

One class is added to use the Fox ionic model : `IonicFox.hpp`, `IonicFox.cpp`

## A.2 /electrophysiology/examples

Several examples are created to solve the monodomain equations with the RM, MM and Fox models in different cases. They include:

- construction of the fibers for the specific domain presented in Figure 2.8.
- choice between two pacing protocols :
  - the pacing down protocol explained in Section 6.3;
  - a pacing protocol made of up to 12 stimulations with pacing cycle lengths fixed by the user;

For the two protocols, the pacing site, the radius and the intensity of the stimulus can be defined by the user.

- restart protocol : the result —a given frame— from a previous simulation can be used as an initial condition for a next simulation.
- $APD$  and  $\Delta APD$  maps : the quantities are evaluated during the simulation for each point of the domain.
- construction of the pseudo-ECG signal : the location of the electrode can be defined by the user.